Pulse Shape Spectroscopy Meets Covariance: A Study in Electronic and Nuclear Dynamics in Molecules

A Dissertation Presented

by

Gönenç Moğol

to

The Graduate School

in Partial Fulfillment of the Requirements

for the Degree of

Doctor of Philosophy

in

Physics

Stony Brook University

August 2024

Stony Brook University

The Graduate School

Gönenç Moğol

We, the dissertation committee for the above candidate for the
Doctor of Philosophy degree, hereby recommend
acceptance of this dissertation.

Thomas C. Weinacht – Dissertation Advisor
Professor, Department of Physics and Astronomy

Dominik Schneble – Chairperson of Defense
Professor, Department of Physics and Astronomy

Leonardo Rastelli
C. N. Yang Institute for Theoretical Physics
Professor, Department of Physics and Astronomy

Benjamin Levine
Institute for Advanced Computational Science
Professor, Department of Chemistry

This dissertation is accepted by the Graduate School.

Celia Marshik
Dean of the Graduate School

Abstract of the Dissertation

Pulse Shape Spectroscopy Meets Covariance: A Study in Electronic and Nuclear Dynamics in Molecules

by

Gönenç Moğol

Doctor of Philosophy

in

Physics

Stony Brook University

2024

Time–resolved photoelectron and photoion spectroscopy is an important method in unearthing coupled dynamics of nuclei and electrons in molecules at ultrafast time scales ($\sim 10^{-15}$ s). In this thesis we combine ultrafast pulse shaping with covariance velocity map imaging technique as a tool to study molecular dynamics. By studying the correlation between different photoions we can hone in on specific fragmentation channels of the parent molecule and uncover the electronic and nuclear dynamics as a function of pulse shapes.

Concretely, using covariance velocity map imaging we study rich

fragmentation channels of 1,4–Cyclohexadine under strong field ionization. The combination of pulse shaping and covariance is applied to the study of electronic and nuclear dynamics of 1,1,1-Trifluoroacetone, where we report on the entanglement between electronic and nuclear degrees of freedom as well as long lasting electronic coherences during molecular dissociation. Finally, we demonstrate a new technique to measure the 3D momentum distribution of photo–electrons for velocity map imaging experiments that combines all three degrees of freedom in one apparatus.

To my family

Contents

List of Figures

List of Tables

List of Abbreviations and Symbols

AMO	Atomic and Molecular Optics
VMI	Velocity Map Imaging
ATI	Above Threshold Ionization
Ti:Sa	Titanium Saphhire
FWHM	Full Width Half Max
HCF	Hollow Core Fiber
CFROG	Co–linear Frequency Resolved Optical Gating
DSCAN	Dispersion Scan
RGA	Residual Gas Analyzer
MCP	Micro–Channel Plate
ToA	Time of Arrival
ToT	Time over Threshold
ToF	Time of Flight
COLTRIMS	Cold-target recoil-ion-momentum spectroscopy
1,4–CHD	1,4–Cyclohexadiene
3F–Acetone	1,1,1-Trifluoroacetone
3Cl–Acetone	1,1,1-Trichloroacetone
KER	Kinetic Energy Release
TDSE	Time Dependent Schrödinger Equation
DNA	Deoxyribonucleic acid
RNA	Ribonucleic acid

Acknowledgements

A Doctor of Philosophy, being a terminal degree, marks the end of a long journey, and nobody completes this journey alone. Humans are profoundly social beings and as such, every activity we engage in necessarily involves communities of people, be it scientific or personal. I would not be able to complete this degree without such communities who have provided support, guidance and encouragement.

First and foremost I would like to thank my dissertation advisor, Tom Weinacht and by extension the Weinacht group for being the chief scientific community that propelled me in ultrafast science. Tom and I met through a combination of unlikely events that led me to TA his "Light, Color and Vision" class in the Spring of 2019. While I was too busy thinking about different ways to classify superconformal field theories in four dimensions, Tom joked several times if I was sure I really wanted to be a theorist. Jokes on me, as he was right, as he often is. He had mentored several theorists before and I was no exception. He has provided tremendous support, from aligning optics, to nitty–gritty details about vacuum equipment, to explaining ultrafast molecular dynamics. Not only did he provided scientific support, but he also had an eye for beauty and elegance, which I have always admired. He taught me that a beautiful figure can do so much more than just presenting data. Before coming to Weinacht lab, I had never thought that art played any role in science. Now I understand that art is pervasive in science from the articles we write, to figures we create to presentations we give.

Of course, the graduate workers who made up the Weinacht group were almost as invaluable as Tom was. I would specifically like to thank Chuan and

Brian, who has shown me the ropes in and around the lab. Throughout our time, Chuan and I debated fiercely, whether something should be done this way or that way. We got along well because we both had an eye for math and theory. Brian on the other hand had a deep passion for hardware and laser development. I've learned from him how to debug every piece of the experimental apparatus. During his last days at Stony Brook after his defense, we had a major equipment failure. He could have just left and not look behind but he was gracious enough to help me get started on fixing the failure and I am infinitely grateful for that.

I have thoroughly enjoyed being part of the Weinacht lab and I think it is very unique that such friendly relationships exist within a research group. Sam and I sometimes disagreed. Yet we were good office mates and friends, united by both of our deep love for humanity. Julia has always been a glowing presence. Towards the later part of my PhD our friendship started to flourish and I am happy that it did. Lộc has been my mentee in the department and our relationship grew closer when she joined our group. Finally, I want to acknowledge support from senior members of our group Eric and Marty, whose expertise and input in group meetings has been extremely helpful.

I would also like to thank my previous mentor, Leonardo Rastelli for teaching me how to think through a difficult problem through examples. Nearly every time we met he would always ask me "Can we do an example?" and every time I felt stuck, he'd encourage me to simplify the problem to a much simpler example that we knew how to solve. In the lab I often find myself asking, what is the simplest thing I can do to debug an equipment or an analysis code. Examples has been my guiding principle for almost everything I did during my PhD.

Last but not least, I want to acknowledge tremendous love and support from my husband and all my friends. My partner in crime and my husband, Jack supported me through thick and thin. Whenever I broke down because of difficulties I faced in the lab or because of the inhumane state of world affairs, he helped me pick myself up to fight another day. My dear friend Waltraut, who is a better person than me in every way, has always been on my side even when I was clearly in the wrong. She would, of course, always tell me to my face that I was wrong. I admire her tenacity, enthusiasm and emotional intel-

ligence. I have learned and continue to learn from her. I would be amiss if I didn't mention my good friends from the department: Caio, Rugved, Artemis, Jolien, Abe, Henry and Jan, my zumba– and yoga–mate Alba who taught me so much about fabrics, sewing and ways of sustainable living, my friends from the salsa/bachata squad: Fanny, Evelyn, Nikit and Sean, my old time friends from Heidelberg: Nathalie, Freddy, Levin and Sebastian as well as my oldest friend from high–school, İpin. I feel very privileged to have met you and to have experienced your friendship.

Of course, my family has always been with me and I want to acknowledge the support of my family in my own language. A translation of the text below can be found in reference [154]. Her zaman yanımda olan, beni destekleyen ve beni bu kariyer yoluna koyan anneme sonsuz minnettarım. Benim yatılı liseye İstanbul'a, daha sonra Almanya'ya, sonra da Amerika'ya gidebilmeye cesaret edebilmem, annemin bana verdiği kuvvet sayesindedir. Annem bana çocukluğumdan beri iki ayağımın üstünde durmamı, haklarımı savunmamı ve sorumluluklarımı yerine getirmeyi öğretti ve bu nedenle bütün başarılarımın üzerinde etkisi vardır. Benzer şekilde babamdan da çok destek gördüm. Babam her kafamın karıştığı zamanda arayıp konuşabildiğim, yardım ve öneri istediğimde her zaman aklını veren desteğim oldu. PhD sürecinde babaannemi, dedemi ve Fatma yengemi kaybettim. Ruhları şad olsun. Dedemin ve anneannemin çocukluğumdan beri beni yetiştirmek için verdikleri emeğe minnettarım. Son olarak Şükran halamın, kuzenlerim Sümer, Esra, Petek, Ayşegül ve Nisan'ın ayrıca isimlerini sayamadığım ailemin her üyesinin gösterdiği sevgi için çok teşekkür ederim.

Finally, I want to acknowledge the people, who work behind the scenes to make the department and the university function smoothly: Donnie, for being *the best* assistant graduate program director and providing unparalleled support for all graduate students, Sue for facilitating administrative interactions with the university and research foundation Bent, Rich and Frank for supporting our lab and James for being the best teacher of machining and a great resource of machining.

List of publications

This thesis is based on the following publications with author's major contribution:

Chapter 3

Moǧol G.; Cheng C.; Weinacht T.; Nomerotski A.; Trallero-Herrero C. *3D Velocity Map Imaging of Electrons with TPX3CAM.* ***Review of Scientific Instruments 2022, 93 (1), 013003.***

Chapter 4

Cheng C.; Frasinski L. J.; Moǧol G; Allum F.; Howard A. J.; Rolles D.; Bucksbaum P. H.; Brouard M.; Forbes R.; Weinacht T. *Multi-Particle Cumulant Mapping for Coulomb Explosion Imaging* ***Physical Review Letters 130, 093001 (2023)***

Cheng C.; Frasinski L. J.; Moǧol G; Allum F.; Howard A. J.; Bucksbaum P. H.; Forbes R.; Weinacht T. *Multi-Particle Cumulant Mapping for Coulomb Explosion Imaging: the Algorithm* ***Physical Review A 109, 042802 (2024)***

Chapter 5

Moǧol G.; Kaufman B.; Cheng C; Ben-Itzhak I. Weinacht T. *Direct observation of entangled electronic-nuclear wave packets* ***Physical Review Research 6, L022047 (2024)***

Other publications that the author is involved:

Davino M.; McManus E.; Helming N. G.; Cheng C.; Moğol G.; Rodnova Z.; Harrison G.; Watson K.; Weinacht T.; Gibson G. N.; Saule T.; Trallero-Herrero C. *A Plano–Convex Thick-Lens Velocity Map Imaging Apparatus for Direct, High Resolution 3D Momentum Measurements of Photoelectrons with Ion Time-of-Flight Coincidence* ***Review of Scientific Instruments 94 (1), 013303 (2023)***

Eren E.; Gahramanov I.; Jafarzade S.; Moğol G. *Gamma Function Solutions to the Star–Triangle Equation* ***Nuclear Physics B 963, 115283 (2021)***

Chapter 1

Introduction

1.1 The Audience

Ever since I took the science communication class during my PhD, whenever I am presenting results, I always find myself asking the question of who the audience is. That is why I want to start by thinking about the audience of my thesis. Several different kinds of audiences come to my mind: my thesis committee, current or future graduate students at Weinacht Lab, undergraduate researchers at Weinacht Lab and other researchers or graduate students in the field.

I feel the obligation for my thesis to be somewhat accessible to a senior undergraduate students. I aimed this chapter and the introductory sections in each chapter to be pedagogical. While the details in subsequent sections could be beyond the knowledge of a senior undergraduate student, I hope that they can still understand the main ideas and approaches.

As any graduate student in a lab can attest, previous PhD theses play a big role from understanding the experimental apparatus, to the logic behind data analysis codes, to general guidance and inspiration for future experiments. In a way PhD theses are the institutional memory of a lab, a written summary of how the experiment and our thinking has evolved. In order to cater to this audience, I chose to write about somewhat mundane day–to–day operation of

the experimental apparatus, as well as detailed view of how I came to understand and think about my measurements.

Lastly, and most importantly, my thesis committee is an[1] audience of this thesis. I came into AMO physics from a very different background and I carry many perspectives and ways of thinking from pen–and–paper theoretical physics. These thoughts and perspectives are sprinkled throughout my thesis. I hope they can help bridge the chasm between different fields of physics.

1.2 Orders of Magnitude

> "*[Since Einstein broke everything], we've got [physics] all worked out, except for* ***small stuff****, big stuff, hot stuff, cold stuff,* ***fast stuff****, heavy stuff, dark stuff, turbulence, and the concept of time.*"
>
> – Zach Weinersmith excerpt from "Science: Abridged Beyond the Point of Usefulness" (emphasis added). Printed with permission from Zach Weinersmith.

In this thesis we study certain ultrafast dynamics of molecular systems upon photo–excitation. To do so we make use of various technologies like femtosecond lasers and ultra–high vacuum equipment. While it is easy to understand mathematically what it means to be 10^{-15} seconds or 10^{-13} atmospheric pressure and work fluently with such quantities, humans often find it hard to conceptualize such quantities very far away from everyday scales (see [1] and references therein). One's everyday experience only helps us understand quantities like 3 minutes or 2 atm.

The bare (i.e. without prefixes) SI units lie at the center of quantities we might engage in everyday life[2]. We could buy 1 kg of tomatoes, weigh 70 kg and take pain medication that has 100s of milligrams of active substances. In everyday life, we intuit and work within about 3–5 orders of magnitudes. While one can

[1] Maybe even *the* audience

[2] The universal system of units was introduced to facilitate commercial activity and is thus, intrinsically linked to human scales.

easily answer the question of how many tomatoes weight about a kilogram, one necessarily resorts to mathematics, if the same question is asked for a thousand kilograms of tomatoes. In science and particularly in physics, we are so used to working at such extra–humanly scales that we forget how far we have extended our intuition through mathematics. In this section, I attempt to center the human scale as *the* scale we can intuit and attempt to bring some context into the orders of magnitude mentioned throughout this thesis.

The most famous unit in ultrafast science must be, femtoseconds (10^{-15} seconds). This time scale appears in the electromagnetic spectrum, e.g. the oscillatory period of a 800 nm light wave is about 3 fs but also in the dynamics of one of the fastest oscillations in molecules: The vibrational period of H_2 molecule is about 8 fs. While these are scientific ways of understanding femtoseconds, they don't bring about an intuitive picture because we try to explain this scale using another scale humans have no access to. In other words, humans do not perceive vibrations of hydrogen atoms or single oscillations of electromagnetic fields, so explaining femtoseconds using these terms do not evoke an emotionally intuitive response. To bring about such a response, we need to bring these concepts down to human scales. Of course, this might be a lost cause because humans only ever deal with 3–5 orders of magnitude, let alone 15. Yet, we can attempt to center the point of comparison in human scales, say minutes rather than abstract concepts like hydrogen vibrations.

If we compared a second to femtoseconds, the difference in scale is 1×10^{15}. We can try to bring the femtosecond scale to human scales by means of an analogy in which we "equate" 1 femtosecond with 1 second. One can then pose the question if 60 femtoseconds were a minute, how long would a minute be? In other words, how long is 10^{15} minutes? The mathematics comes about to be the 1/7th of the age of the universe, which is about 7×10^{15} minutes.

$$60 \text{ femtosecond} \simeq 1 \text{ minute} \implies 1 \text{ minute} \simeq 0.14 \times \text{Age of the Universe}$$

This analogy elucidates how a ridiculously short time scale a femtosecond is. We all understand what a short period of time a minute is, even in our daily lives, let alone comparaed to the age of the universe.

In day to day experimental work, we care about the pressure inside the vacuum chamber, which regulates how many molecules are found in the laser focus. In all of our experiments, molecules are introduced into a vacuum chamber, which has a background pressure about 5×10^{-13} atmospheric pressures. It is an interesting question to ask how empty the vacuum chamber is. An intuitive insight into this question can be gained by thinking about the mean free path of hydrogen molecule as a proxy for pressure. The pressure P and the mean free path $\bar{\ell}_{\text{free}}$, of course has a reciprocal relationship: $P \sim 1/\bar{\ell}_{\text{free}}$.

We could then make the analogy from mean free path to mean free path of "humans" i.e. approximately how close to another person a person might feel in a crowded space. In a tightly packed subway the mean free path of humans is probably around 10 centimeters. If we thought of this tightly packed subway as equivalent to atmospheric pressure, then the vacuum in the vacuum chamber would correspond to having one human every 10×10^{13} centimeters, which is approximately the 1/3rd of the size of the solar system. Comparing a packed subway to having a few humans in the entire solar system illustrates, how *really empty* the vacuum chamber is.

Bringing large numbers to human scales can be a useful lens not only in sciences but also in everyday discussion of current affairs, which often involve orders of magnitude much larger or smaller than we can intuitively grasp. Almost all of this century's pressing issues from the impending climate catastrophe, to unnecessary death and destruction in wars[3], to wealth inequality[4] requires us to grasp orders of magnitudes much larger than we can perceive [2–5].

1.3 Motivation

I feel extremely privileged to be able to spend many years studying the interaction of light and molecules at insanely short time scales described in the previous section. I did not spend these years with the intention of producing

[3] A person's entire family (including distant relatives) might be about 30 people, so killing of e.g. 40,000 people amounts to wiping out of about 1,300 entire families.

[4] A million seconds is about 11.5 days, whereas a *billion* seconds is over 31 years! As of this writing, the author is yet to live a billion seconds.

new industrially applicable photo–harvesting technologies or with the intention of "bettering" the society through some novel innovation, though both might be natural consequences. Throughout my PhD, I motivated myself with the awe I have for the way the nature functions and the way we try to understand it. This is *the* motivation, why I engaged in physics, and consequently it is *the* motivation for this thesis. In what follows I try give a glimpse of this awe to the reader.

Ultrafast molecular reactions are everywhere and happen all the time. Right now, as the reader is reading these words, there is an ultrafast isomerization reaction happening in their eyes that let's them see these words. The focused light in their retina interacts with the rhodopsin molecule that undergoes an ultrafast isomerization [6–8] that ultimately results in a neuralogical signal and vision. This transformation is a beautiful example of how an ultrafast physical reaction leads to chemical and bio–chemical reactions that ultimately underlies one of the most important senses of visually–abeled people.

If the reader happens to be reading this thesis outdoors on a sunny day, there are more ultrafast reactions than meets the eye[5]. The ultraviolet radiation from the sun, which is energetic enough to break molecular bonds, is being absorbed by reader's DNA and RNA. Without any mechanism to dissipate that energy, these crucial molecules would break apart and life as we know it would not be possible. Ultrafast science has uncovered that UV excited nucleo–bases go through a conical intersection [9–12], which is a type of non–adiabatic interaction of nuclei and electrons. This conical intersection allows for nucleo–bases to dissipate the electronic energy into harmless nuclear motion, thereby preventing disassociation.

In this thesis we are primarily concerned with a type of ultrafast process, namely coherence between two electronic states of the molecule i.e. superposition of electronic states with well defined phase relationship. How electronic coherences effect photo–induced dynamics in molecules remains an active research area [13–21] and will be explored further in this thesis.

[5]The pun *is* intended.

1.4 Skeleton of the Thesis

In chapter 2 we give details about the entire experimental apparatus. In particular, we explain how we broaden the initial 30 fs pulses to support ∼7 fs pulses as well as the subsequent shaping and compression of these pulses using an acousto–optic pulse shaper. We discuss the vacuum system and the changes made to it in order to simplify and streamline the use of the sample delivery system. Subsequently, we discuss the velocity map imaging detector and the timepix camera, which is used to record the 3D velocity of ions.

While recording complete momentum information for ions is rather straightforward, 3D momentum information for electrons require a more involved approach. In chapter 3 we propose an approach to achieve this goal and demonstrate the experimental setup. We explain the data analysis steps used and compare our method to previously existing ones.

In chapter 4 we briefly dive into the probability theory that underlies all of our experimental measurements. We describe the covariance technique, which is a statistical tool that captures correlations of different fragment ions. We then compare this technique to the coincidence technique. Subsequently, we apply the covariance technique in the example of an organic molecule 1,4–Cyclohexadine and discuss its various fragmentation channels under strong field ionization.

In the fifth chapter we combine the covariance technique with the pulse shaping technique in order to study the relationship between nuclear and electronic degrees of freedom in the example of 1,1,1-Trifluoroacetone. We provide the evidence that supports our interpretation that long lasting electronic coherences are present even in the presence of large nuclear motion.

Chapter 2

Experimental Design

2.1 Introduction

Understanding the dynamics of molecular system played an important role in chemistry, biology and environmental sciences. Probing the underlying physics of molecules by experimental means however poses several technical difficulties. How does one excite the molecule? How does one detect individual fragments? What kind of vacuum apparatus is needed? In this chapter we outline the experimental techniques that were used to achieve the goal of teasing out what molecules do and why they do it when they interact with light.

As briefly discussed in section 1.2 the relevant time scale for molecular dynamics ranges from a fraction of femtoseconds to hundreds of femtoseconds. Therefore, in order to be able to probe a broad range of molecular dynamics, we need to have a time resolution of order several femtoseconds. This allows us to be in the impulsive regime for excitation i.e. the duration of the laser excitation is shorter than the dynamics we are seeking to understand. Furthermore, by making use of phase locked pulses and controlling the relative phase and delay of the two pulses, we can even access time scales shorter than the pulse duration. Commercial amplified laser systems can produce laser pulses with 30 fs FWHM pulse duration. In order to decrease the pulse duration from 30 fs to 7 fs, we need to broaden the spectrum of the laser pulses, which is achieved with a stretched hollow–core fiber. Lastly, we want to track the

dynamics of the molecules, which can be achieved with a pump–probe experiment. In this experiment, we create two laser pulses that are separated by a given delay. The first laser pulse (pump pulse) excites the molecule and starts the dynamics and the second one (probe pulse) probes the dynamics by ionizing the molecule. The subsequent fragments from the ionization encode the evolution of the excited molecule. By changing the delay between the pump pulse and the prope pulse or more generally, by changing the pulse shapes, we can utilize particular pulse shapes to capture the dynamics of molecules as they are unfolding.

The interaction between the shaped laser light and the molecule takes place in a vacuum chamber. Any background gas present in the vacuum chamber (e.g. nitrogen, oxygen, water vapor) makes it more difficult to study the molecule we are interested in. To that end, the vacuum system is equipped to go down to mid–high 10^{-10} Torr. This allows us to work with a broad range of samples that have different vapor pressures, as well as mitigate any confusion that a particular signal might be coming from a background gas. Perhaps most importantly, in these pressure regimes only a few molecules are in the laser focus allowing for the excitation of order few molecules with each laser shot.

Once the interaction has taken place, we need to record the resulting ions or electrons. While the total yield of electrons and ions have been used to study molecular dynamics for decades, one gains a much deeper insight into dynamics, if one records the momentum resolved yield of each fragment[1]. This is achieved by the velocity map imaging apparatus, which maps the velocity of fragments onto a position sensitive detector. However, individual electron or ion hits are very difficult to measure without further amplification. As an order of magnitude estimate, suppose that a single electron hit produces a signal with 1 ns duration. This signal would correspond to a current of $1.6 \times 10^{-19}\,\mathrm{C}/10^{-9}\,\mathrm{s} \approx 1.6 \times 10^{-10}\mathrm{A}$. Such small currents are very difficult to measure, which is why we amplify this signal using micro–channel plates (MCPs). MCPs are position sensitive detectors that amplifies the single electron/ion signal, while preserving the charged particles initial position on the

[1]For example, using momentum information we can differentiate between different dissociation channels and study them in isolation.

detector. The stack of MCPs we make us of in this thesis has a total gain of about 10^6, bringing the total current to be about 0.16 mA, which is easily detectable. Finally, the amplified current of electrons hits a phosphor screen and create a bright spot on the phosphor screen, i.e. produces a "hit". This hit is then recorded by the Timepix camera.

2.2 Laser Light Generation

2.2.1 Oscillator/Amplifier System

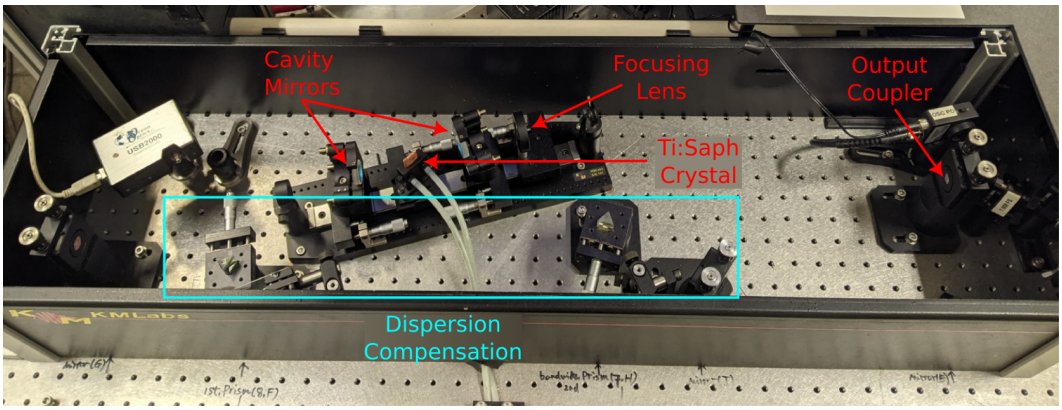

Figure 2.1: Picture of the oscillator with its important parts annotated

The initial ultrafast light is generated by a commercial Titanium:Sapphire (Ti:Sa) oscillator system from KM Labs, which makes use of Kerr–lens mode-locking . The Ti:Sa crystal is pumped with 532 nm laser from Coherent (Verdi-V5) and it is operated at 3.5 W pump power. The oscillator produces laser pulses that are sub 20 fs pulses at 88 MHz repetition rate and has an average power output of 350 mW, which has a day to day variation of at most 10%. The pulse energy of pulses out of the oscillator is about 4 nJ.

Before every day of an experiment, the spectrum of the oscillator and its power output are measured and compared to previous such measurements. If

the output power falls below 300 mW or the spectrum deviates significantly from previous measurements, every optic in the oscillator is cleaned and if necessary, realigned to match the previous performance. In Figure 2.2 we present a typical spectrum of the oscillator, which is centered at 780 nm and has an optical bandwidth of 30 nm.

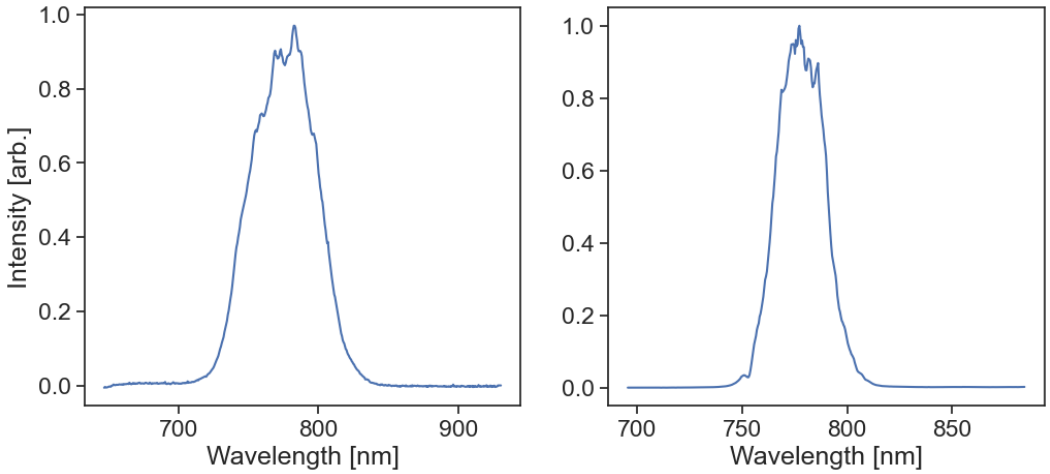

Figure 2.2: Spectrum of the oscillator system (left) and amplifier system (right)

The peak power of the pulses out of the oscillator is not suitable for strong field ionization experiments. Therefore, the initial oscillator pulses are amplified by a commercial amplifier system from KM Labs using chirped pulse amplification. The sub 20 fs pulses out of the oscillator cannot be amplified directly as the amplified intensity would be too high leading to nonlinear phase accumulation, damaging the gain medium. This is why the pulses are first stretched to hundreds of picoseconds in the stretcher using a pair of diffraction gratings.

Due to the difficulty in engineering pump lasers that operate at high pulse energies *and* high repetition rates, 88 MHz laser repetition rate is lowered to 1 kHz using a Pockels cell. The Pockels cell changes the polarization of the laser pulses at 1kHz rate and is situated between two crossed polarizers so

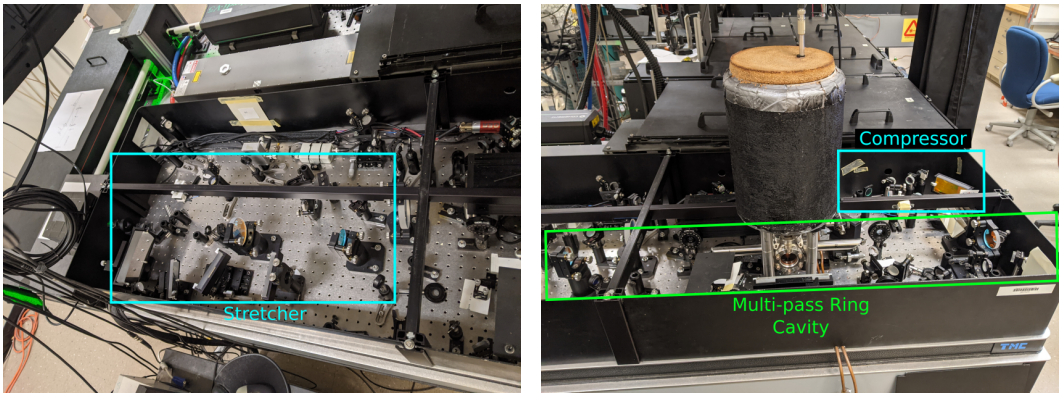

Figure 2.3: Pictures from the amplifier with main components labeled

that the vast majority of the pulses don't make it through the Pockels cell–polorizer set-up. The remaining pulses are then amplified by a 12-pass ring cavity. Subsequently amplified pulses are compressed again using a compressor that cancels the stretcher's chirp on the pulses. The resulting amplified laser pulses have up to 1.1 mJ of pulse energy at 1 kHz repetition rate.

2.2.2 Broadening in Hollow Core Fiber

The light generated by the oscillator/amplfier system is broadened in a stretched hollow–core fiber filled with argon using self–phase modulation, which we briefly discuss below [22–25].

The electric field out of the amplifier has the form

$$E(t) = E_0(t)e^{i\phi(t)} + c.c. \quad , \tag{2.1}$$

where $E_0(t)$ is the envelope function, assumed to be approximately Gaussian in profile and $\phi(t)$ is the instantaneous phase. In free space we can write $\phi(t) = \omega_0 t - kz$ with ω_0 the optical frequency and k the optical wavenumber. When the light is incident on a medium, the polarization vector in this medium can be described in Taylor Series:

$$\mathbf{P} = \epsilon_0 \boldsymbol{\chi}\, \mathbf{E} = \epsilon_0 \Big(\chi_1 \mathbf{E} + \chi_2 \mathbf{E}^2 + \chi_3 \mathbf{E}^3 + \cdots \Big) \quad , \tag{2.2}$$

In general, χ_k is a k–tensor but for spherically symmetric media, such as noble gasses, the k–tensor χ_k takes diagonal form and can be described by one scalar for each order k. By center of inversion inversion symmetry $\mathbf{r} \to -\mathbf{r}$ the polarization vector and electric field vector transform as real vectors $\mathbf{P} \to -\mathbf{P}$, $\mathbf{E} \to -\mathbf{E}$. Thus, we can see that χ_2 must be zero for a medium that has this symmetry such as spherically symmetric noble gasses. Truncating the Equation 2.2 at third order, we get:

$$\mathbf{P} = \epsilon_0 \left(\chi_1 + \frac{3}{4} \chi_3 E^2 \right) \mathbf{E} = \epsilon_0 \left(\chi_1 + \frac{3}{4} \chi_3 I \right) \mathbf{E} =: \epsilon_0 \chi(I) \mathbf{E} \quad , \tag{2.3}$$

where we have defined the intensity dependent susceptibility $\chi(I)$ as the term in the parenthesis. The factor of $3/4$ is a consequence of the trigonometric identity we used to factor out $\cos(\omega_0 t)$ term in $\mathbf{E}$: $\cos^3(\omega_0 t) = 3/4 \cos(\omega_0 t) + 1/4 \cos(3\omega_0 t)$. Further, we ignored the third harmonic term $\cos(3\omega_0 t)$.

The refractive index is then given by:

$$n = \sqrt{1 + \chi} = \sqrt{1 + \chi_1 + \frac{3}{4} \chi_3 I} \approx \sqrt{1 + \chi_1} + \frac{3\chi_3}{8\sqrt{1 + \chi_1}} I \quad , \tag{2.4}$$

where we have Taylor expanded as $\chi_3 \ll (1 + \chi_1)$. Using the definition of the linear susceptibility $n_0 = \sqrt{1 + \chi_1}$, we can write this equation as:

$$n = n_0 + \frac{3\chi_3}{8 n_0} I =: n_0 + n_2 I \tag{2.5}$$

We can thus see that the instantaneous angular frequency depends on the intensity. For the phase of the light at the end of the non-linear medium of length L we have:

$$\phi(t) = \omega_0 t - kL = \omega_0 \left(t - \frac{nL}{c} \right) = \omega_0 \left(t - \frac{n(I) L}{c} \right) \tag{2.6}$$

Note that the index of refraction is a function of the intensity and so is the acquired phase. This is the mechanism that produces new colors of light in

the hollow–core fiber:

$$\omega(t) = \frac{\mathrm{d}\phi}{\mathrm{d}t} = \omega_0 \left(1 - \frac{n_2 L}{c} \cdot \frac{\mathrm{d}I}{\mathrm{d}t}\right) \tag{2.7}$$

Since the laser is pulsed, the intensity I is a function of time and has a Gaussian profile. As the laser pulse is traversing through the non-linear medium the electric field turns on and off, generating new colors through self–phase modulation. In Figure 2.4 we plot a typical output spectrum of the fiber.

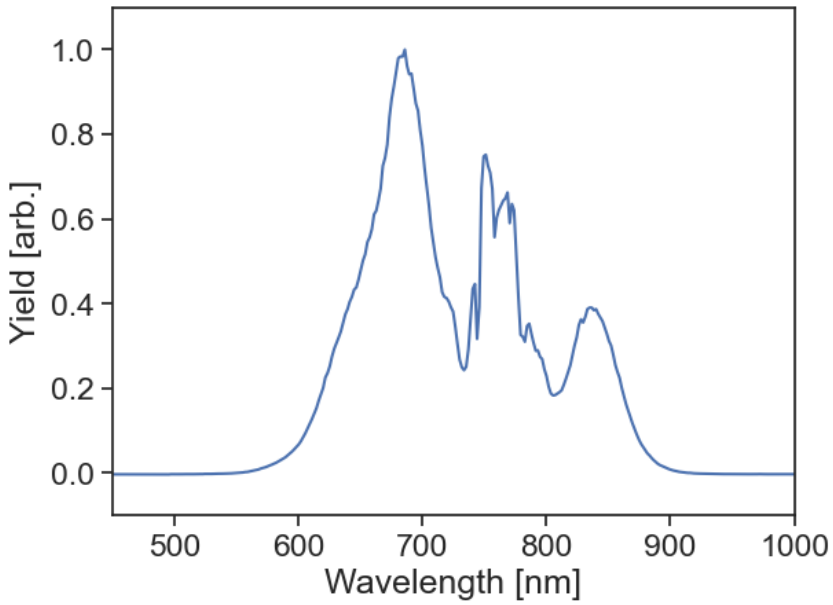

Figure 2.4: Hollow core fiber output spectrum

In our experiment we make use of a 2.1 m hollow-core fiber with inner diameter of 450 µm and fill the fiber with ultra–high purity argon (>99.999 %) [25]. Both ends of the fiber are mounted on a custom–made 1 inch disks that are hold in place by mirror mounts. The mounting disks screw into a bellow assembly that creates a vacuum–tight and movable seal. The mirror mounts are mounted on translation stages so that the entrance of the fiber has 4 degrees

of freedom $(x, y, \text{pitch, yaw})$ and the end of the fiber has 5 degrees of freedom $(x, y, z, \text{pitch, yaw})$. The degree of freedom along the z axis allows us to stretch the fiber, therefore increasing the efficiency of transmission (cf. Figure 2.5).

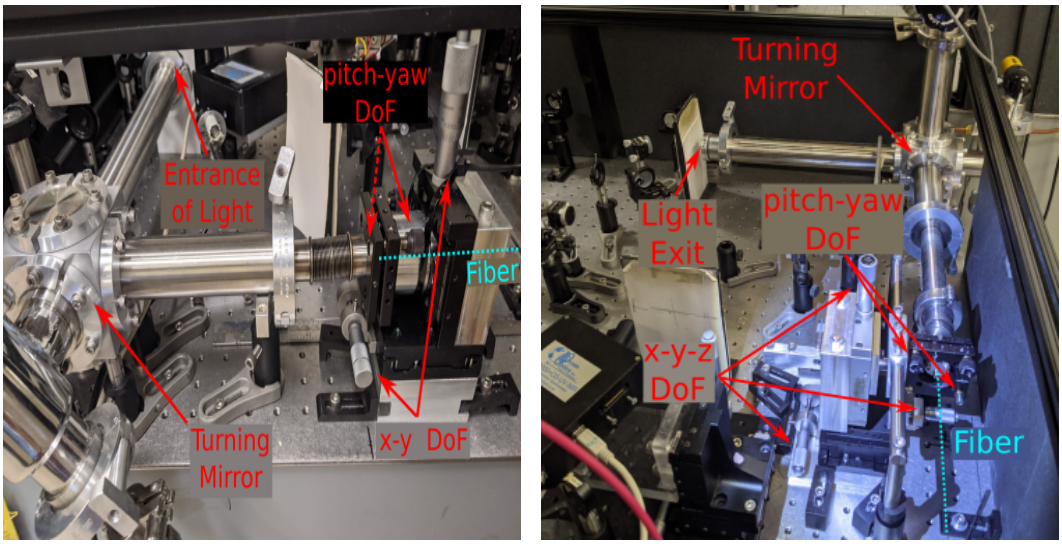

Figure 2.5: Pictures from the entrance and exit of the hollow–core fiber with important components labeled

The incident beam needs to be coupled into the fiber in an efficient manner. When the light is freely propagating in air, it is closely approximated by transverse electromagnetic mode TEM_{00}. However, inside the fiber, the boundary conditions force the electric field to be described by Bessel modes. Therefore, we match the TEM_{00} mode of the free space beam to the lowest order Bessel beam mode of the fiber, as the lowest order Bessel beam mode is the mode that has the highest transmission efficiency [26]. In [26] this mode matching calculation is carried out and the result for the optimal coupling efficiency is given by $w_0 \approx 0.644a$, where w_0 is the waist[2] radius of the incident beam and the quantity a is the inner radius of the hollow core fiber. In our case,

[2]There are many definitions of a "waist" of a Gaussian beam. Throughout this thesis we define the waist to be the radial distance at which the intensity is fallen by $1/e^2$ or equivalently the electric field is fallen by $1/e$.

the optimal waist radius is 145 µm and we focus the light into the SHCF so that the resulting waist radius is 135 µm, closely matching the optimal value of 145 µm.

In Figure 2.6 we plot the coupling efficiency of a 450 µm inner diameter hollow core fiber as a function of the waist size. The incident beam waist radius is changed by inserting lenses of different focal lengths. The resulting beam radius was measured using the knife–edge method, where a knife edge was inserted systematically at various places so that the beam is partially occluded by the knife edge. The resulting intensity at each insertion depth is measured and follows erf function i.e. the integral of a Gaussian. By fitting the measurements to the erf function the beam waist can be accurately inferred.

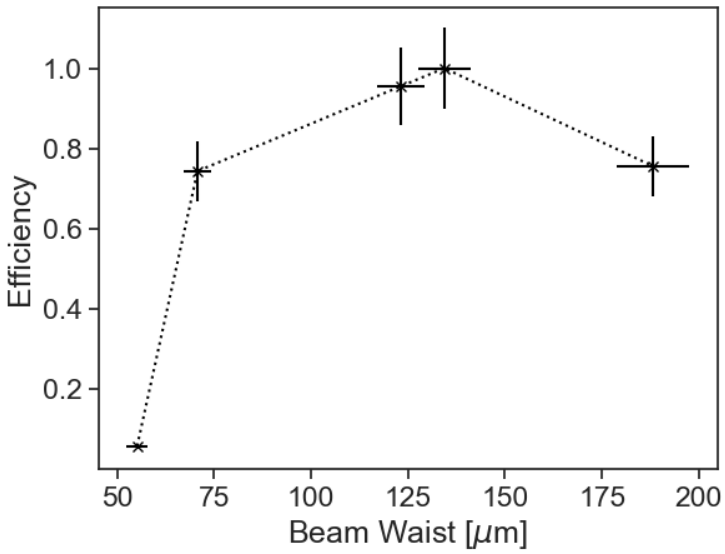

Figure 2.6: Measured coupling efficiency of Helium–Neon laser into a hollow core fiber of inner diameter 450 µm as a function of incident beam waist diameter

Making sure that we excite the lowest Bessel mode in the fiber is of paramount importance for two reasons. The first one is that higher order Bessel modes do not propagate within the hollow–core fiber efficiently. Second, higher order

modes are "speckled" i.e. have many minima and maxima within the mode. Such a "speckled" mode is not suitable for the experimental measurements that we want to carry out. In order to excite the lowest Bessel mode, we follow a simple algorithm for the initial alignment of the laser through the hollow–core fiber.

We first align the light without the fiber setup through two irises that mark the position of the fiber and mark the exit position of the light with a third iris. We then install the fiber setup and bring the fiber entrance and exit to the position of the previously aligned light. This method also minimizes the chance that the entrance of the fiber is damaged as most of the light is transmitted through the fiber during the initial alignment.

Once the light makes it through the entirety of the fiber, one needs to optimize the transmission efficiency as well as the optimize the output mode of the fiber. The x, y degrees of freedom of the entrance controls the coupling efficiency, and therefore they are the first degrees of freedom that need to be adjusted. The pitch and the yaw of the entrance also controls the transmission efficiency but to a lesser extent. These degrees of freedom are however very important in getting a clean mode out of the fiber, alongside with the pitch and the yaw of the fiber exit. The x, y degrees of freedom at the exit generally control the exit position of the light and usually don't need to be adjusted, especially if the initial alignment procedure we outlined in the previous paragraph is followed. While the rough alignment of the fiber can be achieved systematically using the above protocol, there is unfortunately no algorithm for the fine alignment. The best positions for each degree of freedom and the intuition of which degree of freedom needs to be adjusted is gained through repeated alignment of the fiber assembly[3]. That being said, in Appendix A we depict how each degree of freedom affect the output mode of the fiber, if they are slightly misaligned from the optimal position.

For day to day operation, the fiber mounts are stable enough so that generally

[3]The reader might be wondering, how one can achieve a goal without being able to articulate how that goal is achieved. The example of the chicken–sexer, who are people trained in identifying the sex of a chicken, despite not being able to articulate how they do it [27], is an analogous example and is discussed in philosophy texts often.

no alignment of the fiber is needed. We characterize the output of the hollow–core fiber by its transmission efficiency and by the output spectrum. The typical end to end efficiency of the fiber is about 65%, which includes losses at the entrance and exit windows ($\sim 16\%$) and two silver turning mirrors ($\sim 8\%$). The gas pressure inside the hollow core fiber assembly is adjusted to match the spectrum depicted in Figure 2.4. The resulting argon pressure inside the fiber is usually around $600 \pm 50\,\mathrm{Torr}$. While the fiber assembly can hold the argon pressure for multiple days, air leaks in very slowly, and thus distorting the output spectrum. If the spectrum cannot be reproduced, we vacuum out the fiber and re-fill it with argon, which usually recovers the desired spectrum.

2.2.3 Pulse Shaper

We use the pulse shaper discussed in [25] to compress the broad bandwidth light that was generated in a hollow core fiber as well as for shaping the compressed pulses for experiments. The pulse shaper allows us to have extensive control over the pulses [28–32]. For the experiments presented in this thesis we have used the pulse shaper to create two pulses with given delay, relative intensity as well as relative phase between the two pulses. We further use the pulse shaper to characterize the temporal shape of the pulses we generate through dispersion scans (DSCAN) [25, 33–37] and through second harmonic generation co–linear frequency resolved optical gating (CFROG) [38–40] .

The main idea of the pulse shaper is to shape the initial laser pulse $E(t)$ in the frequency domain by adjusting the intensity and phase of each individual frequency with an acousto–optic modulator (AOM). Schematically we need to perform the following operations:

$$E(t) \xrightarrow{\mathcal{F}} E(\omega) \xrightarrow{\times M} M(\omega)E(\omega) =: \widehat{E}(\omega) \xrightarrow{\mathcal{F}^{-1}} \widehat{E}(t) \quad , \tag{2.8}$$

where $M(\omega)$ is the mask we put on the initial electric field to generate the shaped pulses and $\mathcal{F}$ indicates Fourier transformation, in the sense that each frequency is mapped to a position on the AOM crystal.

As a concrete example, a mask of the form $M(\omega) = 1 + e^{i\omega\tau}$ creates two pulses of equal amplitude, that are delayed by a delay τ as seen by Fourier shift

theorem:

$$\mathcal{F}^{-1}\Big(\left(1 + e^{i\omega\tau}\right) E(\omega) \Big) = E(t) + E(t+\tau) \tag{2.9}$$

Each of the operations in Equation 2.8 correspond to optical elements we use in our experimental setup (see Figure 2.7). First, the light entering the pulse shaper is diffracted by an optical grating. This grating maps frequency into angle, as understood by the diffraction equation:

$$n\lambda = d\sin(\theta) \qquad , \tag{2.10}$$

where n is the diffraction order, λ the wavelength, d the spacing of the diffraction grating and θ is the diffraction angle. This angle is then mapped to a position by a curve mirror in $2f$ configuration. This grating and curved mirror configuration corresponds to the first step in Equation 2.8. At the focal position of this curved mirror is the acousto-optic modulator that writes the mask $M(\omega)$. Finally, all of the colors are put back together with a curved mirror–grating setup in the identical but inverted order.

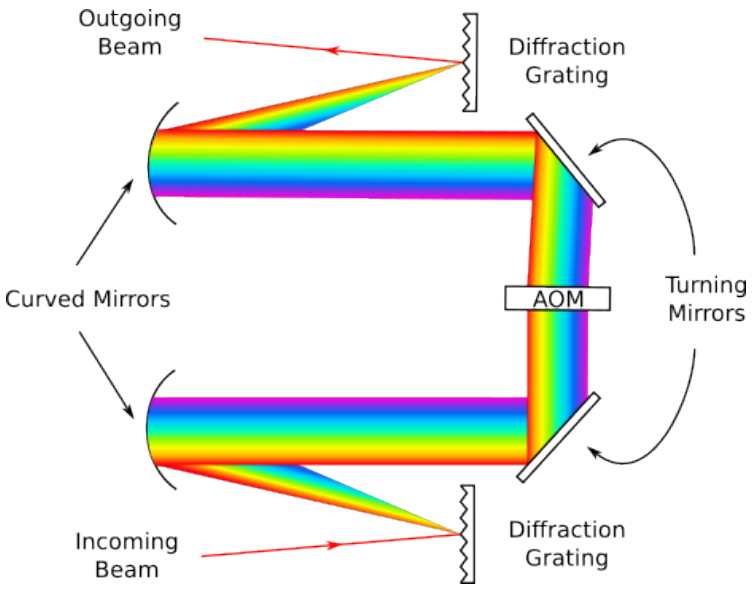

Figure 2.7: Schematic experimental setup of the pulse shaper

On a daily basis, we use the pulse shaper to compress and characterize pulses we generate. The characterization starts with pulse shaper assisted DSCANs. Traditionally, DSCANs are performed by scanning the second order dispersion with a pair of glass wedges [33–35], where the amount of glass inserted directly corresponds to the amount of second order dispersion added. Since we have extensive control of the laser light using the pulse shaper, instead of inserting glass, we can directly control the second and higher order phases, for which we write a mask of the form

$$M(\omega) = \exp\left\{ i \left[\frac{\beta_2}{2}(\omega - \omega_0)^2 + \frac{\beta_3}{3!}(\omega - \omega_0)^3 + \frac{\beta_4}{4!}(\omega - \omega_0)^4 \right] \right\} \quad . \quad (2.11)$$

We scan the second order phase β_2 in order to perform pulse shaper assisted DSCANs, analogous to insertion of glass in the original DSCAN techniques. The third and forth order phases β_3 and β_4 are adjusted based on the DSCANs in order to optimize the pulse duration. However, during the scan itself these higher order phases are held constant. The shaped laser light is then focused onto a BBO crystal to generate the non–linear second harmonic signal as in the original DSCAN technique [33, 34]. We filter out the residual fundamental with a polarizer as the fundamental and the second harmonic signal have orthogonal polarization. Subsequently, we record the second harmonic signal with a spectrometer. The obtained scan is then reconstructed [36, 37] to yield the phase relationship of each frequency with respect to each other (see Figure 2.8). The algorithm also provides the phase needed to be written for each frequency in order to yield a compressed pulse. This excess phase is programmed back into the pulse shaper [41] and if needed, we adjust the third and forth order phase in order to yield a compressed pulse.

At the end of this iterative process, we perform a pulse shaper assisted CFROG [38–40] to confirm the temporal profile of the reconstructed pulse. For this step we generate two pulses with the pulse shaper and scan the delay between them. Both of the pulses are incident on a second harmonic crystal that generates the doubled frequency, which provides the non–linearity to determine the phase relationship of each color. We subsequently filter out the fundamental spectrum with a polarizer and record the remaining spectrally–resolved second harmonic

signal with a spectrometer. From this spectrally resolved autocorrelation signal, one can reconstruct the pulse shape and duration [40], which is crucial to the experiments performed in this thesis.

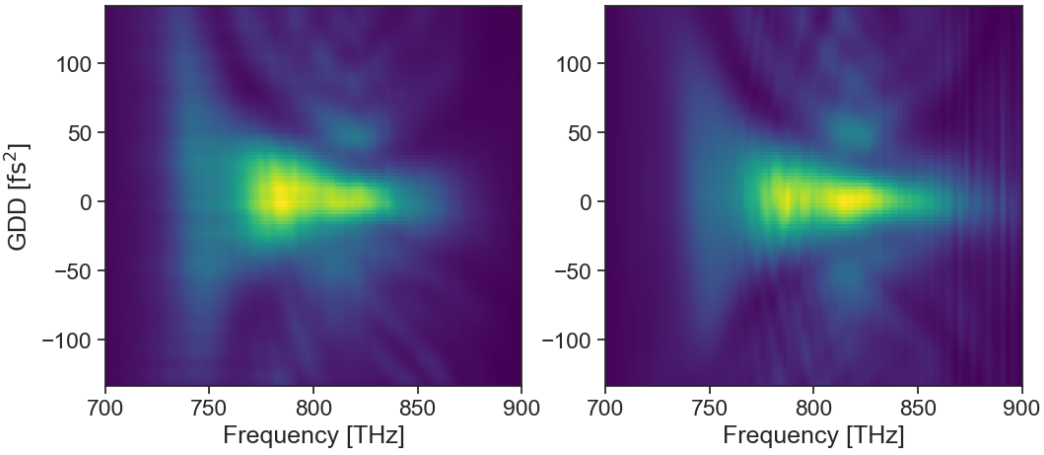

Figure 2.8: Sample DSCAN reconstruction of a 7 fs pulse

After compressing the pulse, we write an additional mask to perform the experiments. We are generally interested in time–resolved dynamics of molecules and investigating contributions of electronic and nuclear degrees of freedom. Thus, we make use the following mask in all of our experiments, which generates a double pulse with given delay and relative phase between the pulses:

$$M(\omega) = A_{\text{tot}}\Big(1 + A_{\text{rel}} \exp\left(i\,\tau(\omega - \omega_L) + i\phi_{\text{rel}}\right)\Big) \qquad , \tag{2.12}$$

where A_{tot} controls the overall amplitude of both pulses, A_{rel} the relative amplitude, ϕ_{rel} the relative phase and τ the relative delay between the two pulses. The quantity ω_L is the locking frequency and is the frequency for which the electric field interferes constructively for all delays. In chapter 5 we go into more detail about how these parameters are related to dynamics of molecules but in order to whet the appetite of the reader, we remark that delay scans with different locking frequencies informs us of nuclear dynamics while phase scans at fixed delays tells the story of electronic dynamics.

2.3 Vacuum Chamber & Detector

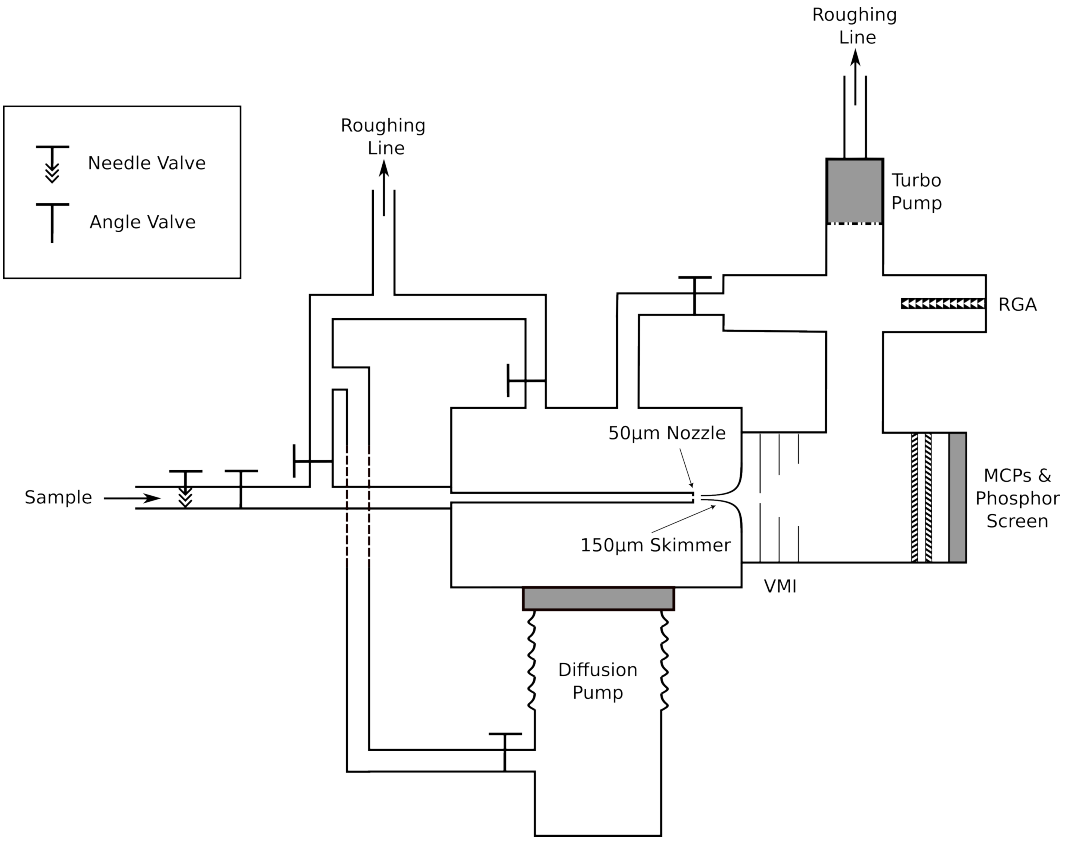

Figure 2.9: Schematic diagram of the vacuum apparatus before the reconfiguration

The vacuum apparatus consists of two chambers (see Figure 2.9): the science chamber and the sample chamber. The sample is introduced into the sample chamber through a needle valve that is connected to a nozzle of diameter $50\,\mu$m. The sample and science chamber are differentially pumped and are connected by a skimmer of diameter $150\,\mu$m. A diffusion pump pumps on the sample chamber, while a turbo pump pumps on the science chamber (see Figure 2.9). The laser light is introduced into the reaction chamber through a UV fused silica window of thickness 2 mm and focused with a spherical sil-

ver mirror which has a focal length of 5 cm. This tight focus allows us to generate very intense electric fields that are required to perform strong field measurements. Furthermore, tighter focusing has the advantage that only a few molecules find themselves within the focal volume and thus, are excited and probed.

The background pressure in the science chamber is around 5×10^{-10} Torr and during operation with a sample, the pressure is adjusted so that a desired count rate of resulting ions are reached. This is done for the optimal use of statistical tools outlined in chapter 4. When sample is introduced, typically the pressure in the science chamber is on the order of high 10^{-9} Torr to mid 10^{-8} Torr, which is measured by a residual gas analyzer. The final pressure is adjusted through two valves: the aforementioned needle valve and the gate valve that controls the conductance of the diffusion pump, and consequently the effective pumping speed. The needle valve provides control over the long term pressure, whereas the gate valve is very fast acting and used to adjust the pressure quickly. Before performing an experiment we stabilize the pressure in the science chamber to *a* pressure usually in the mid 10^{-8} Torr, which usually takes about an hour[4]. The pressure is then adjusted up or down from this stable pressure with the gate valve so that a desired count rate is reached. Due to the initial time it takes to stabilize the pressure, the introduction of sample in the vacuum chamber is the first step of a day of measurement. While the pressure settles, we start aligning and characterizing the light source as discussed in section 2.2.

All of the samples in this thesis are either in gas or liquid form with high enough vapor pressure to perform the experiment. If we are using a gas sample, the tubing to the gas tank is pumped out with a roughing pump through a bypass valve so that virtually no air is introduced into the sample chamber. If the sample is a liquid one, we perform freeze pumping in which the sample is frozen from outside with liquid nitrogen and then the sample holder is pumped out with the same roughing pump. Once the roughing pressure falls to baseline values, all of the valves are closed and the sample is brought back up to room temperature. While the sample is warming up to room temperature, it is very

[4]Improvements outlined in subsection 2.3.1 remedy this "inconvenience".

important *not* to introduce it into the vacuum chamber before it equilibrates to room temperature. This is because the vapor pressure of the sample is lower when it is colder and it depends very strongly on the temperature of the liquid. Thus, introducing the sample before it equilibrates to room temperature might result in unwanted pressure spikes that are hard to control and in extreme cases might damage sensitive experimental apparatus.

2.3.1 Reconfiguration of the Vacuum Chamber

There were two drawbacks to the vacuum chamber that were discussed in the previous section: the use of the diffusion pump and the long time needed before pressure in the science chamber reaches an equilibrium. Most of the experiments in this thesis were performed with the previous configuration, and the reconfiguration does not change the main goal or function of the vacuum chamber. It makes it more robust and easier to use.

Diffusion pumps are phenomenal in terms of their pumping speed and low cost. They can also be maintained in house, unlike turbo pumps as there are no moving parts. The main drawback of diffusion pumps is their potentiality for catastrophic failure. Diffusion pumps work similar to Italian stovetop espresso pots (Moka pot) in the sense that an oil is heated up at the bottom of the pump and then sprayed downwards [42]. Molecules that are hit by the downward spraying oil get a momentum in downward direction, and are subsequently pumped out by the roughing pump. A problem arises, when the roughing line pressure rises due to a failure of the roughing line. At high roughing line pressures, the oil reserve at the bottom of the diffusion pump back streams into the chamber, severely contaminating the vacuum chamber. On June 30, 2023 such a failure occurred, which prompted the reconfiguration of the vacuum chamber.

Since this failure, we have replaced the diffusion pump with a turbo pump as we were not making use of the high pumping speeds of the diffusion pump and therefore wanted to avoid any future such catastrophic failures. Furthermore, the sample manifold and sample delivery was simplified to achieve faster pressure equilibrium in the science chamber. In order to achieve this, we removed the 50 μm nozzle and reconfigured the rest of the sample delivery manifold to

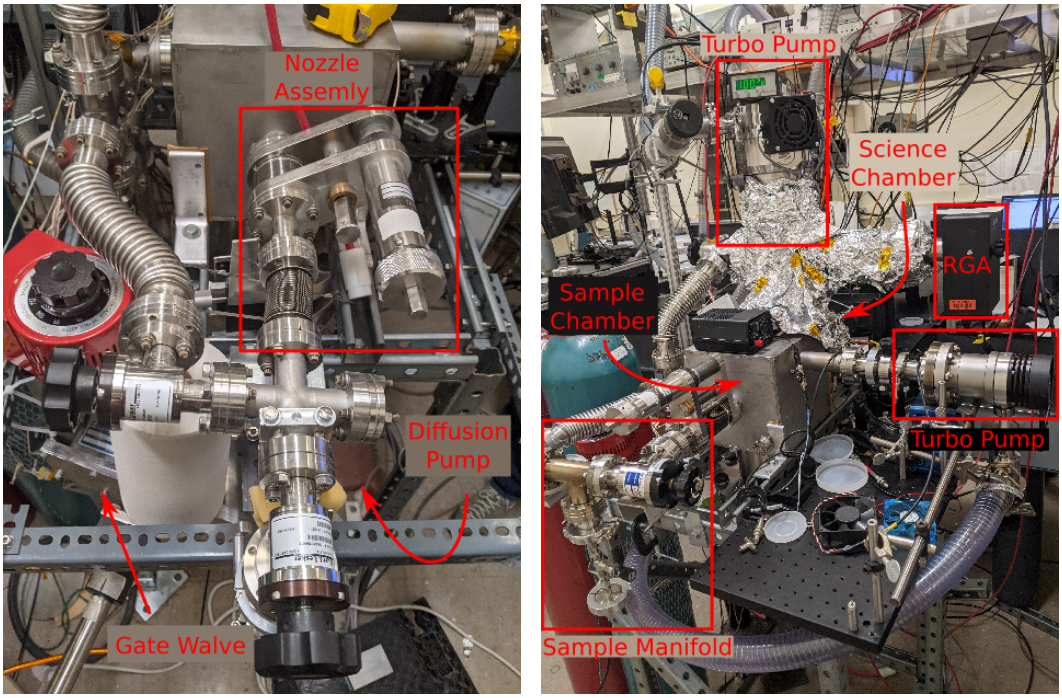

Figure 2.10: Picture of the vacuum apparatus before the reconfiguration (left) and the sample manifold after the reconfiguration (right)

accommodate this change. Currently, sample directly streams from the sample holder through a needle valve into the sample chamber, instead of going through a small opening of the nozzle. This change has achieved a near instantaneous control of the pressure in the science chamber, which allows for a very precise control of the pressure. With this change, the pressure in the science chamber equilibrates in about 10 minutes instead of an hour.

In Appendix B we detail the recovery from the diffusion pump failure because the methods we employed to decontaminate an ultra high vacuum chamber from diffusion pump oil could be useful for any experimentalist that works with diffusion pumps.

2.3.2 Velocity Map Imaging Apparatus

We use a velocity map imaging (VMI) apparatus to record the momenta of ions and electrons we generate via photoionization. The idea behind VMI is to create spatially varying electric fields so that the momentum of the charged particle in the center of the detector is mapped to a position on a phosphor screen, independent of the initial position of the ion [43].

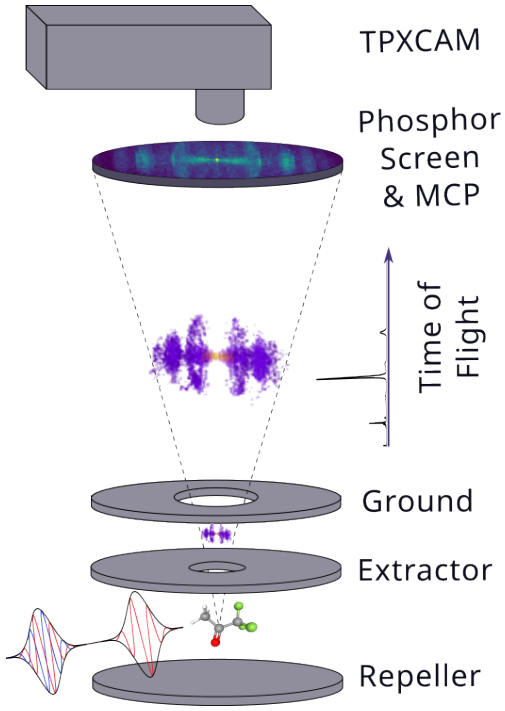

Figure 2.11: Schematic of velocity map imaging apparatus. Created by the author for publication in [126].

In Figure 2.11 we depict the schematics of the VMI apparatus. The laser light is focused at the center of the VMI plates using a 5 cm focal length silver mirror. The charged particles generated by photoionization are then extracted by three VMI plates that are set to voltages of 2400 V/1800 V/0 V for recording ion momenta. The signal of one charged particle is then amplified by a stack of two micro–channel plates (MCP), each with a gain of around a thousand,

resulting in a total gain of about a million. The amplified signal is then converted to light with P47 phosphor screen and these hits on the phosphor screen are recorded by the timepix camera.

The VMI method as we discussed allows one to record the projection of the 3D momentum cloud (p_x, p_y, p_z) of charged particles onto the 2D surface of the phosphor screen (x, y). Assuming cylindrical symmetry, one can then construct the 3D momentum using Abel inversion [44, 45]. Mathematically, Abel inversion assumes a continuous and cylindrically symmetric function. In our case this function is given by the recorded VMI image. Satisfying both of these assumptions for VMI images come with certain drawbacks. Since each ion/electron hit is discrete, and the continuous VMI image is constructed through repeated measurement, satisfying the continuity assumption requires long data acquisition times. Similarly, the requirement of cylindrical symmetry limits the kinds of experiments one can perform. In particular, the cylindrical symmetry precludes the use of elliptically polarized light as this breaks the cylindrical symmetry [46]. For all these reasons, it is better to measure 3D momentum of charged particles directly, rather then reconstructing it in post–processing. We discuss the method of recording 3D ion momentum in subsection 2.3.3 and leave the measurement of 3D electron momentum for chapter 3 as this is a more involved setup both experimentally and from the data analysis point of view.

2.3.3 Timepix Camera and 3D Ion Momenta

Traditionally, cameras work by recording frames i.e. an integral of light on a sensor for a given duration, usually by using a shutter that exposes the light sensitive detector. While commercially available cameras can have integration times as low as several microseconds, this time resolution is not sufficient to record the momentum of ions in the z–direction, without utilizing further experimental apparatus as the time of flight spread of ions is of the order 100 ns. The timepix camera on the other hand is an event–based camera, which means that it records individual hits ("events"), instead of an integral over a certain period. It can record the timing of these events with 1.56 ns time resolution and thus 3D momentum of charged particles can be recorded without any

change to the rest of the experimental apparatus. In what follows, we detail the working principle of the timepix camera as well as how it was used in the experiment.

The photosensitive silicon pixel sensor on the camera registers if a pulse of light, that crosses a certain threshold, is present [47–49]. The camera has an 256×256 array of such pixel sensors, each of which has dimensions of $55\times55\,\mu\text{m}^2$. When sufficient light is incident on any of the pixels and exceeds the predetermined threshold, the time of arrival (ToA) is recorded as well as how long the pixel remained over the threshold (time over threshold, ToT). Time of arrival information is recorded with a global 40 MHz clock and refined at pixel level by a 640 MHz clock, resulting in a time resolution of 1.56 ns. Time over threshold information is recorded with a the same global 40 MHz clock but is not further refined, consequently it has a time resolution of 12.5 ns.

A readout chip then sends the quadruple information (x, y,ToA,ToT) and can support up to 80 Mpixel/s. If we assume that each ion/electron hit takes about 20 pixels, the readout chip can support up to 4000 hits per laser shot for a 1 kHz laser system. While we never make use of such high count rates, for lasers systems with 100 kHz repetition rate, which are becoming more common, the maximum readout rate would be 40 hits per laser shot, still adequate for photoionization experiments.

The camera is further endowed with two time to digital converters with 260 ps time resolution, which we use to mark the arrival of the laser pulse. The second TDC is only used to record the 3D momentum of electrons and its use is discussed in chapter 3. The time difference between the arrival of the laser and the ToA reading from each pixel yields the time of flight (ToF) of the charged particle. This time of flight information can be converted into the z–momentum in a straightforward manner [50] as ions have a time of flight spread of the order hundred nanoseconds and 1.56 ns time resolution is more than enough for this application. Perhaps more importantly, the ToF information also let us distinguish different species of ions by their charge to mass ratios: ToF $\propto \sqrt{m/q}$. The ability to determine the species of each ion at each laser shot and as well as their 3D momenta forms the bedrock of experiments

presented in this thesis.

In the pre–processing step of the raw timepix data, we need to correct for time walk effects as well as centroid every hit [50]. As with any constant threshold discriminator, the timepix camera suffers from time–walk effects, in which the time of arrival correlates with the intensity of the light being recorded. In Figure 2.12 we plot two signals that arrive at the same time but are amplified differently. We can see that the stronger signal has an earlier nominal ToA, which is entirely caused by the time–walk effect, which is why ToT information is used to correct for this correlation in order to yield an accurate measurement of time of flight of charged particles. Lastly, we compute the ToT–weighted average of a pixel cluster in order to determine the position of a hit. The final data after the pre–processing contains five columns: `laser shot number, x, y, ToF, ToT`, which form the basis of all experimental results.

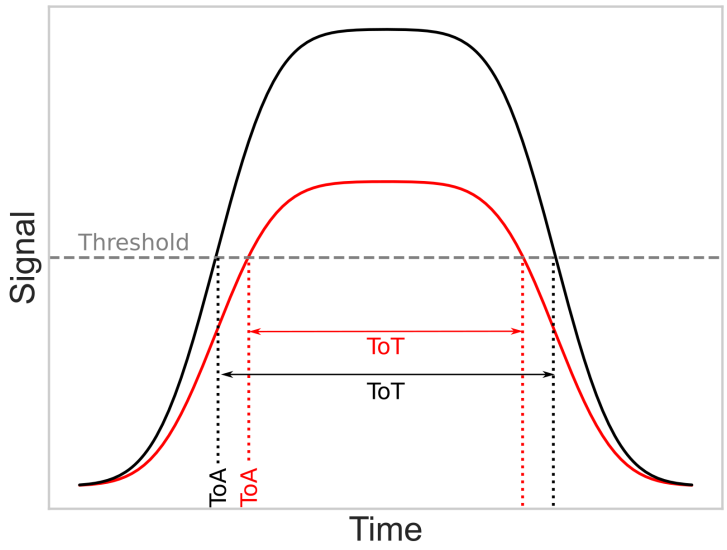

Figure 2.12: The black and red curves indicate the arrival of charged particles at the same time. Nominally, the time of arrival of both curves are different due to the time walk effect as the time of arrival correlates with time over threshold.

2.4 Intensity Calibration

One of the most important experimental parameters is the intensity of light at the focus in the reaction chamber. We can easily measure the average power of laser pulses using a power meter. In order to relate the average power to the intensity at the focus we need to perform a calibration. We simply write

$$I_{\text{focus}}[\text{TW/cm}^2] = \alpha P_{\text{avg}}[\text{mW}] \qquad , \tag{2.13}$$

where the calibration constant α with units [TW/cm^2/mW] is to be determined. Note that this calibration depends on the pulse duration because the conversion from average power to peak power (i.e. power in each pulse) depends on pulse duration. In particular, we have:

$$P_{\text{peak}} = \frac{E}{\Delta t} \quad , \quad P_{\text{avg}} = E f_{\text{rep}} \implies P_{\text{peak}} = \frac{P_{\text{avg}}}{f_{\text{rep}} \Delta t} \qquad , \tag{2.14}$$

where E is the energy carried by each pulse, Δt is the FWHM pulse duration and f_{rep} is the repetition rate of the laser. We can do a back of the envelope calculation to estimate the intensity as follows:

Let the focal length of he focusing optic be f_{focus} and assuming a Gaussian beam and aberration–free focusing, the beam size at the focus is given by:

$$w_{\text{focus}} = \frac{\lambda f_{\text{focus}}}{\pi w_0} \qquad , \tag{2.15}$$

where w_{focus} is the radius of the beam waist at the focus, λ is the central wavelength and w_0 is the initial beam waist radius at the focusing optic. Finally, we can calculate the space and time averaged intensity (in FWHM):

$$I_{\text{focus}} = \frac{P_{\text{peak}}}{\pi w_{\text{focus}}^2} = \left(\frac{1}{f_{\text{rep}} \Delta t} \right) \frac{P_{\text{avg}}}{\pi w_{\text{focus}}^2} = \left(\frac{\pi w_0^2}{f_{\text{rep}} \Delta t \lambda^2 f_{\text{focus}}^2} \right) P_{\text{avg}} \tag{2.16}$$

Lastly, we take into account the losses at the vacuum window (about 4% per surface) the silver focusing mirror (about 3%). With the following pulse parameters: $w_0 \approx 0.21\,\text{cm}$, which corresponds to 0.5 cm FWHM diameter, $f_{\text{rep}} = 1\,\text{kHz}$, $\lambda = 700\,\text{nm}$, $\Delta t = 7\,\text{fs}$, and $f_{\text{focus}} = 5\,\text{cm}$, we obtain the calibration factor:

$$\alpha = 149 \left[\frac{\mathrm{TW/cm^2}}{\mathrm{mW}} \right] \tag{2.17}$$

In this estimate, we assume that the laser beam is a perfectly Gaussian beam and that the entire beam is focused without aberrations. Therefore, the focus is in reality less tight than we assumed in the above calculation. While one can try to take these effects into account, we choose the route of determining this coefficient through experimental means and use the somewhat naive calibration in Equation 2.17 as a guiding rough estimate.

In order to determine the intensity calibration, we utilize physical principles that lets us infer the intensity directly. The main idea comes from above threshold ionization, in which an atom in intense laser fields absorbs more photons that is needed to ionize, resulting in peaks in the photoelectron spectrum that are separated by one photon energy. The ATI spectrum therefore, has a built–in energy calibration, which can be used to calibrate the position of an electron to its momentum using the fact that ATI peaks are spaced by one photon order. Furthermore, the ATI spectrum develops a cutoff at $2U_p$, where U_p is the ponderomotive energy; the average energy of a free electron in an oscillating electric field over one optical cycle [51–53]. The ponderomotive energy is proportional to the laser intensity and thus locating the $2U_p$ cutoff on the spectrum gives a direct calibration of laser intensity.

This cutoff can be understood from conservation of momentum of an electron in an electric field. Assuming electric dipole approximation i.e. that the wavelength is much larger than the atom, we can write for the electric field $E(\mathbf{r}, t) \approx E(t)$. Furthermore, we assume "simple–person's" model, where we disregard elastic rescattering of the electron by the atomic core. The conserved (aka canonical) momentum of an electron in this field is given by $\boldsymbol{p}_{\mathrm{cons}} = m\boldsymbol{v} - e\boldsymbol{A}$, where m is the mass and $\boldsymbol{v}$ the velocity of the electron, $\boldsymbol{A}$ is the vector potential. Assuming that the electron had zero velocity at the time of the ionization, we have $\boldsymbol{p}_{\mathrm{cons}} = -e\boldsymbol{A}$. The maximum momentum of the electron is then given by $\boldsymbol{p}_{\mathrm{max}} = e\boldsymbol{A}_{\mathrm{peak}}$, where $\boldsymbol{A}_{\mathrm{peak}}$ is the peak vector potential, or equivalently in terms of the electric field, we have $\boldsymbol{p}_{\mathrm{max}} = e\boldsymbol{E}_{\mathrm{peak}}/\omega_0$, where ω_0 is the laser frequency. The maximum kinetic energy of the electron without

rescattering is then given by

$$E_{\max} = \frac{\boldsymbol{p}_{max}^2}{2m} = \frac{e^2 E_{\text{peak}}^2}{2m\omega_0^2} = 2U_p \qquad , \tag{2.18}$$

where we used the equation for the ponderomotive energy:

$$U_p = \frac{e^2 E_{\text{peak}}^2}{4m\omega_0^2} \tag{2.19}$$

This $2U_p$ cutoff we described can be used to calibrate average power to intensity because it is a directly related to the intensity. If we identify this cutoff in the photoelectron spectrum, we can infer $2U_p$ and in return the peak intensity. Before we continue with the experimental data, we rewrite the ponderomotive energy in terms of the intensity $I_{\text{peak}} = c\epsilon_0 E_{\text{peak}}^2/2$:

$$U_p = \frac{e^2}{2c\epsilon_0 m_e} \cdot \frac{I_{\text{peak}}}{\omega_0^2} \implies U_p[\text{eV}] = 0.053 \times I_{\text{peak}}[\text{TW/cm}^2] \tag{2.20}$$

Using the pulse shaper to vary the pulse energy, we have carried out measurements of ATI spectrum of argon at different intensities. While each measurement allows us to determine U_p, the combination of many measurements provides higher precision by averaging the resulting calibration parameters.

In Figure 2.13 we present the experimental results. We plotted the photoelectron spectrum in logarithmic scale as this allows for the determination of the cutoff, which is difficult to determine on a linear scale. We can clearly see the ATI peaks of argon as vertical lines spanning different intensities. We have also marked in this figure two possible places for the location of the $2U_p$ cutoff because the exact location of the cutoff is hard to determine in a purely quantitative fashion. We use these two measurements to estimate our uncertainty of the calculated laser intensity.

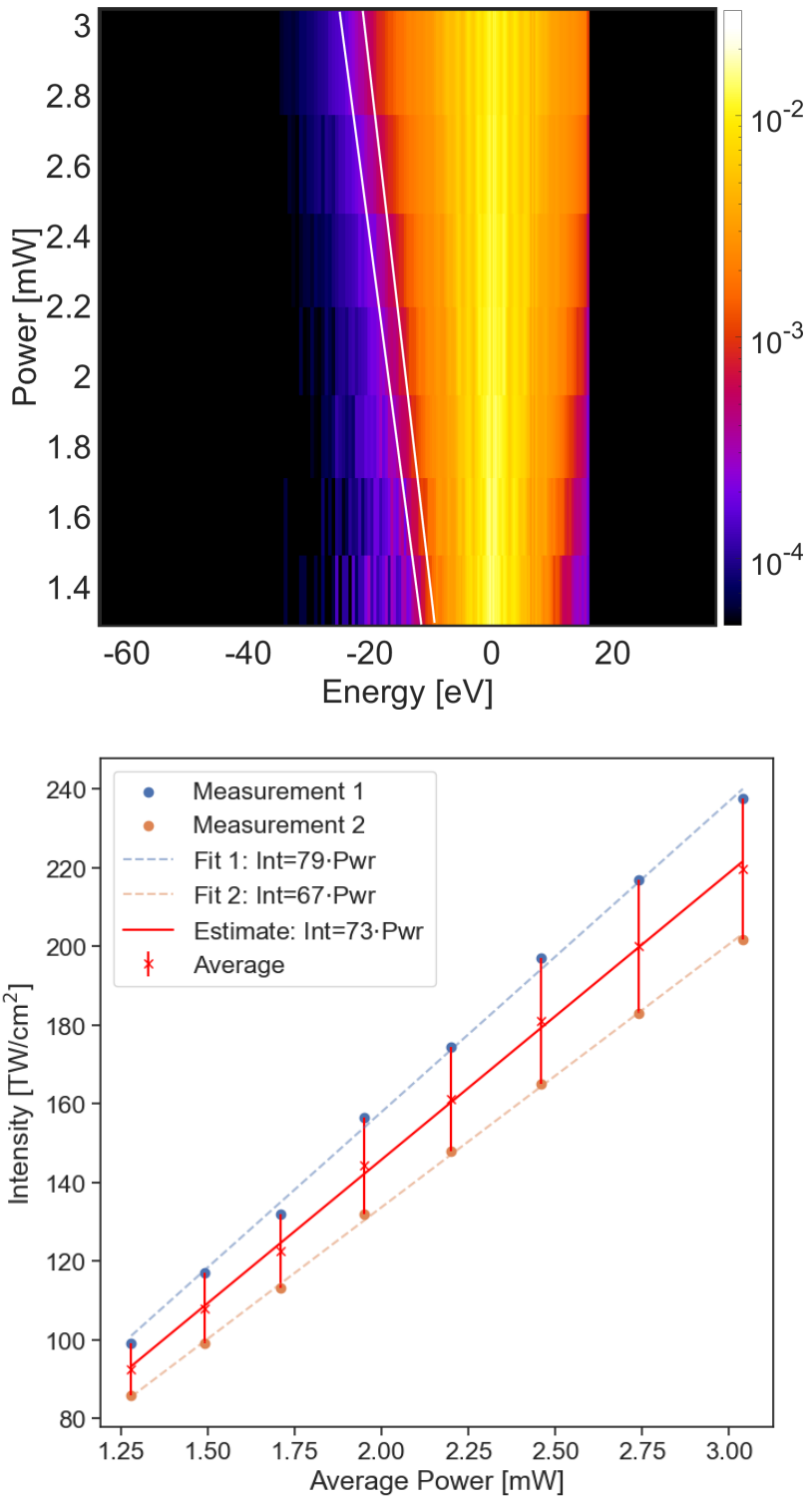

Figure 2.13: Photoelectron spectrum for the above threshold ionization of argon as a function of the average power as measured by the powermeter (Top Panel). Intensity of the laser at focus as a function of the average power (Bottom Panel), giving the calibration of intensity to average power.

From the data presented in Figure 2.13 and using Equation 2.20 we can infer the peak intensity of each measurement. In Figure 2.13 we also plot these inferred intensities as a function of the average power measured by the powermeter. This allows us to determine the calibration parameter between the intensity and the average power:

$$\alpha = (73 \pm 6) \left[\frac{\mathrm{TW/cm^2}}{\mathrm{mW}} \right] \quad . \tag{2.21}$$

In comparison with the naive calculation we performed in Equation 2.17, we see that the experimental value is about a factor of two smaller. This discrepancy is well within the limits of the back of the envelope calculation, which is supposed to provide an order of magnitude estimate. See the discussion around Equation 2.17 for why the naive estimate overestimates the intensity.

Chapter 3

3D Velocity Map Imaging of Electrons

3.1 Introduction

Velocity map imaging (VMI) of electrons and/or ions is a powerful tool for obtaining momentum resolution for charged particles in photo–ionization experiments [46, 50, 54–56]. VMI allows for the measurement of photo–electron spectrum and gives insights into electronic configuration of the molecular system at the time of ionization. VMI technique has been used to measure not only the photoelectron spectrum but also the angular distribution of photoelectrons [57–59]. Furthermore, recording VMI images as a function of pump–probe delay or more generally pulse shapes, allows one to probe the energy differences between different excited states. These can be then compared to theoretical dynamics simulations to yield a holistic understanding of the underlying dynamics [10, 11, 60, 61].

In broad strokes, a VMI system consists of an electrostatic lens, a signal amplifier (Micro–Channel Plates), a phosphor screen that registers the hits and a camera that records an image of the phosphor screen. Normally, the camera is triggered before the arrival of the laser and records an integral over time of the light incident on each pixel. Commercially available frame based cameras however, do not provide exposure times short enough ($\sim$0.1–10 ns) to time

each individual electron or ion hit, therefore, the projection of the 3D momentum cloud onto a 2D surface is recorded. Assuming cylindrical symmetry, 3D information can be obtained by Abel inversion [44, 45].

There are many experimental techniques to circumvent the long integration times of cameras, so that the time of flight of the charged particles can be recorded. One of these techniques is DC slicing, in which the MCPs are only turned on at a given time [62–64]. By changing the time that MCPs are gated, one can "slice" the 3D momentum cloud into 2D images and construct the full 3D cloud in post processing. The main drawback of the slicing technique however, is the data acquisition time. Clearly, k slices require the data acquisition time to be k times longer, which is not desirable. It is much more time efficient to try to resolve the time of flight of charged particles for each laser shot.

As discussed in subsection 2.3.3 the event–driven timepix camera allows one to record time of arrival of each recorded hit with 1.56 ns time resolution [47–49]. In previous works the timepix camera has been used to record the time of flight of ions as well as their 3D momentum [50]. In the case of ions this is a straightforward measurement as their time of flight spread is of the order of hundred nanoseconds.

In the case of electrons however, at usual VMI voltages the time of flight spread is of the order of hundreds of picoseconds, which is too fast for the pixel's ToA resolution. In this chapter we detail how one can stretch the time of flight spread of electrons to about 8 ns and use the second time to digital converter on the camera, which has time resolution of 260 ps, to timestamp arrival time of electrons [65] and thereby recording the 3D momenta of electrons.

3.2 Experimental Setup

In order to demonstrate this novel technique, we measured photoelectron spectrum of xenon in the case of above threshold ionization [52]. For this experiment, we bypass the hollow–core fiber and pulse shaper setup and directly use the 30 fs pulses out of the amplifier. See chapter 2 for details on the experimental apparatus.

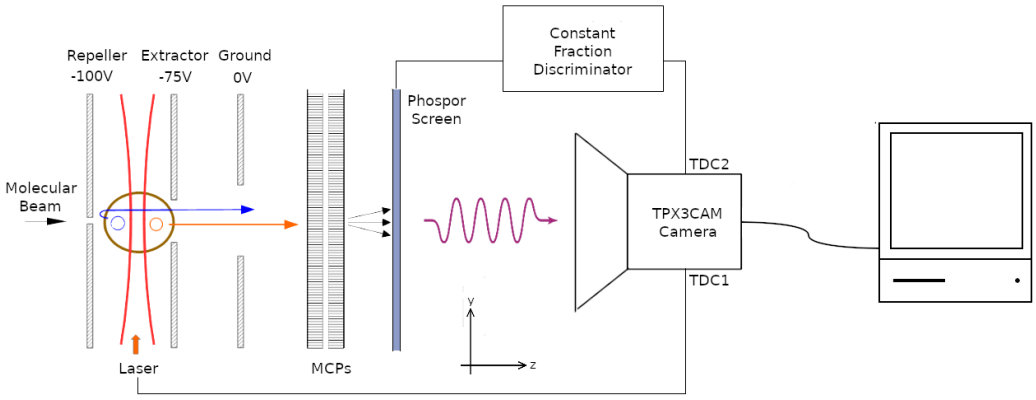

Figure 3.1: Schematic setup to record 3D velocity map imaging of electrons. Created by the author for publication in [65].

We used 30 fs pulses instead of sub 10 fs pulses because we want to observe above threshold ionization (ATI) of xenon. Above threshold ionization from few cycle pulses often produce ATI peaks that are difficult to measure and resolve and thus we choose not to use them for this experiment. The rationale for making use of ATI is two fold: First, it describes a familiar and well studied signal, which helps us debug, develop and test the proposed set–up. Second, ATI produces a photoelectron spectrum with peaks separated by one photon energy. It therefore comes with its own energy scale that we can use to calibrate the timing information into momentum information.

The basic idea behind this technique is to make use of an additional time to digital converter (TDC) on the timepix camera to record the time of arrival of an electron. That being said, even with a TDC with 260 ps time resolution, the time of flight spread of electrons at standard VMI plate voltages (600 V/450 V) is too short (∼1 ns) to record meaningful timing information. We carried out SIMION simulations [66], which numerically calculate the electric field of the VMI plates and subsequently the time of flight of charged particles, in order to determine optimal VMI voltages to maximize the time of flight spread. Since the time of flight spread of electrons are directly controlled by VMI voltages, we opted for lowering the voltages to 100 V/75 V. At these voltages, electrons

have a time of flight spread of about 6 ns, which is still too fast for pixel's 1.5 ns ToA resolution, but perfectly adequate for TDC's 260 ps time resolution. Lowering the VMI voltages to such unconventional voltages have its own drawbacks, which we discuss in detail in section 3.5.

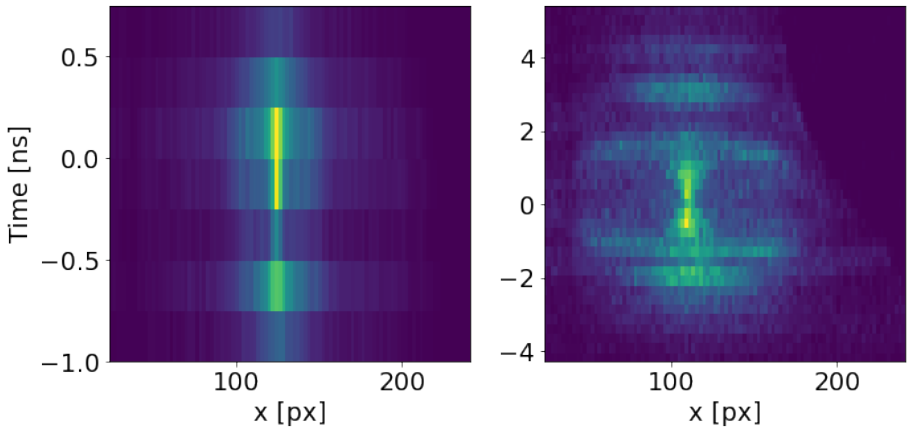

Figure 3.2: Photoelectron yield from above threshold ionization of xenon as a function of time of flight and x momentum for higher VMI voltages (600V/450V) (on the left) and lower (100V/75V) VMI voltages (on the right). Regularly spaced peaks correspond to ATI orders. The time axis is displayed relative to the zero momentum electrons. Created by the author for publication in [65].

In Figure 3.2 we plot the VMI images for higher VMI voltages (left) as well as lower VMI voltages that we used for the experiment (right). The polarization of the incident light is in the time of flight direction so that we can resolve the z–momenta using the time of flight information. We can see that we fail to resolve the time of flight of electrons at high VMI voltages as we predicted from SIMION calculations. For lower VMI voltages, we can resolve the individual ATI peaks using the time of flight information. We recorded two ATI peaks for the faster electrons (i.e. electrons with z–momenta towards the detector) and three ATI peaks for the slower electrons (i.e with negative z–momenta).

Note that we need to maximize the time of flight *spread* of the electrons and not the total time of flight of electrons. While maximizing the total time of flight can be achieved relatively easily, maximizing the time of flight spread is much more difficult. This is because of the following simple kinematic observation: The time of flight spread is solely controlled by the electric field between the first and the second VMI plate. In particular it is given by the time it takes for an electron with momentum in $-z$ direction to turn around and come back to its original position, with a momentum in $+z$ direction with equal magnitude.

In order to record the arrival time of electrons, we capacitatively couple the signal from the phosphor screen[1] to the constant fraction discriminator. The electronic signal on the phosphor screen is much faster than the fluorescence of the phosphor screen and its subsequent measurement with the camera. When there's a hit on the phosphor screen, the voltage on the phosphor screen briefly drops and subsequently there's a small current flowing into the phosphor screen as the power supply brings the phosphor screen back to its set voltage. The capacitative coupling allows us to filter out this signal from the high (3500 V) DC background that the phosphor screen is operating at. This small signal from the phosphor screen is amplified and fed into a constant fraction discriminator. Finally, the signal is converted into transistor–transistor logic with a digital delay generator (SRS DG645) so that it can be used to trigger the TDC on the timepix camera.

The use of a constant fraction discriminator is of paramount importance. The pulse height distribution from the phosphor screen depends on the exact the details of how efficiently the electron signal is amplified in MCPs as well as, how efficiently this amplified signal is converted into light in the phosphor screen. Consequently, the pulses out of the phosphor screen have a broad pulse height distribution. If we used a leading edge discriminator, the timing information would suffer from timewalk effects (cf. Figure 2.12), effectively washing out the 260 ps time resolution we are trying to maintain. A constant fraction discriminator solves this problem as it only turns on when the pulse

[1] We remark that this experiment can equally be performed by capacitatively coupling to one of the MCP. The choice of MCP vs. phosphor screen has no bearing.

reaches a pre–determined fraction of the amplitude of the pulse. Therefore, timewalk effects are greatly reduced.

3.3 Data Analysis

3.3.1 Removal of Multiple Hits

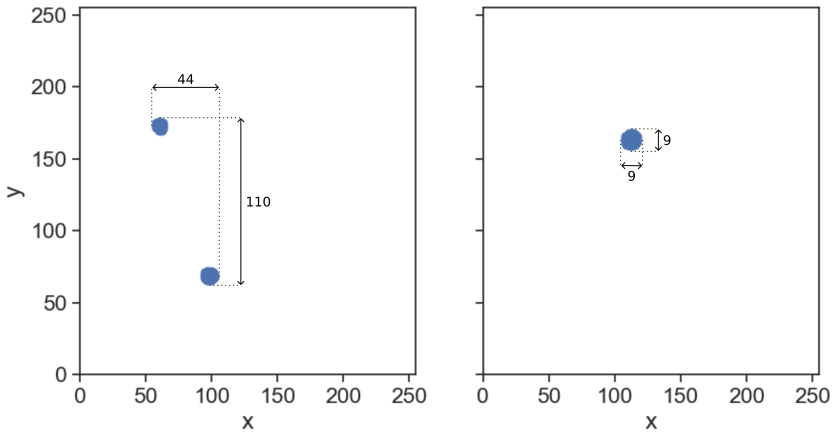

Figure 3.3: (On the left) a multiple hit VMI image that has 44 pixels between the two outer most "on" pixels in the x direction and 110 pixels in the y direction. (On the right) a single hit VMI image that only extends for 9 pixels in x and y directions

The careful reader might have noticed that we use a single TDC that marks the arrival time of electrons. While the camera is endowed with two TDCs with same time resolution, one of the TDCs is used to mark the arrival of the laser shot and thus cannot be used to timestamp electrons. Consequently, we can only measure the time of flight of a single electron. If there is more than one electron hit in a given laser shot, we have no way of distinguishing which electron's time of flight we have measured. In a sense we measure the time of flight of the "first" electron; however, there is no way to determine which electron that leads to separate x,y location on the detector was the "first" one. This is why we need to remove all multiple hit VMI images from the dataset.

While there are many clustering algorithms to determine the number of hits in an image, they are often computationally expensive. Furthermore, these algorithms would count two electron hits that are overlapping as a single hit. The faster and more robust method relies on the following observation: The maximum distance between two "on" pixels in x or y direction for a multiple hit image is larger than a single hit image (cf. Figure 3.3). Therefore, we use the x and y extent of a VMI image to threshold out the multiple hits. In Figure 3.4 we plot the x and y extent of each VMI image for one dataset as well as the threshold we chose to filter out multiple hit events. The threshold was chosen through the visual inspection of individual VMI images, as well as the discarded (i.e. multi–electron) and undiscarded (i.e. single electron) VMI images. Note that most of the laser shots (75%) are single electron events because the partial pressure of the sample in the chamber as well as the intensity was adjusted so that most of the laser shots are single electron events.

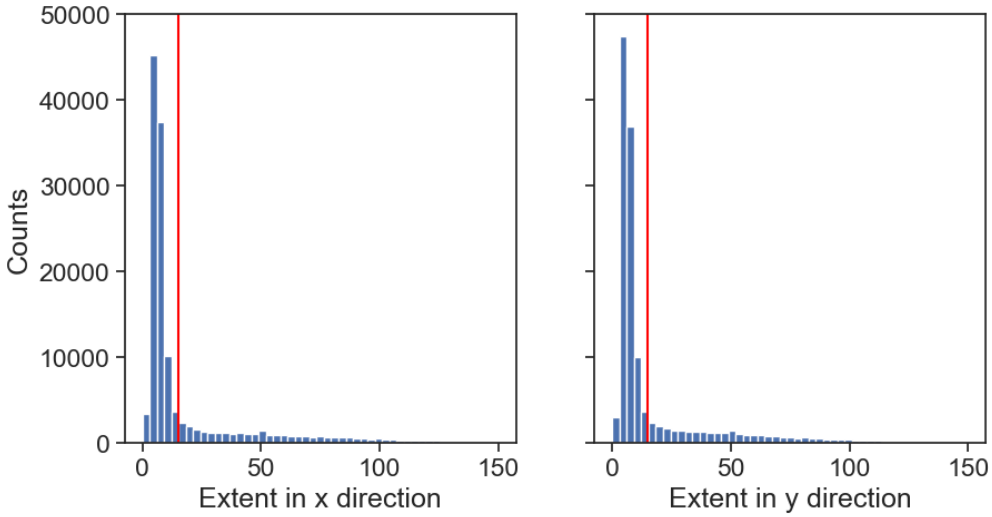

Figure 3.4: Histograms of laser shots showing the maximum distance between two "on" pixels in the x (left) and y (right) direction. The red line indicates the threshold that was chosen to filter out multiple electron events. Consequently, laser shots on the left of the red line are interpreted as single hits and all the rest as multiple hits.

3.3.2 Synchronization of TDC and Pixel Timing

One of the strengths of using one apparatus (timepix camera) to record both the time of arrival of electrons (TDC2) and arrival of laser shot (TDC1) is the relative simplicity of the synchronization of these two times. Had we used two separate devices, one would have to come up with an experimental scheme to identify the two different times, which is a non-trivial proposition because at any given shot one of the signals might go undetected, shifting the stack of times by one and thus, incorrectly identifying different laser shots as the same for all of subsequent laser shots [64]. In our case both of the times (TDCs and pixel time of arrival) is based on the same clock of the camera hence, eliminating a need for a complicated time synchronization scheme.

Still, each TDC2 timing needs to be associated with a TDC1 timing as well as with the timing of each pixel in a given laser shot. Because of the way the data was collected and the camera's internal aggregation of data into packages, it is not necessarily the case that each line of data is chronological even though they are *roughly* chronological. Furthermore, one cannot simply sort the times chronologically because there are limited number of bits used to denote each time and thus, the timing loops back to zero ("overflows") every 26 s for pixels and 107 s for TDCs[2].

We refer to [67] for the full algorithm for the synchronization of these times and provide here the main ideas. We iterate over the pixel timings and associate each pixel timing a candidate TDC1 and TDC2 timing. We posit that the correct TDC1 and TDC2 time must be the one that is locally closest in timing to the pixel timing. We further refine this association by making sure that the assigned times make physical sense i.e. the pixel time of arrival must be larger than the TDC1 timing, which marks the arrival of the laser and comes before the camera records the hits.

[2]The exact number is $(25\,\text{ns}) \times 2^{30}$ for pixel times and $(25\,\text{ns}) \times 2^{32}$ for TDC timing.

```
TDC1: 0.00101496458129883
TDC2: 0.00101969869384766
TOA: 0.0010193421875, ToT: 225, x: 72, y: 205
TOA: 0.0010193484375, ToT: 75, x: 136, y: 176
TOA: 0.0010193515625, ToT: 250, x: 70, y: 205
...
TOA: 0.0010192796875, ToT: 2750, x: 118, y: 39
TOA: 0.001019284375, ToT: 950, x: 117, y: 44
TOA: 0.0010192765625, ToT: 6600, x: 118, y: 42
TOA: 0.0010192796875, ToT: 2325, x: 117, y: 43
TOA: 0.0010192828125, ToT: 1450, x: 117, y: 39
TDC1: 0.00195490598754883
TDC1: 0.00289484713134766
TDC1: 0.00383478853759766
TDC2: 0.00383952578125
TOA: 0.0038391375, ToT: 175, x: 129, y: 188
TOA: 0.0038391375, ToT: 150, x: 132, y: 188
TOA: 0.003839140625, ToT: 125, x: 135, y: 185
TOA: 0.0038391421875, ToT: 175, x: 127, y: 186
TOA: 0.003839134375, ToT: 200, x: 130, y: 188
TOA: 0.0038391296875, ToT: 200, x: 128, y: 187
...
TOA: 0.0038391125, ToT: 4525, x: 131, y: 184
TOA: 0.0038391171875, ToT: 1100, x: 128, y: 184
TOA: 0.0038391171875, ToT: 1525, x: 133, y: 184
TOA: 0.0038391125, ToT: 3575, x: 131, y: 185
TDC1: 0.00477472994384766
TDC1: 0.00571467135009766
TDC1: 0.00665461275634766
TDC2: 0.00665935103759766
TOA: 0.00665895625, ToT: 300, x: 99, y: 152
TOA: 0.0066589578125, ToT: 250, x: 101, y: 154
TOA: 0.006659, ToT: 75, x: 105, y: 154
TOA: 0.00665895625, ToT: 350, x: 102, y: 154
TOA: 0.00665905, ToT: 100, x: 106, y: 153
```

Figure 3.5: Excerpt from raw timepix data. TDC1 timestamps the arrival of laser shots and TDC2 timestamps time of arrival of electrons. Different batches of synchronized TDCs and pixels are shown with different colors. Black TDCs indicate that there were no recorded hits for those laser shots. TDC data is emphasized for easier view.

Furthermore, the difference of pixel ToA and TDC1 and TDC2 timing is constrained to lie within a certain range. For TDC1, the difference of ToA and TDC1 cannot be larger than 0.9 ms as there is a new laser shot every 1 ms. The TDC2 timing should lie much closer to the ToA of the pixels because they are sourced from the same event i.e. hits on the phosphor screen. However, due to finite speed of light in cables these times are not equal. We therefore chose 6 μs for the maximum difference between the ToA and TDC2 times. Of course, the actual difference between ToA on the pixels and TDC1 or TDC2 times are much less than 0.9 ms or 6 μs. These limits we chose are meant to avoid any unphysical assignment of times.

3.3.3 Time of Flight–Momentum Calibration

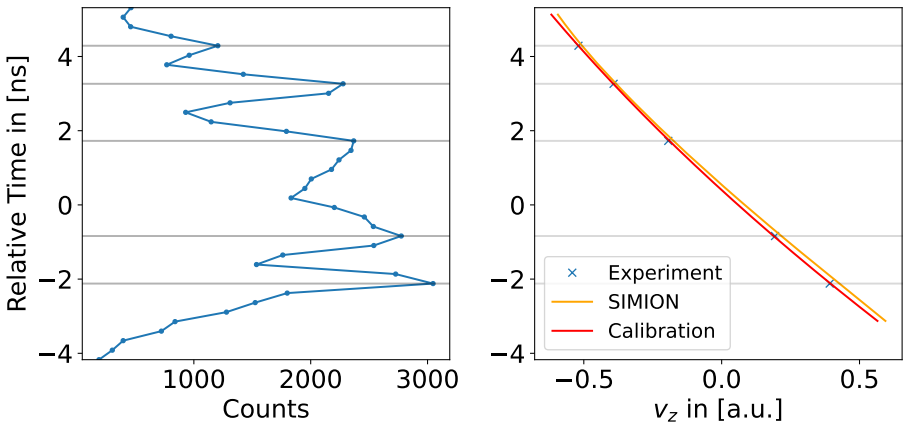

Figure 3.6: Total electron yield resulting from above threshold ionization of xenon as a function of relative arrival time (left) and calibration of relative arrival time to momentum in the z direction (right). See also Figure 3.8 for 2D view of the ATI of xenon with labeled ATI energies. Created by the author for publication in [65].

The time of flight we record for electrons need to be converted into momentum in the z–direction. In order to do this calibration, we first simulated the time of flight of electrons in our VMI setup with 3 plates at voltages -100 V, -75 V

and 0 V using SIMION software [66] assuming that the electrons are created in the middle of the first and second VMI plate. We chose these voltages so that the time of flight spread of the electrons are a few nanoseconds, so that we can sample enough data points with the TDC. We display the resulting calibration in Figure 3.6.

While the SIMION simulation provides good agreement with the measured ATI peaks, we opted for calibrating the velocity to time of flight using the fact that ATI peaks are separated by one photon energy. We chose a second and third order polynomial for this fit and found that the third order fit does not deviate substantially from the second order fit and thus opted to use the second order fit for calibration. Both the SIMION simulations and the resulting calibration are plotted in Figure 3.6.

3.4 Experimental Results

We measure photoelectrons resulting from above threshold ionization of xenon. These electrons have well defined energies that are separated by one photon energy, which we use to characterize and benchmark our experimental method. We performed the experiment at various VMI voltages as well as with two different polarizations. When the polarization is in the direction of the time of flight, we resolve the z momentum using the ToF information (temporal setup). In usual VMI experiments, the polarization is orthogonal to the time of flight direction and the momenta of electrons are resolved spatially on the detector (spatial setup). We can therefore benchmark the temporal setup with the usual spatial setup, as the physics is the same regardless of the direction of polarization.

In Figure 3.7 we present the results for temporal VMI setup. The ATI peaks are resolved using the timing information. Note that we can resolve three ATI peaks in the $-z$–direction and two peaks in the $+z$–direction, which is expected because the electrons in the $-z$–direction take a longer time and thus are easier to resolve. In this measurement we used the VMI voltages we quoted in section 3.2 i.e. 100 V/75 V/0 V. Furthermore, we remark that in the temporal setup the phosphor screen only records the projection onto the x–y plane

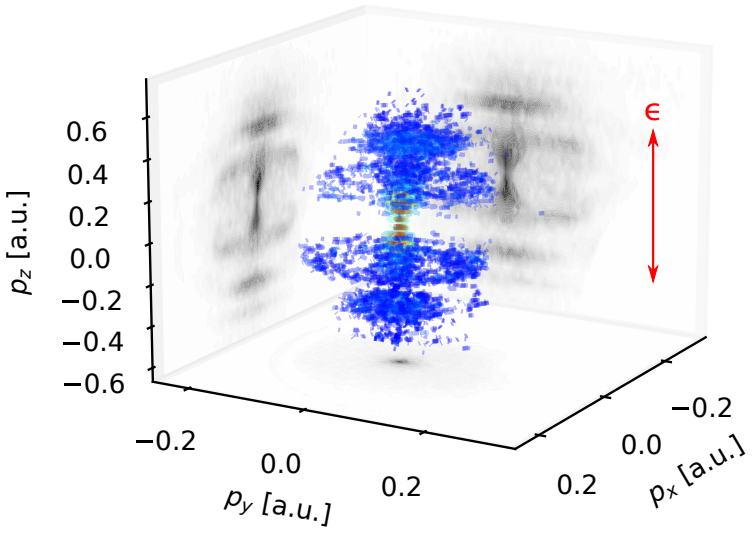

Figure 3.7: Above threshold ionization of xenon. The ATI peaks are resolved using the time of flight of electrons. The laser polarization is in the z–direction (red arrow). The VMI voltages used in this measurement were 100 V/75 V/0 V. Created by the author for publication in [65].

and would only see a central dot depicted in x–y plane in Figure 3.7. We also note the cylindrical symmetry along the axis of laser polarization. This can be seen directly on the depicted momentum cloud as well as from the quantitative similarity of projections on the y–z and x–z planes. The momentum cloud has a slight tilt towards x–direction. We suspect that this is the result of a slight tilt in the laser polarization, which is consistent with the measurements carried out by tilting the polarization 90° (cf. Figure 3.8). We do not expect this tilt to affect any of the results presented in this chapter. That being said, it is remarkable that this tilt could be read off from our measurement.

In Figure 3.8 we compare the temporal and spatial imaging methods. In particular, we see that we can recover the correct ATI energies using temporal imaging without resorting to Abel inversion or cylindrical symmetry. We note however that the spatial imaging method has higher momentum resolution than the temporal imaging method. This is evident from the fact that we have about 40 bins for the time resolution, whereas the camera has 256 pixels

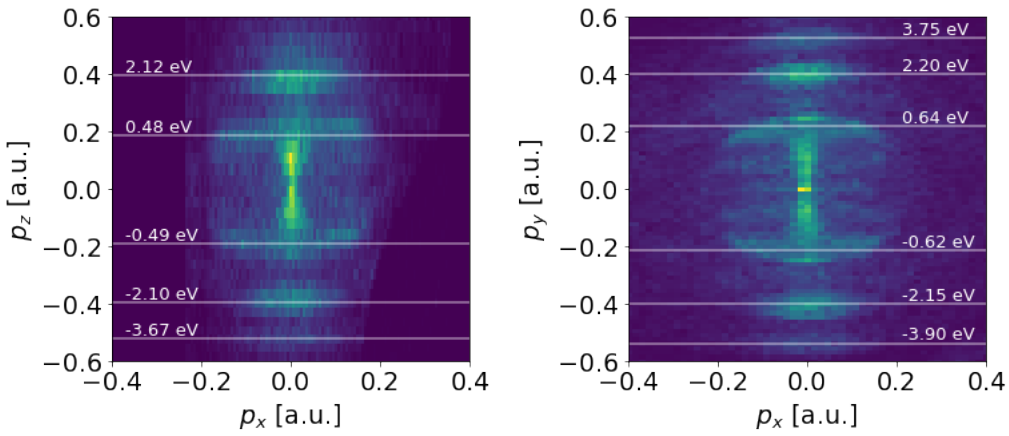

Figure 3.8: Comparison of temporal imaging (left) and spatial imaging (right). For temporal imaging the laser polarization is perpendicular the detector and the momentum along the z–axis is recovered from electron timing. In the case of spatial imaging the electron energies are recovered from the image on the phosphor screen and the polarization is in the plane of the detector. Created by the author for publication in [65].

in both directions. Nevertheless, the quantitative and qualitative agreement shows that our method is a viable method for measuring electron momenta along the time of flight direction.

3.5 Discussion & Comparison to Other Methods

In order to increase the time of flight spread of electrons, we employed very low (100 V/75 V) VMI voltages. For comparison, the rest of the measurements in this thesis uses larger than 600 V for the VMI plates and many VMI apparatus works with even higher voltages (order 1–10 kV). The higher the VMI voltages the larger is the range of energies one can record, which can be understood from simple kinematics. The electrons that have too much momentum in the x or y direction escape the VMI apparatus and do not hit the MCP. Increasing VMI voltages thus allows us to record electrons with higher transverse

momentum because with higher VMI voltages the travel time of electrons is smaller and consequently, they travel less far transversely.

Our method's range of energies in the xy–plane is limited because of the low VMI voltages we had to employ in order to increase the time of flight spread of electrons. There are several ways one can use to increase the momentum range in the plane of the detector. The first one is to use larger VMI plates, which would increase the momentum range linearly with the size of the plates. Alternatively, one can try to decrease the space between the VMI plates and the MCPs, which would also linearly change the momentum range. Finally, a more involved approach would be to employ thick[3] VMI [46, 68]. Using thick VMI, it was demonstrated that the energy range can be improved by 50% and the time of flight spread of electrons by about 300% [46].

Another potential complication with such low VMI voltages is stray electromagnetic fields. We employ in all of our experiment a μ–metal shielding that shield the VMI apparatus as well as the free flight region between the last VMI plate and the MCP from stray magnetic fields. At higher voltages one does not need to worry about stray electric fields, as the electric fields of the VMI plates dominate any other stray electric field. While the concern about stray electric field at lower voltages is valid, we have seen no evidence of stray electric fields distorting the final photoelectron spectrum. To verify this, we compared results from higher VMI voltages (600 V/450 V), to the results from lower voltages and have seen no quantitative difference between them.

One might also worry about the decrease in the detection efficiency of MCPs at lower VMI voltages [69]. The quantum efficiency of MCPs depend on the kinetic energy of the incident charged particle and thus lower voltages result in lower detection efficiency. The manufacturer of the MCPs quote that the quantum efficiency ranges between 70% to 90% in the range 50 eV to 3 keV, which is adequate for our purposes.

[3]The terminology comes from "thin" and "thick" lenses. The standard VMI setup with three plates is considered a "thin" electro–static lens, while more than 3 plates is considered a "thick" lens.

Currently, our setup is limited to single electrons only as we discussed in subsection 3.3.1. This is a severe restriction from the point of view of the physics one can probe with this technique. For example, with this technique we cannot perform a double ionization experiment and record both of the resulting electrons. Even in the case of single ionization, about 30% of the laser shots had to be discarded, which would increase the data acquisition time by about 40% in order to achieve comparable statistics. The development of commercially available next generation timepix cameras will remove this restriction as the pixels on these cameras are expected to have 200 ps time resolution [70–72]

We want to briefly compare our method to cold target recoil-ion-momentum spectroscopy (COTRIMS) [73–78]. In this method, the molecules are introduced using a supersonic molecular beam and thus are cooled to 50 mK in order to create a very small spread of initial momentum of the target ions. After photoionization, electrons and ions are accelerated apart and mapped onto separate position sensitive detectors with the help of electric and magnetic fields. The final momentum of the charged particles can be calculated from their time of flight as well as their final position on the detector [77]. The position and time of flight of electrons are obtained from hexagonal delay line detectors (see Figure 3.9). Similar to our setup, the initial signal from the charged particle is amplified by a stack of MCPs. When the amplified signal of electrons hits the delay line detector, it creates a small current in multiple delay lines that travels along them. By measuring the timing of these currents, one can deduce the distance of the hit along each delay line. Combining the timing of at least two delay lines one can identify the position of the hit uniquely. The third delay line allows for unique identification of multiple hits if the hits are sufficiently spaced out in time or in position [78].

As mentioned previously, our setup allows detection of 3D momentum of a single electron, while the COLTRIMS detector can achieve up two electrons per shot, with partial information available for the third electron. Furthermore, COLTRIMS apparatus has a higher momentum resolution than the VMI techniques employed in this thesis. For instance, in [79] the authors quote that their COLTRIMS apparatus has a momentum resolution of 0.7 a.u. for D^+ ion, whereas our VMI setup has a momentum resolution of about 2.7 a.u. for

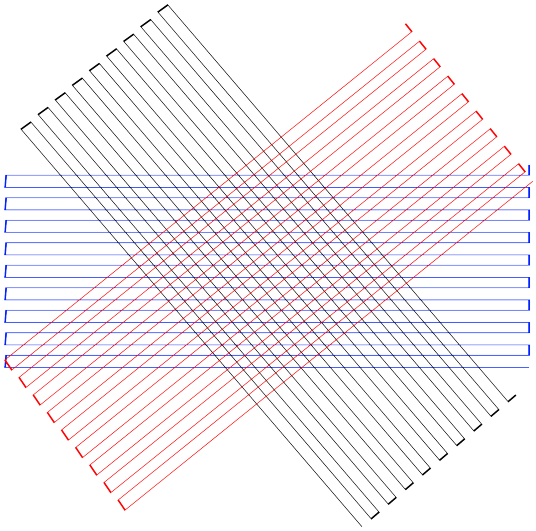

Figure 3.9: Schematic of a hexagonal delay line detector. Each delay line is colored differently to distinguish them from each other.

the same ion [80]. The disadvantage of COLTRIMS apparatus compared to the 3D VMI technique discussed in this chapter is its implementation cost. By making use of the Timepix camera, any VMI system can easily be configured to record the 3D momentum of electrons and ions without changing the rest of the apparatus or the vacuum system. Furthermore, the reconstruction of the momenta for the COLTRIMS apparatus is rather non–trivial, both from the electronics side and from the data analysis point of view (see Figure 2.8 and Appendix D in [77]). Finally, because there are three delay lines in COLTRIMS experiments there is no easy way to convert the COLTRIMS detector to record many electrons per laser shot without big changes to the apparatus, while the new generation of timepix cameras will be able to record many electron shots.

Chapter 4

Covariance Velocity Map Imaging

4.1 Introduction

Coincidence measurements with multiple fragment ions have been used to gain a deeper insight into strong field light–matter interactions [81–89]. Some advantages of recording multiple fragments in coincidencei include the ability to reconstruct molecular frames, measure kinetic energy release of fragments and determine fragmentation channels. As the amount of data and data acquisition times increase, new data analysis techniques are proposed to achieve these objectives. In particular, covariance analysis was introduced in the field of ultrafast science [89–96], which is a tool to study correlations between ionic fragments. This technique later has been refined [97, 98] to control for fluctuations in experimental parameters, such as the intensity of the laser pulses, which is hard to control in free electron X–ray diffraction experiments. The ability of multi–particle covariance/coincidence to resolve fragmentation channels has been widely demonstrated [53, 99–102] as well as the equivalence of the coincidence and covariance techniques [103].

While the covariance technique has been used for up to three fragment ions, the case for 4– and higher particle covariance was an open question in the ultrafast community, due to an important mathematical difference between four and higher covariances. This technique has been recently extended to allow for more than three fragment ions [104–106].

In this chapter we lay the probabilistic foundations of experimental measurements that undergirds the coincidence and covariance measurements. We restrict our discussion to ions as there is a richer probabilistic theory due to different species of ions. We then discuss the background subtraction technique in coincidence measurements and demonstrate its mathematical equivalence to the covariance technique. At the end of the chapter we demonstrate these techniques to study disassociation channels of 1,4–Cyclohexadiene upon multi–photon ionization.

4.2 Probability Theory of Experimental Measurements

Suppose that we are doing a strong field double–ionization experiment on a molecule AB, so that A^+ and B^+ ions are produced. In any given laser shot, the number of A^+ or B^+ fragments fragments is random[1], as this depends on a number of parameters that we cannot possibly control such as the *exact* (not average) number of molecules in the laser focus for every laser shot. Even if we could control it, there are still intrinsic processes that make the exact number of fragments random, such as the non–unit probability of ionizing the molecule and the non–unit detection efficiency of the experimental apparatus. Empirically, however, the number of X^+ fragments N_X is described well by the Poisson distribution [80]. The probability that k number of X^+ ions is observed, is given by

$$\mathbb{P}(N_X = k) = \frac{(\lambda_X)^k e^{-\lambda_X}}{k!} \tag{4.1}$$

The expectation value and variance of a Poisson random variable N_X is well known and is given by the only parameter of the Poisson distribution:

$$\langle N_X \rangle = \mathrm{var}(N_X) = \lambda_X \tag{4.2}$$

[1]Here we use the term "random" in a technical mathematical sense. We say that a quantity X is random, if its outcomes is not deterministic. The "randomness" of X is modeled by Poisson distribution and as such it is not "random" in the colloquial sense.

where the brackets $\langle N_X \rangle$ denote expectation value. In the statistics literature the expectation value is often denoted as $\mathbb{E}[N_X]$ but we stick to the physicist notation and use the angled brackets.

Of course, the average number of X^+ ions i.e. λ_X depends on external experimental parameters such as the partial pressure P of the sample in the vacuum chamber and the intensity of laser light I. The dependence of λ_X on the partial pressure can be described by a linear relationship

$$\lambda_X(kP, I) = k\lambda_X(P, I) \tag{4.3}$$

This relation is a consequence of the fact that the partial pressure of the sample in the vacuum chamber controls the average number of molecules in the laser focus. If we double the pressure in the chamber, the number density of the molecules in the chamber doubles and thus, the average number of molecules in the laser focus. We therefore expect the number of measured X^+ ions to double.

In general, the ionization probability is a nonlinear function of the laser intensity for strong field ionization. Furthermore, the dependence of λ_X on intensity is complicated because at different intensities different physical processes could be taking place. For example, large changes in intensity can push an experiment from the multi–photon regime into the tunneling regime. Nevertheless, in the multi–photon picture, small changes in the intensity can be described by a power law behavior, assuming that the underlying physical process doesn't change under small variations of the intensity. For an n–photon process, the cross–section of photon–molecule interaction is proportional to the n^{th} power of the intensity and thus, we have for small changes in intensity ϵ:

$$\lambda_X(P, (1+\epsilon)I) = (1+\epsilon)^n \lambda_X(P, I) \approx (1 + n\epsilon)\lambda_X(P, I) \tag{4.4}$$

In what follows, we will drop the dependence of λ_X on the pressure and laser intensity for ease of notation.

In general, there could be many different dissociative ionization processes that lead to the production of an A^+ ion and each of these processes is described by its own Poisson distribution. For example, all of the following processes

lead to a production of an A^+: Single ionization resulting in A^+ (λ_{A0}), double ionization resulting in A^+ and B^+ (λ_{AB}), triple ionization that results in A^+ and B^{++} ($\lambda_{AB^{++}}$). For a total number of observed A^+ ions we have[2]:

$$\lambda_A = \lambda_{A0} + \lambda_{AB} + \lambda_{AB^{++}} + \cdots \quad , \tag{4.5}$$

We assumed here that the observations of different processes are statistically independent of each other, which is a physically sound assumption.

For lower laser intensities, a process that produces higher charges is much less likely than the process with fewer charges on the molecule[3]. Thus, we have the hierarchy:

$$\lambda_{A0} \gg \lambda_{AB} \gg \lambda_{AB^{++}} \tag{4.6}$$

This fact is both a blessing and curse in disguise. It means that we can safely truncate the Equation 4.5 after a few terms. The curse is that we are generally interested in the higher order ionization of AB e.g. λ_{AB} term. Therefore, the dominant single ionization term λ_{A0} acts as an unwanted background for λ_{AB}. In what follows, we will discuss experimental methods that aim to get rid of this unwanted background.

4.2.1 Coincidence Technique

A ubiquitous technique of isolating the double ionization term λ_{AB} from the single ionization is the (somewhat obvious) recognition that double ionization produces two ions A^+ and B^+. If we isolate the laser shots in which exactly one A^+ and exactly one B^+ are present *in coincidence*, then we can hope to isolate the double ionization channels. Suppose the probability that the laser pulse singly ionizes a molecule is given by η_1 and that the probability that it doubly ionizes a molecule is given by η_2. Further, suppose that we are performing a

[2]A quick derivation shows that if X and Y are Poisson random variables with parameters λ_X and λ_Y, then the sum random variable $\Sigma = X + Y$ is a Poisson distribution with parameter $\lambda_X + \lambda_Y$. This is the justification of adding λ's in Equation 4.5.

[3]Here we assume that the laser intensity is not so high as to doubly ionize every molecule in the laser focus. The intensity regimes discussed in this thesis do not fall into this category.

strict coincidence experiment, in which all the laser shots are rejected unless they have exactly one A^+ ion and B^+ ion. We denote the number of molecules that are ionized in a given laser shot by N_{ionized}. Assuming that the ionization rates are low i.e. $\lambda_{A0}, \lambda_{B0}, \lambda_{AB} \lesssim 0.05$, we have

$$\begin{aligned}
\mathbb{P}(\text{Background}) &= \mathbb{P}(N_{A0} = 1)\mathbb{P}(N_{B0} = 1)\mathbb{P}(N_{\text{singly ionized}} = 2) && (4.7)\\
&= \lambda_{A0} e^{-\lambda_{A0}}\, \lambda_{B0} e^{-\lambda_{B0}}\, \eta_1^2 && (4.8)\\
&\approx \eta_1^2 \lambda_{A0} \lambda_{B0} && (4.9)
\end{aligned}$$

In the last step we assumed that the count rates are small[4] and thus $e^{-\lambda_{A0}} \approx 1$, which is a good assumption for coincidence experiments. Similarly for the signal, we have:

$$\mathbb{P}(\text{Signal}) = \mathbb{P}(N_{AB} = 1)\mathbb{P}(N_{\text{doubly ionized}} = 1) \approx \eta_2 \lambda_{AB} \tag{4.10}$$

Thus, the ratio of signal to background is given by:

$$\frac{\mathbb{P}(\text{Signal})}{\mathbb{P}(\text{Background})} = \frac{\eta_2}{\eta_1^2}\, \frac{\lambda_{AB}}{\lambda_{A0}\lambda_{B0}} \tag{4.11}$$

As experimentalists, we have control over λ's mainly by varying the pressure in the chamber and thus, the number of molecules that are caught in the laser focus à la Equation 4.3. We have a limited control by varying the intensity of the laser and thus, leveraging the fact that higher photon order processes scale faster with intensity than lower order processes à la Equation 4.4. The probability of singly ionizing η_1 is larger than doubly ionizing η_2 because the focal volume associated with double ionization is smaller than that of single ionization. Consequently, the prefactor η_2/η_1^2 in Equation 4.11 is less than 1.

In the experimental literature the background is astutely called "false or random coincidences" because these are events that seemingly come from double ionization. For this reason, controlling false coincidences is of paramount im-

[4]For reference, $e^{-0.05} \approx 0.95$, by assuming that $e^{-\lambda} \approx 1$, we are *overestimating* the signal to noise ratio.

portance in experimental measurements. There are several ways to control false coincidences. For example, one can use a tighter focusing mirror so that less molecules have the chance to be in the laser focus as the laser focal volume is smaller. One can also work at very low pressures so that the number of molecules in the chamber is minimized[5]. Still, the reader might have the impression that Equation 4.11 combined with the curse of Equation 4.6 dooms the coincidence method because clearly $\lambda_{A0}\lambda_{B0} \ggg \lambda_{AB}$.

At this point it becomes important to recognize that in modern experimental research, we not only count the molecules (i.e. talk about yields) but also have access to the *momentum* of each fragment through the velocity map imaging apparatus discussed in previous chapters. If a molecule AB truly doubly ionized and broke up into two pieces A^+ and B^+, then the sum of the momenta of the A^+ and B^+ ions needs to be zero[6]. Invoking momentum conservation, we can elevate Equation 4.11 to the following one:

$$\left.\frac{\mathbb{P}(\text{Signal})}{\mathbb{P}(\text{Background})}\right|_{\text{mom conserved}} = \frac{\eta_2}{\eta_1^2}\,\frac{\lambda_{AB}}{\lambda_{A0,\,\mathbf{p}}\;\lambda_{B0,\,-\mathbf{p}}} \qquad , \tag{4.12}$$

where the subscripts $\mathbf{p}$ and $-\mathbf{p}$ denote the momentum of the resulting ion. Note that we don't include this subscript for the double ionization term, as the momentum is automatically conserved for true coincidences. For argument's sake suppose that there are $N_{\text{bins}} = 100$ bins for each momentum bin in the x, y and z directions. So we can write, assuming that each 3D momentum bin is populated uniformly, $\lambda_{A0} \approx N_{\text{bins}}^3 \lambda_{A0,\mathbf{p}}$. Thus, for Equation 4.12 we get:

$$\left.\frac{\mathbb{P}(\text{Signal})}{\mathbb{P}(\text{Background})}\right|_{\text{mom conserved}} = N_{\text{bins}}^3\,\frac{\eta_2}{\eta_1^2}\,\frac{\lambda_{AB}}{\lambda_{A0}\;\lambda_{B0}} \qquad , \tag{4.13}$$

which means an improvement of the signal to background by a factor of *million*! This improvement is usually sufficient to bring the signal to background ratio to acceptable levels. Note that the signal to background ratio improves

[5]Note that in Equation 4.11 decreasing the pressure, increases the signal to background ratio.

[6]We here assume that the molecule starts with zero momentum. While this is strictly not true because we perform experiments at room temperature, the momenta of resulting ions are much higher than the initial momentum of the parent molecule. For comparison, $kT_{\text{room}} \approx 25\,\text{meV}$, whereas the ions usually have order several eV energy.

only by N^3_{bins} and not by N^6_{bins}. This is because of the conditional way we pose the question i.e. we suppose that there's an A^+ ion from a single ionization with momentum $\mathbf{p}$ and subsequently look at the probability that there's a corresponding B^+ ion from an independent event, which happens to have $-\mathbf{p}$ momentum.

Despite this tremendous improvement, performing coincidence experiments is challenging and time consuming. Recall that we had to throw out any laser shot, which had more than exactly one A^+ and B^+ ions for what we called *strict* coincidence experiments. We further filtered by momentum conserving ions in the remaining dataset. While one can relax the first assumption using the momentum conservation, the filters we impose on the dataset quickly dwindle the number of viable laser shots. In order to be able to make statistically significant claims about the double ionization, we need a lot of shots in which double ionization takes place. For a 1 kHz laser system, such measurements previously required *days* of data acquisition at low count rates [103]. This technique quickly becomes prohibitive if we want to study a molecule as a function of the pulse shapes like pump and probe delay or the relative phase between the two pulses. Even if a single delay takes only one day of measurement, a pump–probe measurement with 100 delays would take 100 days for 1 kHz laser systems, which is not feasible even for the most dedicated researchers, let alone the fact that controlling all external parameters like laser intensity, pressure in the chamber over such long horizons is very difficult. Even though higher repetition rate lasers are becoming more common [108] and would reduce the data acquisition times significantly, we believe reducing data acquisition times is still an important scientific endeavor.

4.2.2 Covariance Technique

Another approach to remove the unwanted background comes from the realization that we need not be as strict as the coincidence method. The coincidence method is a sharp method, whereas the covariance technique we will discuss is more "fuzzy" and statistical. We note that the "fuzziness" should not be interpreted in an inferior light, as the equivalence of covariance and coincidence methods has been demonstrated in the literature [103]. Instead of discarding laser shots, the covariance method aims to recover the physics of double ion-

ization through statistical means, hence the "fuzziness". In some sense, the laser shots where double ionization does not take place, have information[7] on the background processes and we leverage this information in the covariance method. Consequently, the covariance technique allows us to work in count regimes 10–100 times that of coincidence measurements.

In statistics, the covariance of two random variables X and Y is given by

$$\mathrm{cov}(X,Y) = \left\langle (X-\overline{X})(Y-\overline{Y}) \right\rangle = \langle XY \rangle - \langle X \rangle \, \langle Y \rangle \tag{4.14}$$

where we defined $\overline{X} = \langle X \rangle$ and $\overline{Y} = \langle Y \rangle$. Covariance measures the unnormalized correlation between the random variables X and Y. Importantly, if X and Y are statistically independent, then they have vanishing covariance[8]. Note that covariance is inherently symmetric and bi–linear:

$$\mathrm{cov}(X + \alpha Z, Y) = \mathrm{cov}(X,Y) + \alpha \, \mathrm{cov}(Z,Y) \tag{4.15}$$

which follows from the linearity of expectation values.

If we write, $N_A = N_{A0} + N_{AB}$ and $N_B = N_{B0} + N_{AB}$, then using the linearity of covariance we get:

$$\begin{aligned}
\mathrm{cov}(N_A, N_B) &= \mathrm{cov}(N_{A0} + N_{AB},\, N_{B0} + N_{AB}) && (4.16)\\
&= \mathrm{cov}(N_{A0}, N_{B0}) + \mathrm{cov}(N_{A0}, N_{AB}) && (4.17)\\
&\quad + \mathrm{cov}(N_{B0}, N_{AB}) + \mathrm{cov}(N_{AB}, N_{AB}) && (4.18)\\
&= \mathrm{cov}(N_{AB}, N_{AB}) = \mathrm{var}(N_{AB}) = \lambda_{AB} && (4.19)
\end{aligned}$$

where in the last line we used the fact that different ionization processes are statistically independent of each other.

In the covariance method, the double ionization rate λ_{AB} is recovered in a "background–free", albeit statistical manner! As a consequence, the covariance technique allows us to work with much higher count rates thus enabling

[7] i.e. it tells us what to "ignore"

[8] The converse is not true except in very special cases.

the study of molecular dynamics as a function of the pulse shape (e.g. pump–probe delay). In section 4.3 we discuss the count rate regimes that is needed for different covariance experiments.

Note also that we didn't throw away any unwanted laser pulses. In fact, *all* of the laser shots play a role as we need to determine the statistics of single ionization (i.e. background) as well as double ionization and we cannot discard any laser shots. Even the laser shots with no recorded ions play a role, as they are used to estimate the statistics of both processes.

So far we have only discussed the covariance technique for two–body dissociation. We can extend the defintion of covariance to 3– and 4–body disassociation in a straight forward manner by generalizing Equation 4.14.

For 3–body covariance we define:

$$\mathrm{cov}(N_A, N_B, N_C) := \left\langle (N_A - \overline{N}_A)(N_B - \overline{N}_B)(N_C - \overline{N}_C) \right\rangle \tag{4.20}$$

Note that this time $N_A = N_{A0} + N_{AB} + N_{AC} + N_{ABC}$ and similarly for N_B and N_C and we are after the statistics of N_{ABC}, the triple ionization channel. In Appendix C, we show that this 3–body covariance indeed yields the triple ionization rate i.e. $\mathrm{cov}(N_A, N_B, N_C) = \lambda_{ABC}$.

Having done 2– and 3–body covariances, one would hope that the higher order covariances follow. Unfortunately, this is not the case. For example the 4–body covariance formula is given by [104–106]:

$$\lambda_{ABCD} = \mathrm{cov}(N_A, N_B, N_C, N_D) - \mathrm{cov}(N_A, N_B)\mathrm{cov}(N_C, N_D) - (2 \text{ similar terms}) \tag{4.21}$$

The intuition behind this formula comes from the fact that four–fold covariance can be a result of two body covariance between pairs of fragments. In a sense, two pairs of fragments can be correlated and this would yield a four–fold covariance, even though all four of the fragments are not correlated. The subtraction in Equation 4.21 ensures that this "spurious" correlation is subtracted out.

This can be seen rigorously from the derivation in Appendix C as well. In the derivation, we used the fact that $\langle (X - \overline{X}) \rangle = 0$ and some terms consequently vanished. In the four–fold case one is left with terms like $\langle (X - \overline{X})(Y - \overline{Y}) \rangle$, which doesn't vanish and give rise to the subtraction terms above in order to yield the quadruple ionization term.

4.3 Real Experiments and Estimators

In real experiments we don't have access to any random variables like N_A. They are mathematical objects that exist in our minds[9]. We can only *estimate* what the statistics of a random variable N_A is through repeated experimental measurement. As a familiar textbook example (see e.g. [107]), we want to briefly discuss how we can estimate the mean of a distribution through repeated measurement in order to introduce the language of estimators, before introducing them in the case of covariance.

Taking a step back, suppose that a random variable with a given probability distribution X has mean μ. How would we "know" that X has indeed mean μ? We would look at repeated observations of X and average them[10]. Each observation X_i is of course a random variable with the same distribution as X and averaging these observations lead to an *estimate* of μ. In concrete terms, computing the average over N repeated observations amounts to:

$$\hat{\mu} = \frac{1}{N} \sum_{i=1}^{N} X_i \qquad , \tag{4.22}$$

which is again a random variable i.e. the exact value of the mean computed is random because X_i are random variables themselves. Since $\hat{\mu}$ is a random variable, we can talk about its expectation value. The expectation value of $\hat{\mu}$

[9] Plato's allegory of the cave can help us understand this. Mathematical objects N_A "cast their shadow" on real world as outcomes of measurements.

[10] One can think about a coin flipping experiment. If I have a possibly biased coin, I can estimate the probability of heads coming up by flipping it many times.

is given by:

$$\langle \hat{\mu} \rangle = \frac{1}{N} \sum_{i=1}^{N} \langle X_i \rangle = \frac{1}{N} \sum_{i=1}^{N} \mu = \mu \tag{4.23}$$

We can also compute the variance of $\hat{\mu}$ as well. One can show that

$$\mathrm{var}(\hat{\mu}) = \frac{\sigma_X^2}{N} \qquad , \tag{4.24}$$

where σ_X^2 is the variance of X. Therefore, with repeated measurement, we can improve the estimate of μ through averaging. In other words, the uncertainty we have on μ reduces with repeated measurement.

The random variable $\hat{\mu}$ is called an *estimator*, as it estimates the actual mean μ of the random variable X. In the statistics literature estimators are often denoted with hats. Furthermore, the property that $\langle \hat{\mu} \rangle = \mu$ implies that $\hat{\mu}$ is unbiased i.e. the estimator $\hat{\mu}$ estimates the correct mean μ *on average*.

Note that there could be many different unbiased estimators that estimate the same quantity. In this sense the choice of an estimator is a *choice* made by the experimentalist and one has the freedom to choose other estimators, if those estimators fulfill a particular property. For example, we could have chosen a rather "silly" estimator and declared $\hat{\mu}_S := X_1$. This estimator still satisfies $\langle \hat{\mu}_S \rangle = \mu$ and is thus unbiased, however the variance of this choice of estimator does not improve with repeated measurement for obvious reasons: $\mathrm{var}(\hat{\mu}_S) = \sigma_X^2$. In this sense, $\hat{\mu}$ is a superior estimator than $\hat{\mu}_S$ because it has lower experimental uncertainty.[11]. We remark however that the second estimator is computationally much cheaper $\mathcal{O}(1)$, than the standard estimator, which scales as $\mathcal{O}(N)$. While this is not a good enough reason to choose the

[11] In statistics literature one would say that $\hat{\mu}$ is a *uniformly better estimator* than $\hat{\mu}_S$ because $\mathrm{var}(\hat{\mu}) < \mathrm{var}(\hat{\mu}_S)$ for $N > 1$. The question of which estimator is the uniformly minimum-variance unbiased estimator (UMVUE), or whether it exists at all for a given statistical quantity is an interesting question in the field of estimation theory. Interestingly, one cannot produce an estimator with arbitrarily low variance. According to Cramér–Rao bound, the variance of an estimator $\hat{\theta}$ and the Fisher information $\mathcal{I}(\hat{\theta})$ of that estimator satisfy (under certain mathematical conditions) an uncertainty relation: $\mathrm{var}(\hat{\theta})\,\mathcal{I}(\hat{\theta}) \geq 1$

latter estimator, it is important to weight different aspects of estimators such as computation times and rate of convergence while choosing one.

***

In the previous section we discussed the covariance method. Being a statistical method, the real observed quantity is the *estimator* of the covariance, which has its own variance i.e. uncertainty. The natural estimator of covariance of two random variables X, Y is given by:

$$\widehat{\mathrm{cov}}(X,Y) = \frac{1}{N}\sum_{i=1}^{N} X_i Y_i - \frac{1}{N^2}\left(\sum_{i=1}^{N} X_i\right)\left(\sum_{i=1}^{N} Y_i\right) \tag{4.25}$$

$$= \frac{1}{N}\sum_{i=1}^{N} X_i Y_i - \hat{\mu}_X \hat{\mu}_Y \tag{4.26}$$

Usually the unbiased estimator for covariance has a $1/(N-1)$ in the denominator instead of $1/N$, similar to the case of sample vs. population variance. However, since we are averaging over hundreds of thousands of laser shots, the difference is negligible and we opt for using $1/N$ for notational brevity.

Note that making the leap from the abstract definition of covariance in Equation 4.14 to the estimator in Equation 4.25 has the advantage that the latter formula spells out exactly how the data analysis code should be written. If we are interested in calculating $\widehat{\mathrm{cov}}(N_A, N_B)$, we have to calculate the two terms in Equation 4.25. For the first term, we would multiply the number of A^+ and B^+ ions in any given shot, then take the average of this product over all laser shots. The second term just subtracts the product of the mean of A^+ and B^+ ions from the first term. This subtraction yields the estimated covariance between the two fragments.

4.3.1 Uncertainty of the Covaraince Estimator

We are interested in understanding the uncertainty of the covariance estimator $\widehat{\mathrm{cov}}(N_A, N_B)$. In other words, we want to obtain the variance of the covariance

estimator. While this can be done analytically [104] with various simplifying assumptions, we opt for a numerical estimate of the uncertainty by running a Monte–Carlo simulation, which we detail below [105, 106].

In order to carry out the Monte–Carlo simulation, we need to decide on the λ's for each process i.e. $\lambda_{A0}, \lambda_{B0}$ and λ_{AB}. In the most ideal case[12], we would only have double ionization λ_{AB} and no single ionization i.e. we set every λ other than the highest order lambda to zero. This gives us a lower bound on the uncertainty that we can expect.

In Figure 4.1 we plot the Monte–Carlo results for this case. We can see that the Mone–Carlo simulation and the analytical calculations from [104] are in agreement. For 2–fold covariance, the noise to signal ratio decreases with increasing λ. For 3– or 4–fold covariance, the noise to signal ratio has a minimum before $\lambda_{max} < 0.5$ and then starts rising slowly in the case of 3–fold covariance and rather sharply in the 4–fold covariance. This makes it evident that the number of hits per laser shot is a very important parameter to control, especially in the cases of 3– and higher–fold covariances.

Often in real experiments, we cannot turn off lower ionization channels like we did in the above simulations. In order to see the effects of these lower ionization channels on the noise to signal ratio, we extend our Monte–Carlo simulations to include these channels. To that end we set the double ionization term to 1 and we fix the remaining parameters randomly from a uniform distribution over the range $[0.5, 1.5]$. This gives us a uniform ionization rate for all of the ionization channels as a starting point[13]. In order to reflect the curse of double ionization we discussed in Equation 4.6, we multiply λ_{A0} and λ_{B0} by a predetermined factor so that λ_{AB} is at least a factor of 5 smaller than the single ionization λ's. If we run this simulation for e.g. triple ionization, then we would multiply the second ionization λ's by this factor and the single ionization λ's by the square of this factor. In essence, we are creating a geometric hierarchy of λ's pursuant to Equation 4.6. Lastly, in order to simulate the

[12] This is likely experimentally not realizable.

[13] The particular choice of these lower order ionization channels play no role and therefore, we choose them "randomly" instead of picking particular values by hand.

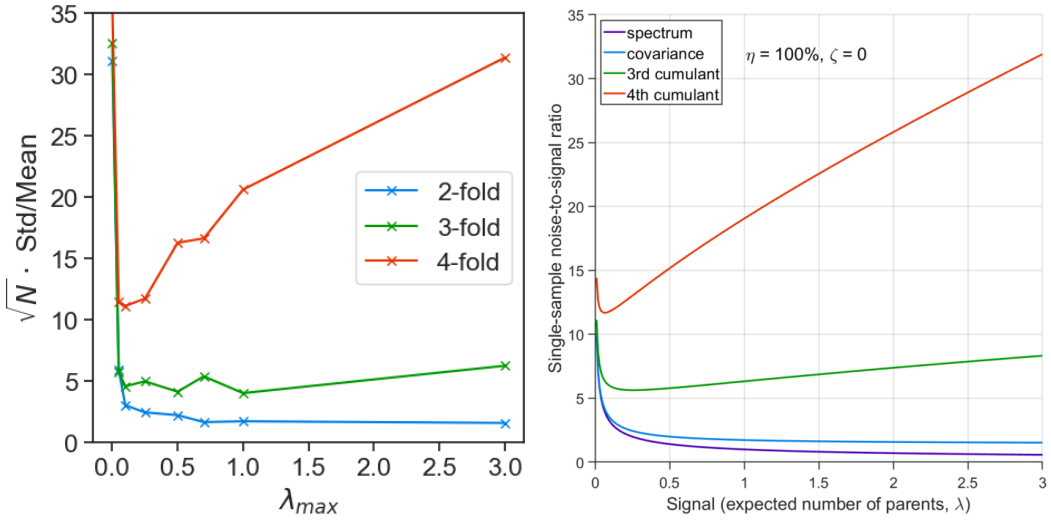

(a) Monte Carlo Simulation

(b) Figure 3 from [104]

Figure 4.1: The single shot noise to signal ratio obtained as a function of the expected number of higher ionization channel λ_{AB} for 2–fold, λ_{ABC} for 3–fold and λ_{ABCD} for 4–fold covariance in the case where only these highest fragmentation channels are turned on. Figure (a) shows the Monte–Carlo Simulation and figure (b) shows the analytical results from [104] (reproduced with permission)

effects of number of hits per laser shot on the uncertainty, we multiply all of the λ's by a "pressure factor" à la Equation 4.3. In an actual experiment, one would change the pressure in the vacuum chamber in order to yield a desired count rate, hence the name "pressure factor". We then count the number of A^+ ions and B^+ ions in all of the laser shots, so that in the end we have a dataset of number of A^+ and B^+ ions with "unknown" double ionization rate λ_{AB}. We then estimate this value using the covariance method. A numerical experiment consists of drawing $N = 500,000$ samples from this distribution and subsequently estimating the highest ionization term. We subsequently repeat an experiment with the same λ's 30 times in order to estimate the variance.

Note that this simulation scheme describes the worst case scenario because

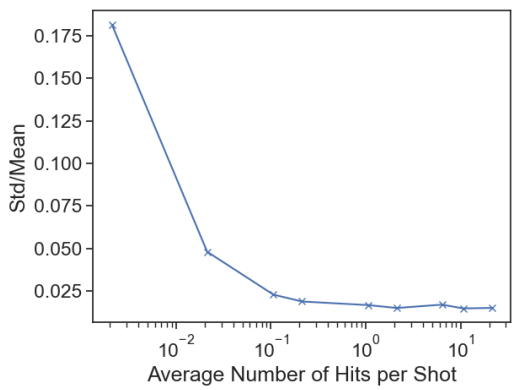

(a) 2–fold covariance

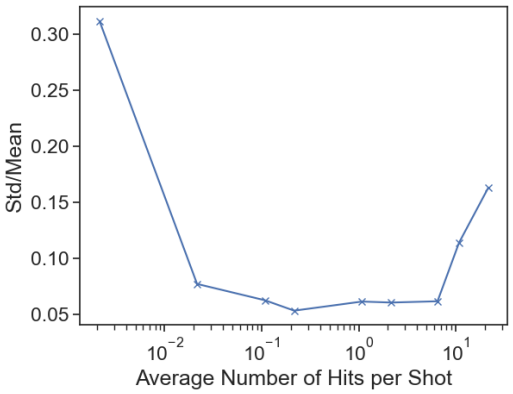

(b) 3–fold covariance

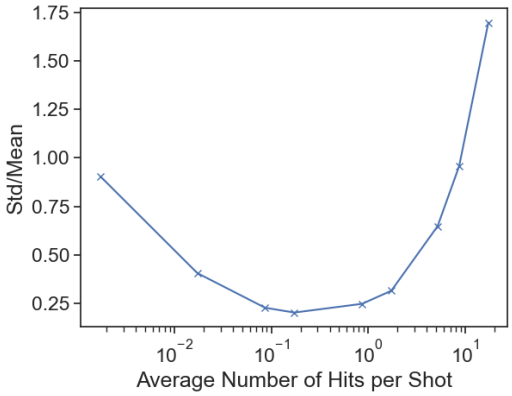

(c) 4–fold covariance

Figure 4.2: Monte Carlo simulation results for noise to signal ratio for the 2,3 and 4–fold covariance technique as a function of average number of hits per shot.

we turned on *all* of the background lower ionization channels. In any given molecular system, it is very likely that only some of the background lower ionization channels will be realized. By comparing the most optimistic regime with the most pessimistic regime, we can get a better understanding of the range of experimental uncertainty. In Figure 4.2 we display the results of the simulation with all of the background lower ionization channels turned on. On the x–axis we plot the number of average hits per laser shot. We plot average

hits per shot as it is the experimental parameter we have most direct access to, unlike λ_{max} the average number of highest ionization channel. Furthermore, on the y–axis we plot the absolute noise to signal ratio, rather than the single shot noise to signal ratio, which is greater by a factor of $\sqrt{N}$.

We see that in the case of 2–fold covariance, the signal to noise improves with average number of hits per shot with diminishing return above 1 hits per shot. In experiments, we typically aim for around 10 hits per shot, as this provides ample statistics without overwhelming the detector. The cases for three and four fold covariance are more interesting and show an increase in the noise with increasing number of hits per shot. In Figure 4.2b we see that the optimal hits per shot for 3–fold covariance is around 0.1 to 10 with the minimum around 0.2. For this reason, we generally do not exceed 10 hits per shot when performing 3–fold covariance experiments. For 4–fold covariance, the noise scales much faster than the previous two cases, with optimal hits per shot being around 0.1. Therefore, if we are performing an experiment to probe 4–fold fragmentation of a molecule, keeping the number of hits per shot below 5 is of paramount importance.

4.4 Background Subtraction for Coincidence Measurements

As we discussed in subsection 4.2.1, performing coincidence experiments can be very time consuming. For this reason, the coincidence community has devised a background subtraction scheme to subtract the false coincidences. To the author's knowledge the first time this background subtraction scheme is discussed in [86] but has been in wide usage since [85, 109–111].

Suppose we want to do a coincidence experiment with ions A^+ and B^+. Let's assume that in the preprocessing step all of the events with multiple A^+ ions or B^+ ions are removed, so that $N_A, N_B \in \{0, 1\}$. In this case the quantity $N_{A,i}\, N_{B,i}$ indicates whether there was a coincident A^+ and B^+ in the laser shot i, as it is non–zero if and only if $N_{A,i}$ and $N_{B,i}$ are both equal to 1. It is then

natural to average this quantity over all laser shots:

$$\text{RawCoincidence} = \frac{1}{N}\sum_{i=1}^{N} N_{A,i}\, N_{B,i} \tag{4.27}$$

Of course, this quantity overcounts because there could be plenty of false coincidences. The idea for the subtraction of the false coincidences is as follows: If we picked an A^+ ion from laser shot i and B^+ ion from laser shot $i+1$, they are necessarily uncorrelated. Therefore, the quantity $N_{A,i}N_{B,i+1}$ gives an estimate of the false coincidences. One can then subtract this quantity with a parameter α that is matched experimentally to minimize the false coincidences (see Supplementary Information in [85]).

$$\widehat{C} := \frac{1}{N}\sum_{i=1}^{N} N_{A,i}\, N_{B,i} - \frac{\alpha}{N}\sum_{i=1}^{N} N_{A,i}\, N_{B,i+1} \tag{4.28}$$

The Equation 4.28 looks very similar to the covariance estimator in Equation 4.25. In fact, $\widehat{C}$ *is* an estimator of the covariance. We can see this by taking the expectation value of $\widehat{C}$:

$$\left\langle \widehat{C} \right\rangle = \frac{1}{N}\sum_{i=1}^{N} \langle N_{A,i}\, N_{B,i}\rangle - \frac{\alpha}{N}\sum_{i=1}^{N} \langle N_{A,i}\, N_{B,i+1}\rangle \tag{4.29}$$

$$= \frac{1}{N}\sum_{i=1}^{N} \langle N_{A,i}\, N_{B,i}\rangle - \frac{\alpha}{N}\sum_{i=1}^{N} \langle N_{A,i}\rangle\ \langle N_{B,i+1}\rangle \tag{4.30}$$

$$= \frac{1}{N}\sum_{i=1}^{N} \langle N_{A,i}\, N_{B,i}\rangle - \frac{\alpha}{N}\sum_{i=1}^{N} \mu_A\mu_B \tag{4.31}$$

$$= \frac{1}{N}\sum_{i=1}^{N} \Big(\langle N_{A,i}\, N_{B,i}\rangle - \mu_A\mu_B \Big) - (\alpha-1)\mu_A\mu_B \tag{4.32}$$

$$= \text{cov}(N_A, N_B) - (\alpha-1)\mu_A\mu_B \tag{4.33}$$

In step 2 we used the fact that different laser shots are statistically independent and in the last step we used the definition of the covariance (Equation 4.14).

Note that this estimator is a *biased*[14] estimator of the covariance for $\alpha \neq 1$. The bias is given by

$$\text{Bias}(\widehat{C}) := \left\langle \widehat{C} \right\rangle - \text{cov}(N_A, N_B) = (1-\alpha)\mu_A\mu_B \tag{4.34}$$

If μ_A and μ_B are less than 1, and α is close to 1, the bias of the estimator could be negligible. Furthermore, it is not obvious, whether this bias plays any role in experimental measurements. Both covariance and coincidence background subtraction techniques are tools to understand and isolate a fragmentation channel, so the adequacy of estimator depends on the use case. If one wants to study the branching ratios of various fragmentation channels, the bias might play a role especially at higher count rates. If one is interested in dynamics of a particular channel, it might not play any role, apart from reducing the contrast of the signal.

4.5 A Study of Photo–ionization with Covariance

So far we have been only concerned with the number of ions of a given species i.e. the yield of an ion species. As we have outlined in subsection 2.3.2, we record the 3D momenta of ions, which leads to a refinement of the covariance technique we outlined. We can simply upgrade the yield N_A to a momentum resolved yield $N_{A,\mathbf{p}}$ and still utilize all of the covariance formalism.

In practice, we rarely look at two–particle covariance, where both particle's 3D momentum are resolved, as this produces a 6D plot that is hard to visualize and interpret[15]. Instead, we often isolate one direction of the momentum

[14] The word "bias" has negative meaning in colloquial usage (e.g. biased media outlet). Here we use the word bias in strictly statistical terms and do not take a position on which estimator is a better one. In fact, one of the recent publications that the author co–authored uses an estimator of this type [105, 106], as it was computationally cheaper to implement.

[15] At least it is hard for humans to interpret, machine learning methods might play a role in understanding such refined quantities.

of both fragments e.g. $\mathrm{cov}(N_{A,p_z}, N_{B,p_z})$. Alternatively we can look at 2D spectrum of one fragment *in covariance* with another. Mathematically, this amounts to a covariance of the form $\mathrm{cov}(N_{A,\mathbf{p}}, N_B)$. In general, one can apply this technique to any observable that can be constructed out of the momenta of the fragments, such as the angle between them or the total kinetic energy release from both particles.

4.5.1 ToF-ToF Type Covariance

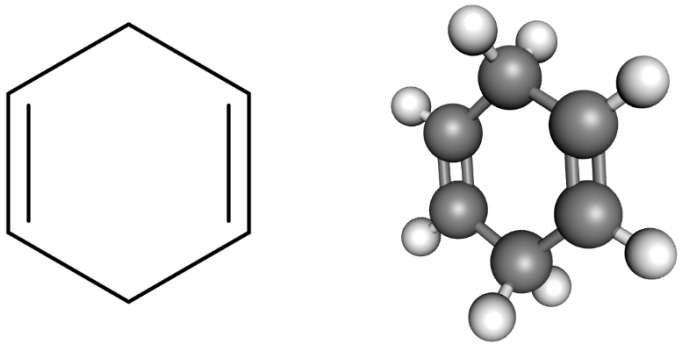

Figure 4.3: Chemical Formula (left) and ball and stick figure (right) of 1,4 Cyclohexadine where gray atoms refer to carbon and white atoms to hydrogen.

For setting experimental parameters, as well as understanding the resulting dynamics, one of the most useful two–fold covariance is the time of flight resolved one. Recall that time of flight is used to identify the ion species as well as for reconstructing its momentum in the z–axis. Therefore, the ToF–ToF covariance gives an overview of possible fragmentation channels we might be inducing for given experimental parameters.

We performed a strong field ionization experiment on 1,4–Cyclohexadiene (1,4–CHD), which has the chemical formula C_6H_8 and is depicted in Figure 4.3. We use 30 fs pulses out of the amplifier at 2 mW average power, which approximately corresponds to $50\,\mathrm{TW/cm^2}$ laser intensity at focus. The background pressure in the chamber was 3×10^{-10} Torr and the sample pressure in the

chamber was at 9×10^{-9} Torr. On average, there were about 2 hits per laser shot and the entire dataset was taken for one hour.

In Figure 4.4 we present the ToF–ToF covariance as well as the mass calibrated version of it for easier identification of fragments. At a glance, there are several features one can identify. First of all, the plots are symmetric along the diagonal, which is reflected in the symmetry of the covariance function. Second, there are circular blobs with non–zero covariance (V–VIII), as well as much more prominent anti–diagonal lines (I–IV). Finally, there are apparent correlations that much less prominent e.g. around IX. We discuss each of these features and their physical meaning below. A summary of the peaks and possible fragmentation channels that these peaks correspond to, can be found in Table 4.1. We will motivate and discuss these assignments in the rest of this chapter.

Peak	Mass/Mass Location	Break–up Channel Candidates
Ia	65/15	$C_5H_5^+/CH_3^+$
Ib	63/15	$C_5H_3^+/CH_3^+$
II	53/27, 52/27, 52/26	$C_4H_x^+/C_2H_x^+$
III	39/39	$C_3H_3^+/C_3H_3^+$, Br^{++}/Br^{++}(unlikely)
IV	39/15	Br^{++}/CH_3^+(?)
V	38/14	$C_3H_2^+/C_2H_3^+/C_1H_2^+$
VI	27/14	$C_3H_2^+/C_2H_3^+/C_1H_2^+$
VII	38/27	$C_3H_2^+/C_2H_3^+/C_1H_2^+$
VIII	27/27	$C_2H_3^+/C_2H_3^+/C_2H_x^+$

Table 4.1: Summary of break–up channels for 1,4–Cyclohexadine

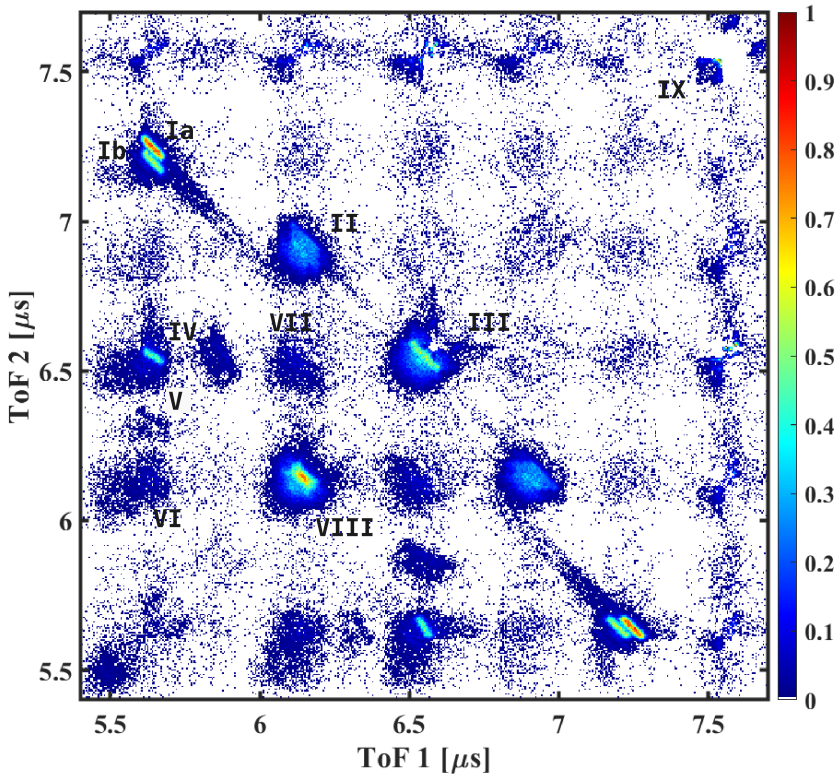

(a) Time of Flight–Time of Flight covariance

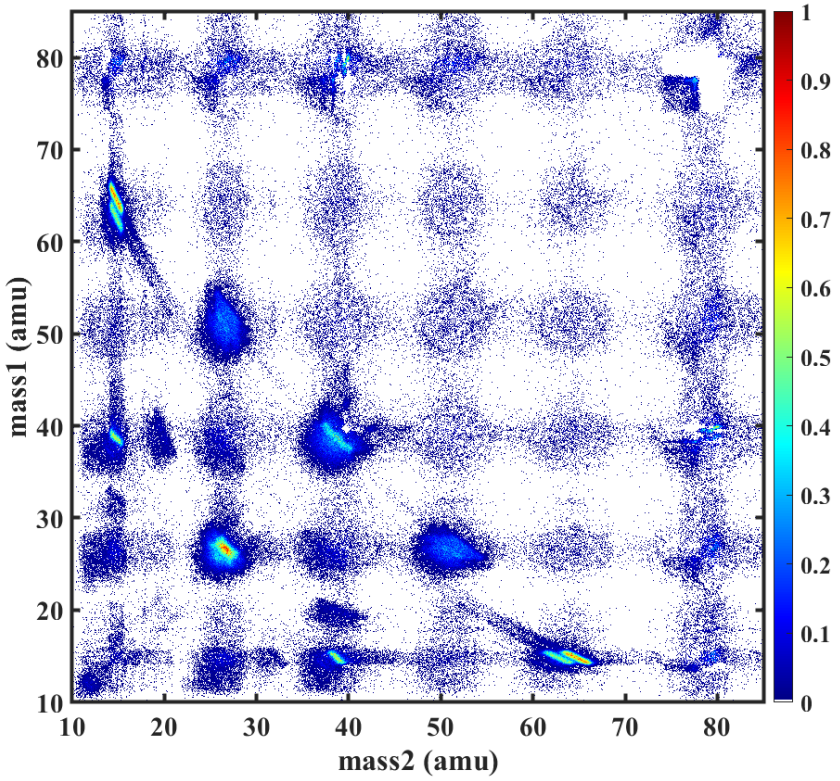

(b) Corresponding Mass–Mass covariance

Figure 4.4: Time of Flight–Time of Flight covariance of strong field ionization of 1,4 Cyclohexadine. The experiment was performed with a single 30 fs pulse with approximate intensity of 50 TW/cm^2.

We first start with the spurious correlations, which are an artifact of the statistical tool we are using and use peak IX as an example of such a spurious correlation. This peak, would correspond to a correlation of a fragment with mass 78 amu with another fragment with the same mass. Clearly, since the parent molecule has mass 80 amu, there cannot be two fragments with mass 78 amu that correlate. In fact, this is the reason that the upper diagonal of the plot is largely empty because any correlation above the diagonal correspond to two fragments, whose masses added together exceed the parent molecule mass. Because of the statistical nature of the covariance technique, we can only achieve zero covariance *statistically*. This means that in the limit of infinite number of laser shots, we would indeed get zero correlation and for finite number of laser shots, we are left with fluctuations around zero. In the introduction we referred to the "fuzziness" of the covariance technique, this is precisely how this "fuzziness" manifests itself in actual experimental measurements. In what follows, we will ignore these unphysical correlations.

One of the most prominent features in Figure 4.4 are the anti–diagonal lines (I-IV). These anti–diagonal lines are a consequence of momentum conservation and indicate that there is a two–body dissociation. If the parent molecule breaks up into two fragments, the fragment momenta satisfy[16] $\mathbf{p}_A + \mathbf{p}_B = \text{const} \approx 0$, which is a result of momentum conservation as the parent molecule has negligible momentum. We note that such momentum conserving anti–diagonal lines might also appear, if there is a three body break–up such that the third body does not carry away significant momentum. We can check whether a break–up is truly two body break–up by adding the masses of the fragments and comparing the sum to the mass of the parent molecule.

Finally, there are circular blobs (V–VIII), which indicate break–ups into more than two bodies, where each body carries comparable momentum. In Figure 4.4 we can identify two of the three fragments but the third fragment is difficult to determine without further analysis. In order to interpret and identify these channels, we resort to three–fold covariance technique on the same

[16] In reality the parent molecule starts with some thermal energy $kT_{\text{room}} \approx 25\,\text{meV}$, however this is negligible compared to order several eV that the fragments carry as a result of the fragmentation.

dataset and discuss these channels in subsection 4.5.3 and continue with the discussion of the two–body fragmentation channels (I–IV)

The most prominent signal comes from the anti–diagonal lines at masses 15 and 65 as well as 15 and 63 (Peaks Ia and Ib). While the first breakup isn't a two body breakup as the masses do not add up to 80, the ejection of hydrogens does not alter the momentum sum of the two large fragments appreciably. We interpret these channels as the breakup of 1,4–CHD into CH_3^+ and $C_5H_5^+$or $C_5H_3^+$ respectively.

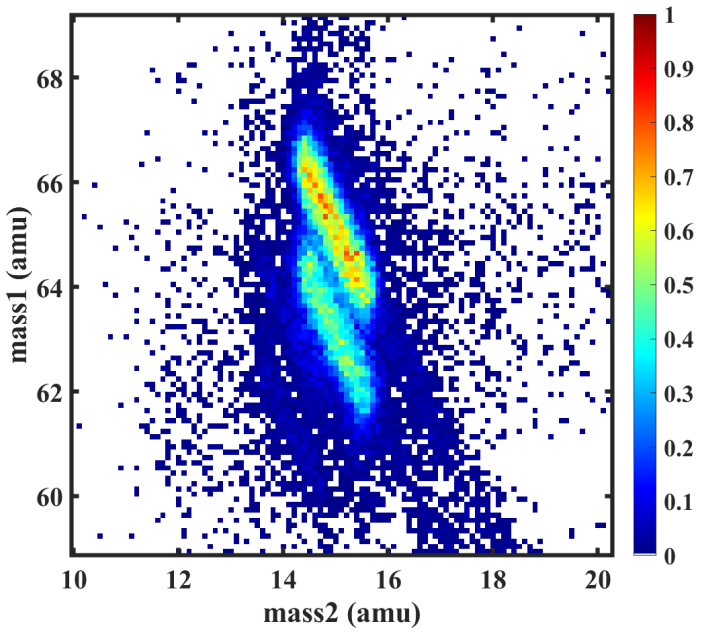

Figure 4.5: Zoomed view of Peak Ia and Ib from Figure 4.4, showing the correlation between fragments $CH_3^+/C_5H_5^+$and $CH_3^+/C_5H_3^+$

At the first glance, the presence of CH_3^+ is surprising as the parent molecule does not have a CH_3 group. In Figure 4.5 we zoom in on this region in order to provide more evidence that the peak indeed is at mass 15 and not 14, which would correspond to CH_2^+. In order to see a dissociation into CH_3^+ there needs to be a proton migration in the dication. Such proton migration

has been observed in similar systems and is relatively common [46, 112, 113]. A time resolved experiment can help identify the time scales for this proton migration. Combining a time resolved experiment with the covariance, similar to the one we perform in chapter 5 would be very interesting in understanding the details of the proton transfer. For example, one could look for the following signature to identify the time scales of the proton transfer: For low delays one could observe a correlation of CH_2^+ and $C_5H_6^+$, which gives rise to a correlation between CH_3^+ and $C_5H_5^+$as the pump–probe delay increases. We leave such a measurement for a future study and continue with the discussion of Figure 4.4.

We see a similar collection of anti–diagonal line around masses 26 and 54 (Peak II) and there are likely three possible disassociation channels with varying number of hydrogens attached to each of the fragments. With certainty we can assign these channels as a breakup of a fragment with 4 carbon atoms and 2 carbon atoms i.e. $C_4H_x^+/C_2H_x^+$. However, the exact number of hydrogen atoms in both of these fragments is difficult to determine as they are overlapping and none of them is dominant. The likeliest candidates for these break–up channels are $C_4H_5^+/C_2H_3^+$, $C_4H_4^+/C_2H_3^+$ and $C_4H_4^+/C_2H_2^+$.

We assign the anti–diagonal Peak III to the break–up channel $C_3H_3^+/C_3H_3^+$i.e. a symmetric break–up of the parent molecule, less two hydrogens, which we do not expect to carry away appreciably momentum. There is however another candidate assignment, which can come from residual halogenated methanes that were used for different experiments[17]. In this light, Peak III might correspond to a correlation between two doubly charged bromine atoms, coming from e.g. a dissociation of CH_2Br_2. However, at the intensities this measurement was taken, it is very unlikely that quadruple or higher ionization takes place. Hence, we feel confident in assigning Peak III to the symmetric break–up channel $C_3H_3^+/C_3H_3^+$.

A similar confusion of fragments is also present for Peak IV. In fact, we refrain from interpreting this peak conclusively but will offer some possibilities. It is located at masses 15 and 39 and they form an anti–diagonal line, indi-

[17]Empirically, samples containing halogens like clorine, bromine and iodine are difficult to pump out.

cating that momentum of these fragments is conserved. Furthermore, note that in Figure 4.4a the angle of the anti–diagonal line is different from 45°, which indicates that one of the fragments is doubly charged, while the other is singly charged[18]. We infer the mass information from the time of flight by ToF $\propto \sqrt{m/q}$ and the time of flight to momentum conversion assumes that the fragment is singly charged and therefore, if the charges of the fragments are different, the angle of the anti–diagonal line is modified by the ratio of the charges. We offer two possibilities for this peak: it could be a fragmentation channel with masses 30/39 or 15/78. In the case of 1,4–CHD the former possibility would correspond to $C_2H_6{}^{++}/C_3H_3{}^{+}$, which is not possible as the number of hydrogens exceed those that are in 1,4–CHD. The measurements are also compatible with $C_2H_5{}^{++}/C_3H_3{}^{+}$, however such a radical rearrangement of hydrogens to form C_2H_5 is extremely unlikely. Furthermore, this would still be a three body break–up, and therefore unlikely to yield a momentum conserving anti–diagonal line.

The other possibility is that this channel corresponds to fragments with masses 15/78, which precludes 1,4–CHD as the parent molecule. This could correspond to triple ionization of a background halogenated methane e.g. CH_3Br and subsequent break–up into $CH_3{}^{+}$ and Br^{++}. This assignment also seems unlikely for two reasons. First, there are two isotopes of bromine with approximately equal natural abundance: ^{79}Br and ^{81}Br. While $^{79}Br^{++}$ would be compatible with the measurements, the absence of $^{81}Br^{++}$ seems to rule out this interpretation. Second, the ratio of partial pressure of any background gas to 1,4–CHD is at least two orders of magnitude lower and thus, it is unlikely to yield such a prominent signal.

4.5.2 N–xy Type Covariance

We can further study momentum resolved fragments in covariance with another fragment i.e. $\mathrm{cov}(N_A, N_{B,\mathbf{p}})$ type covariances. This would give us the momentum resolved distribution of fragment B in covariance with fragment A. In Figure 4.6 we present these covariances for each combination of C_1H_x,

[18]Here we assume as before that we at most triply ionize any sample.

C_2H_x, ..., C_5H_x. Note that there is no symmetry as in previous cases because we break the symmetry explicitly by choosing to resolve one of the fragment's momentum and not the other.

In Figure 4.6 we see a narrow circular feature for each combination of fragments whose number of carbons add up to 6. This can be understood from the point of view of energy conservation. The fragments are born with the certain energy and because we do not orient molecules, all of the directions are equally likely to be present, however the momenta have to add up to the total energy of the fragmentation $E \propto p_x^2 + p_y^2 + p_z^2 \approx const$, which is the equation of a sphere. The two dimensional projection of this sphere is consequently a narrow circular feature.

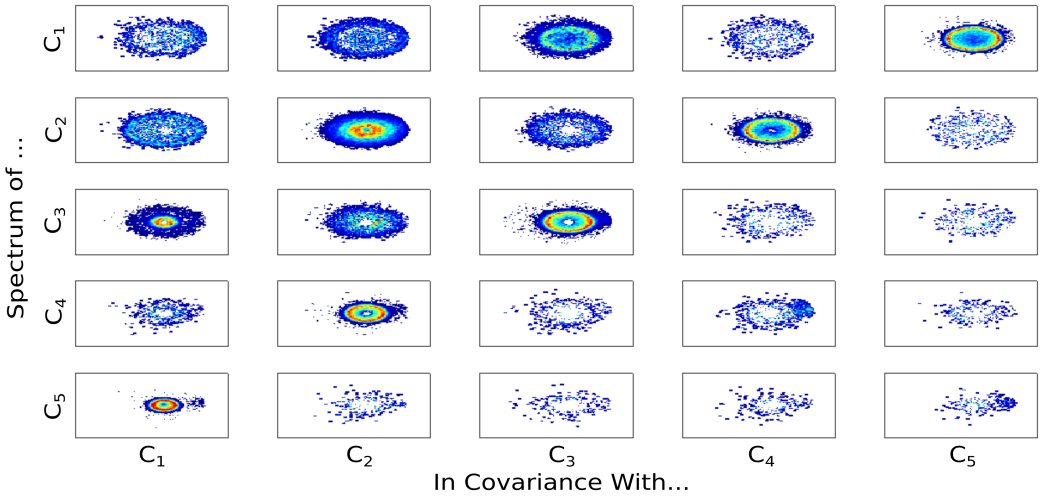

Figure 4.6: N–xy type covariances. The identity of the x,y resolved yield of a fragment is listed on the left and the covariant partner is listed below.

For three–body breakups, the circular feature is not as pronounced as two–body breakups but is thicker, which is a consequence of the fact that the third body carries away some energy. We can see this thicker feature in Figure 4.6 in the spectrum of e.g. C_2H_x in covariance with C_1H_x. Note that in the spectrum of C_3H_x in covariance with C_1H_x we see a smaller thin circle, surrounded by a

larger circular feature. The smaller thinner circle is likely a consequence of a two body break–up i.e. Peak IV. However, as we discussed previously we do not conclusively identify this channel. The larger circular feature comes from a three body disassociation, which we discuss further below. Note that the three body dissociation is more energetic than the two body dissociation and thus, the circular feature has a larger radius.

In the previous section we identified Peak II as a dissociation of 1,4–CHD into C_2H_x and C_4H_x with various numbers of hydrogen atoms. The reader might have been skeptical of this assignment given that there is no prominent anti–diagonal feature for Peak II in Figure 4.4 as dissociation channels with different partitions of hydrogen overlap in time of flight plots. Looking at mixed covariances helps resolve this issue. Since the energy release from the dissociation for these channels with varying number of hydrogens are likely to be very similar, they are all mapped to approximately the same position in the x–y plane. Consequently, we see thin circular features in the spectrum of C_2H_x in covariance with C_4H_x and similarly in the spectrum of C_4H_x in covariance with C_2H_x. This is consistent with the fact that Peak II indeed represents a collection of two body break-ups with different partitions of hydrogens.

Finally, we want to discuss pairs of fragments for which there is vanishing covariance in Figure 4.6. Recall that the upper diagonal of Figure 4.4 was largely empty as the sum of masses of the fragments in this region exceeds the parent mass. Similarly, in Figure 4.6 there is vanishing correlation for plots in the lower diagonal as the sum of the number of carbon atoms for those fragments exceed the the number of carbon atoms in the parent molecule and thus, there cannot be any such dissociation channel.

4.5.3 3-fold N–ToF–ToF Type Covariance

By examining covariances between three fragments, we can isolate triple ionization channels (Peaks V-VIII in Figure 4.4). We resolve two of the fragments in their time of flight and leave the third one unresolved i.e. we study mixed covariances of type $\mathrm{cov}(N_A, N_{B,p_z}, N_{C,p_z})$. By changing the pair of fragments that are time of flight resolved, we can gain a holistic understanding of the 3–body breakup process.

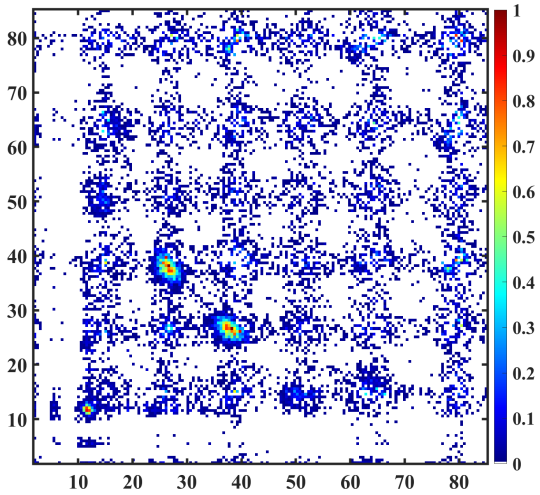

(a) Hidden Partner: $C_1H_x^+$

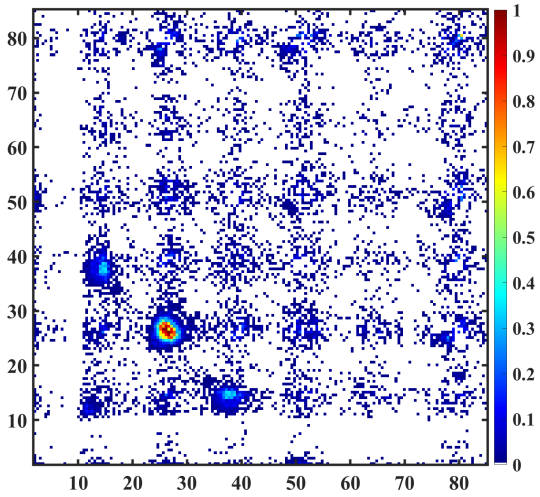

(b) Hidden Partner: $C_2H_x^+$

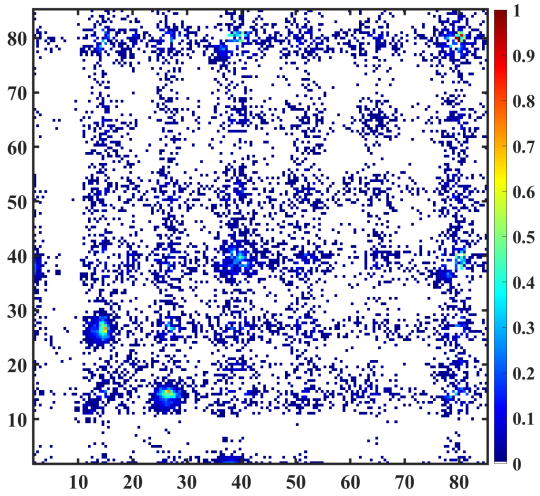

(c) Hidden Partner: $C_3H_x^+$

Figure 4.7: Three–fold mixed covariances in which one of the fragments is not resolved in time of flight. The partner that is not time of flight resolved is shown in the figure captions. Both of the axes in all of the plots depict the mass of the fragments in amu. The labels were removed to fit on single page.

In Figure 4.7 we present these 3–fold covariances. We can see that there are two disassociation channels for the triply ionized parent molecule, namely $C_2H_3^+/C_2H_3^+/C_2H_x^+$channel and $C_1H_2^+/C_2H_3^+/C_3H_2^+$channel. We can locate the symmetric channel in Figure 4.7b as a strong correlation at masses 27 and 27. Along with the third "hidden" partner $C_2H_x^+$ that is not time of flight resolved, this gives rise to the disassociation channel $C_2H_3^+/C_2H_3^+/C_2H_x^+$.

Staying with the same plot, we can see that there is a weaker covariance at masses 14 and 38, which we interpret as $C_1H_2^+$ and $C_3H_2^+$ respectively. This gives rise to the disassociation channel $C_1H_2^+/C_2H_3^+/C_3H_2^+$. Unlike the symmetric disassociation channel into $C_2H_x^+$ ions, we can double check this asymmetric channel by rotating which pair of fragments is time resolved. In Figure 4.7a we plot the 3–body covariance with the C_1H_x as the hidden partner. Here we see that there is a prominent correlation at masses 27 and 38, which bolsters the interpretation of this breakup channel being $C_1H_2^+/C_2H_3^+/C_3H_2^+$. Similarly in 4.7c we see that there is a prominent correlation at masses 14 and 27, again consistent with our assignment of this dissociation channel.

4.6 Conclusion

In this chapter we discussed probabilistic foundations of experimental measurements and introduced the covariance technique. We compared coincidence measurements with covariance measurements and demonstrated that the background subtraction scheme in coincidence experiments is an estimator of the covariance of two fragments. Furthermore, we run Monte–Carlo simulations to estimate the uncertainty of the covariance estimator and discussed the optimal count rates for 2–, 3– and 4–fold covariance experiments.

Lastly, we used the covariance formalism with momentum resolved yields of fragments to study the 2– and 3–body fragmentation channels of 1,4–Cyclohexadine upon strong field ionization. We identified a proton transfer process in the dissociation channels $CH_3^+/C_5H_5^+$and $CH_3^+/C_5H_3^+$and suggested an experimental scheme to identify the time scales associated to the

proton transfer. Furthermore, in Table 4.1 we summarized all of the experimentally observed fragmentation channels and their interpretation as a dissociation channel of 1,4–CHD.

Chapter 5

Long Lasting Electronic Coherences

5.1 Introduction

The interplay between the electronic and nuclear degrees of freedoms has been an important piece in understanding the energy flow in molecules [114–118]. Such interactions play a role in many photo–physical processes such as photo–isomerization [6–8], light harvesting [119, 120] and photo–protection of DNA and RNA bases [9, 12, 121, 122]. The role of electronic coherences (i.e. superposition of electronic states with well defined relative phase relationship) in photo–induced molecular dynamics remains an active research area [13–21]. In what follows we will give a brief overview of this field as well as outline the theoretical background for electronic coherences.

In atomic systems the electronic coherences can last for extended periods of times as there are very few intrinsic mechanisms to disturb the coherence. In atoms the loss of coherence is often related to thermal radiation as well as collisions of atoms with a second body [123–125]. In molecular systems however, the motion of nuclei after photo–excitation complicates the electronic dynamics. Measurements of electronic coherences in molecules have been limited to few femtoseconds [13–20] and recently, they have been demonstrated to last as long as tens of femtoseconds [21].

This ultrafast loss of electronic coherences in molecules can be understood by the interplay between electronic and nuclear degrees of freedom. We can describe the wavefunction Ψ of the molecule in Born–Oppenheimer approximation as:

$$\begin{aligned}\Psi(\boldsymbol{r}, \boldsymbol{R}, t) =& a_1(t)\chi_1(\boldsymbol{R}, t)\psi_1(\boldsymbol{r}; \boldsymbol{R}) \\ &+ a_2(t)\chi_2(\boldsymbol{R}, t)\psi_2(\boldsymbol{r}; \boldsymbol{R}) + \cdots \ , \end{aligned} \tag{5.1}$$

Here ψ_i represents the i^{th} electronic state of the molecule and χ_i represents the nuclear wavefunction on the i^{th} electronic state. As usual, $\boldsymbol{R}$ denotes nuclear coordinates and $\boldsymbol{r}$ denotes electronic coordinates. In general the coefficients a_i depend on time, in order to account for changes in population due to internal conversion or intersystem crossing.

One can generate a superposition state like in Equation 5.1 by multi–photon excitation of a few cycle pulse ($<$10 fs) so that the excitation is restricted to the single subcyle that corresponds to maximum of the envelope function [126–128]. Suppose that we are exciting the molecule to a state via n–photon excitation. The spectrum of the few cycle pulse is very broad and with each photon order the FWHM of the n^{th} order excitation spectrum grows[1] with $\sqrt{n}$. Therefore, the range of states that we can excite with the laser pulses increases with each photon order. Consequently, if there are states that are accessible with $n \pm 1$ photons, one expects these states to be populated as well [127, 128, 131, 132].

Here we focus on the case that the neighboring states are separated by one photon order, which is a natural choice given our photon energy (1.7 eV) and molecular energies involved in the measurement. The initial excitation takes place with at least four photons to reach the first few excited states and ab-

[1]The reader might be surprised that the n^{th} order excitation spectrum *broadens* with each photon order. In the time domain the n^{th} order spectrum is described by the n^{th} power of the field and by the Fourier convolution theorem, the spectrum is the n–repeated convolution of a Gaussian with itself, which results in the $\sqrt{n}$ broadening.

sorbing more than 6 photons readily ionizes the molecule[2]. Hence, we either excite the molecule with 4 and 5 photons or 5 and 6 photons i.e. with one photon order separation in both cases. Of course 4 and 6 photon excitation is also possible, but we think that this is a subdominant excitation process.

Let's take the special case of Equation 5.1 with only two states. Then, the off–diagonal density matrix element that describes the electronic coherence is given by

$$\rho_{12}(\boldsymbol{R}, t) = a_1 \chi_1(\boldsymbol{R}, t) a_2^* \chi_2^*(\boldsymbol{R}, t) \tag{5.2}$$

Looking at Equation 5.2 we can identify the main mechanisms for electronic decoherence in molecules. The first mechanism is the potentiality for the loss of the complex nuclear wavefunction overlap $\chi_1(\boldsymbol{R}, t)\chi_2^*(\boldsymbol{R}, t)$. The other mechanism is that the coefficients a_i can decrease due to population loss mechanisms like conical intersections or inter–system crossings. There are numerous studies on the dominant decoherence mechanism in molecules and which mechanism dominates depends on the details of the molecular system [19, 21, 116, 135–139]. Note that if the potential energy surfaces for electronic states 1 and 2 are approximately parallel, both of these decoherence mechanisms can be suppressed. By definition, there cannot be conical intersections or intersystem crossings for parallel states. Furthermore, the loss of complex overlap function is minimized as the wavefunctions propagate on approximately parallel surfaces.

In order to study electronic coherences, we perform a pulse shape parameter scan, where we parameterize the pulses by the delay and the relative phase between the two pulses. We can describe the pump and probe pulses as follows:

$$E_{\mathrm{pu}}(t) = E_0(t)\cos(\omega_0 t) \qquad E_{\mathrm{pr}}(t) = E_0'(t-\tau)\cos(\omega_0(t-\tau) - \phi_L) \tag{5.3}$$

where, ϕ_L describes the relative phase between the laser pulses, ω_0 the laser

[2]The ionization potential of 3F–Acetone is reported to be 10.67 eV in [133] and 11.00 eV in [134].

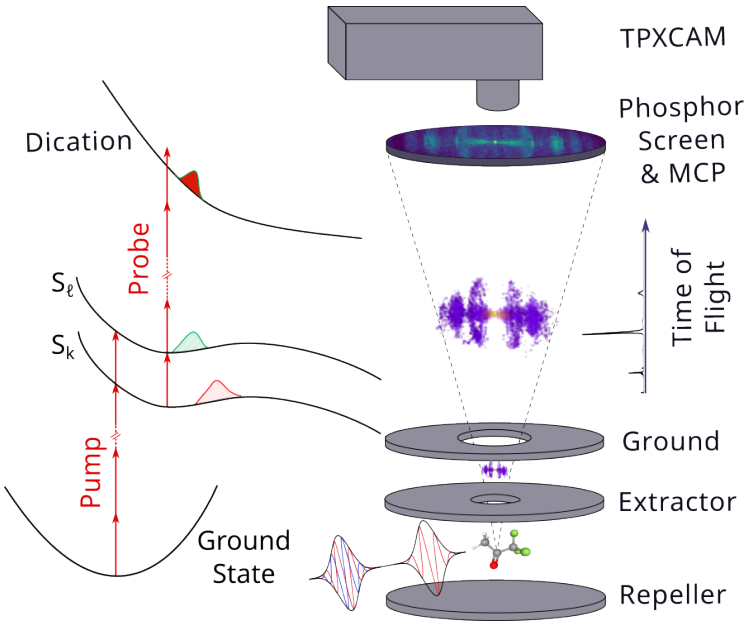

Figure 5.1: Left panel: Potential energy curves and excitation scheme. We excite 3F–Acetone to a pair of high-lying Rydberg states, which are separated by one photon energy. Subsequently the molecule is doubly ionized with a probe pulse. Right Panel: Shaped, phaselocked pump and probe pulses depicted interacting with 3F–Acetone. The resulting velocity distribution of ions are recorded using velocity map imaging apparatus. Created by the author for publication in [126].

frequency, τ the delay between the pump and the probe pulse and E_0 (E_0') are the envelope functions of pump (probe) pulses. In our experiment, we consider n–photon absorption to state 1 and $(n+1)$–photon absorption to state 2 initiated by the pump pulse (see Figure 5.1). Subsequently, the probe pulse doubly ionizes the molecule and we record the momentum resolved yields of resulting fragments as a function of pulse shape.

The recorded dication yield Y as a function of pulse shapes can be described as follows [126, 128]:

$$Y(\boldsymbol{R},t) = |a_1|^2|b_1|^2 + |a_2|^2|b_2|^2 + b_1 b_2^* \rho_{12}(\boldsymbol{R},t) + c.c. \tag{5.4}$$

where b_1 describes the probability amplitude of m–photon ionization to the ground state of the dication from state 1 and b_2 similarly describes that of $(m-1)$–photon ionization from state 2 to the same state. In perturbation theory, one would write for m– or $(m-1)$–photon absorption:

$$b_1 \sim \langle f| \left(\boldsymbol{\mu}\cdot\boldsymbol{E}\right)^m |1\rangle \qquad b_2 \sim \langle f| \left(\boldsymbol{\mu}\cdot\boldsymbol{E}\right)^{(m-1)} |2\rangle \tag{5.5}$$

We wrote $\sim$ instead of equality because the simple perturbation theory cannot capture the strong field dynamics in the laser pulse. Nevertheless, we assume that it captures the main aspects of the excitation. We therefore write:

$$b_1(t) = Q_{1\mathrm{f}}\big(E_{\mathrm{pr}}(t)\big)^m \qquad b_2(t) = Q_{2\mathrm{f}}\big(E_{\mathrm{pr}}(t)\big)^{(m-1)} \tag{5.6}$$

where $Q_{i\,f}$ describes the matrix element for each pair of states. We also note that we do not orient molecules, so these matrix elements are understood to be integrated over all initial orientations. Integrating t over the pulse duration, we arrive at the formula for the yields [128]:

$$\begin{aligned} Y(\boldsymbol{R},\tau,\phi) =& |a_1|^2 \left|Q_{1f}(E_0')^m\right|^2 + |a_2|^2 \left|Q_{2f}(E_0')^{m-1}\right|^2 \\ &+ a_1 a_2^* Q_{1\mathrm{f}} Q_{2\mathrm{f}}^* (E_0')^{(2m-1)} e^{i\phi_L} \rho_{12}(\boldsymbol{R},\tau) + c.c. \end{aligned} \tag{5.7}$$

In this expression, we see how we can study the presence of electronic coherences experimentally. As we vary the relative phase ϕ_L between the pump and the probe pulses, the yield Y modulates over a background that is independent of the presence of coherent electronic states. Note that if the coherent states were separated by K photon orders, then the yield would modulate like $e^{iK\phi_L}$ and consequently K times as we varied ϕ_L from 0 to 2π. The fact that the yield is modulated like $e^{i\phi_L}$ is a direct consequence of the fact that the states were separated by one photon order.

5.2 Experimental Setup

The details of the experimental apparatus was discussed in chapter 2. Here we give important details pertinent to the experiment at hand. In order to probe electronic coherences, we generate two pulses ($\sim$7 fs) with the pulse shaper and perform pump–probe experiment on triply–fluorinated acetone (3F–acetone) as a function of relative phase and delay between the pulses. The molecule 1,1,1-Trifluoroacetone is closely related to acetone, where one of the CH_3 groups in acetone is replaced by a CF_3 group. A ball and stick figure of 3F–acetone is shown in Figure 5.2.

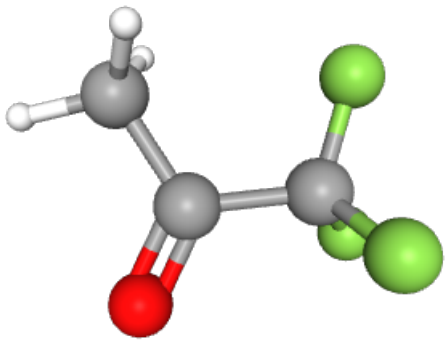

Figure 5.2: Ball and stick figure of 1,1,1-trifluoroacetone. White atoms refer to hydrogens, red atoms to oxygen, gray atoms to carbon and green atoms to fluorine

In order to create two pulses with given delay and relative phase between them we make use of the pulse shaper. Recall from subsection 2.2.3 that we can generate arbitrary pulses by writing a mask on the spectrally resolved pulse (cf. Equation 2.8). In this experiment we make use of a mask of the form:

$$M(\omega) = A_{\text{tot}}\Big(1 + A_{\text{rel}} \exp\left(i\,\tau(\omega - \omega_L) + i\phi_L\right)\Big) \qquad , \tag{5.8}$$

where A_{tot} controls the overall amplitude of both pulses, A_{rel} the relative amplitude, ϕ_L the relative phase and τ the relative delay between the two pulses.

In the time domain this mask creates the following pulses (cf. Equation 5.3):

$$E_{\mathrm{pu}}(t) = E_0(t)\cos(\omega_0 t) \quad E_{\mathrm{pr}}(t) = A_{\mathrm{tot}}A_{\mathrm{rel}}E_0(t-\tau)\cos(\omega_0 t - \tau(\omega_0 - \omega_L) - \phi_L) \tag{5.9}$$

The quantity ω_L is called the locking frequency and the electric field at this frequency interferes constructively for all delays i.e. the relative phase between the two pulses are "locked" at this frequency. In Figure 5.3 we plot a simulated spectrum $E(\omega)$ for a pump–probe signal with locked frequency as well as pump–probe signal in a typical Michelson interferometer, which formally has a locking frequency of 0.

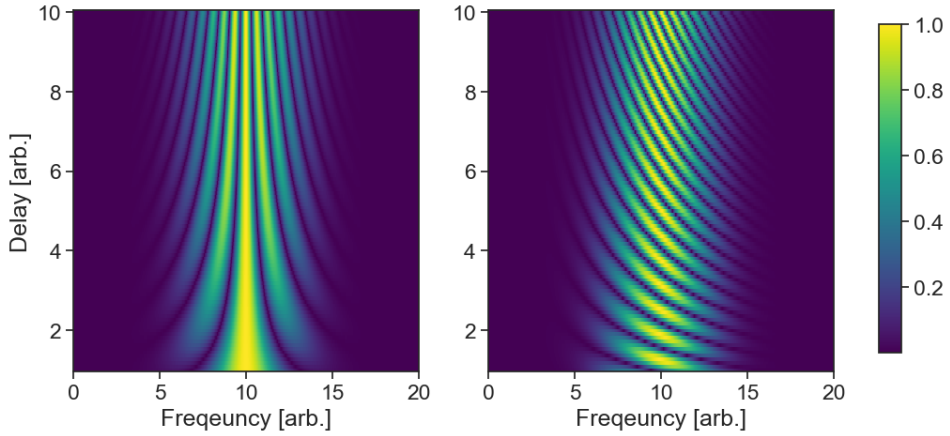

Figure 5.3: Simulated pump–probe spectrum $E(\omega)$ with locked frequency at central frequency (i.e. 10) (left) vs. Michelson interferometer, which formally has a locking frequency at zero (right)

While performing pump–probe scans with the pulse shaper, we have independent control over phase and delay between the two pulses. In a typical Michelson interferometer, one does not have an independent control over the relative phase and the delay (cf. Figure 5.3). To put it in the terminology of pulse shaping, in a Michelson experiment there is no way of controlling ω_L or ϕ_L. By performing pump–probe scans with different locking frequencies and averaging them, we can perform a phase averaged pump–probe experiment.

Since the electronic contributions depend on the relative phase between the pulses, by averaging the relative phase between the pulses we aim to average–out electronic contributions and therefore probe the nuclear dynamics directly as they do not depend on the phase between the two pulses.

As discussed in the previous section, we can identify electronic coherences by performing an experiment where we vary the relative phase between the pulses. However, such a phase sensitive measurement is highly non–trivial. First, such a measurement is easiest to perform when the pump and probe pulses propagate on the exact same beam paths, since optics on different paths can lead to disparate phase accumulation and the exact optical path length might be very difficult to control. The pulse shaper is an indispensable tool to overcome this difficulty. Since the pulse shaper creates both of the pulses collinearly, the optical path lengths of pump and probe pulses are automatically the same.

Another potential problem is the possibility of optical interference of pulses. While two pulses that are separated by a delay longer than the pulse duration cannot interfere, hollow–core fiber broadened spectra often[3] have pre– or post–pulses as self–phase modulation produces structured spectra. When we use the pulse shaper to create the pump and the probe pulses out of this structured spectra, we are creating two pulses that could have pre– or post–pulses. Clearly, if e.g. the main pulse of the pump pulse interferes optically with the pre or post–pulse of the probe pulse so that the effective laser intensity varies as the pulses constructively and destructively interfere, we would get variation in yields of fragments, without probing any dynamics. In section 5.3 below we discuss in detail how we ruled out optical interference.

5.3 Ruling Out Optical Interference

Ruling out optical interference of pump and probe pulses with their potential pre– and post–pulses is of paramount importance. In order to characterize the temporal shape of the pulses we performed pulse shaper assisted CFROGs. In

[3]Self–phase modulation produces spectra with modulations [129, 130]. In the time domain, such modulations result in pre– or post– pulses.

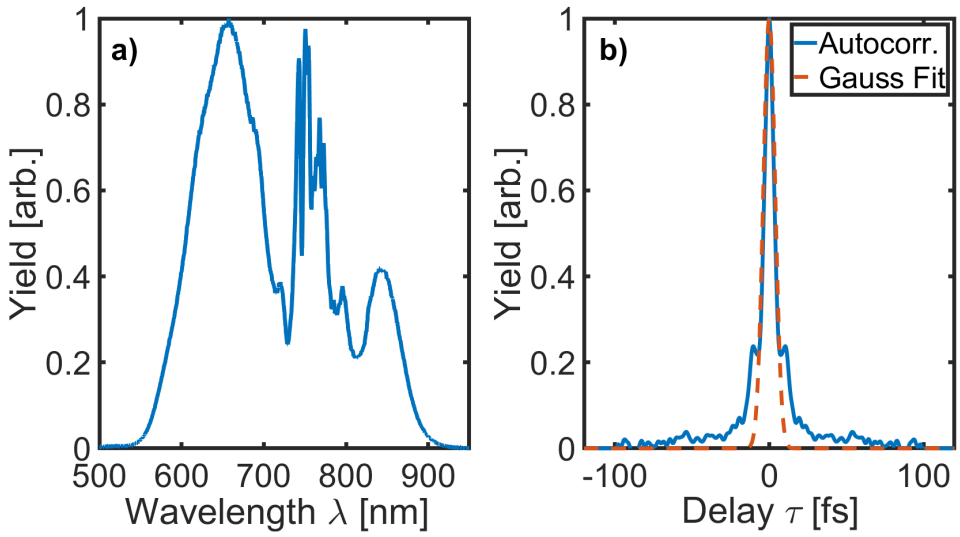

Figure 5.4: Spectrum and reconstructed CFROG. Created by the author for publication in [126].

Figure 5.4 we provide the spectrum out of the hollow–core fiber as well as the reconstructed CFROG. Note that the FWHM duration of the pulse is about 7 fs and there is indeed a pre– or post– pulse at around ±20 fs. Furthermore, there is some intensity extending out to ∼50 fs with diminishing intensity. For this reason, we only performed scans of relative phases with pulses that are separated by more than 85 fs delays, which is well outside of the range that the pre– or post–pulses can optically interfere with the main pulse.

Another evidence for the lack of optical interference of pulses comes from the *dynamics*. If the optical interference was the main driver of the modulations, then all of the fragments would follow the same trend because modulations would be driven by the change in laser intensity as the two pulses interfere constructively and destructively. In Figure 5.5, we extract the yield of two fragments ($CF_3^+$and CF_2^+) from the same dataset. We can see that the co-variant yield of CF_3^+ and the yield of CF_2^+ are out of phase with each other as opposed to in phase, which would be the case if the yields of the fragments

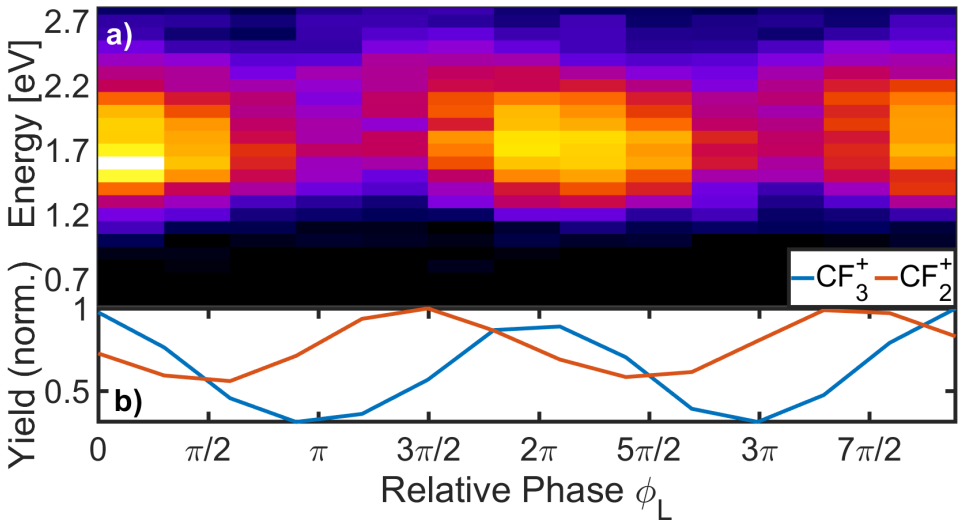

Figure 5.5: (a) Energy resolved yield of CF_3^+ in covariance with CH_3CO^+ as a function of the relative phase (b) Lineout of the above graph for CF_3^+ and yield of CF_2^+ as a function of the relative phase. Created by the author for publication in [126].

were to be modulated by the change in intensity[4]. This indicates that the modulations seen in Figure 5.5 cannot be explained by optical interference. We note that the phase offset between the CF_2^+ and CF_3^+ yields are interesting in of themselves but for the current work we mainly use this offset to rule of optical interference and do not attempt to interpret what the cause of such an offset might be.

5.4 Experimental Results

5.4.1 Vibrational Dynamics

We measure the 3D momenta of fragment ions using the velocity map apparatus discussed in subsection 2.3.2. The ability to study ions in covariance (cf. chapter 4) allows us to gain deeper insights into nuclear dynamics, as it

[4]We expect the intensity dependence of these two fragments to be similar

allows us to focus on particular fragmentation channels. In this study of 3F–acetone, we focus on the disassociation of 3F–Acetone along the CF_3–CH_3CO bond, which is beautifully captured by covariant velocity map imaging. Furthermore, using the pulse shaper (cf. subsection 2.2.3) we study this disassociation channel as a function of the pulse shape, in particular as a function of the pump–probe delay and the relative phase between the two pulses.

With the pump pulse we initially excite the molecule to a pair of high–lying states of the neutral molecule[5]. Subsequently, the probe pulse doubly ionizes the molecule and the resulting molecular fragments are recorded (see Figure 5.1). The recorded kinetic energy release of the fragments varies with their time dependent separation à la Coulombic repulsion[6]. By recording the fragments in covariance, we can both calculate the kinetic energy release from both of the fragments.

In Figure 5.6 we present the pump–probe measurement on 3F–Acetone, which shows the kinetic energy release (KER) from CF_3^+ and CH_3CO^+ in covariance as a function of the pump–probe delay. We estimate that the pump intensity is $230\,\mathrm{TW/cm^2}$ and the probe intensity is $550\,\mathrm{TW/cm^2}$. The locking frequency for this scan was set to $\omega_L = 2.51 \times 10^{15}\,\mathrm{rad/s}$, which corresponds to a central wavelength of 750 nm. As we discussed in detail in chapter 4, measuring these two ions and checking for momentum conservation allows us to uniquely identify the disassociation channel as the bond between CF_3 and CH_3CO.

There are three important features in Figure 5.6(a): (1) the kinetic energy release decreases with increasing pump–probe delay, (2) the KER yield modulates with period $33 \pm 5\,\mathrm{fs}$ (3) an unchanging yield around 5.5 eV. We now discuss each of these features and their interpretation in terms of molecular dynamics.

The monotonic decrease of KER as a function of pump–probe delay is in

[5]This interpretation is explained further by the evidence presented later in this section.

[6]Here we are assuming that the dicationic potential is steep enough (in other words Coulombic enough) so that we can map the kinetic energy release in the dication to the nuclear separation in the neutral. We note however, that even if the dicationic potential deviates slightly from a Coulombic potential, the basic interpretation still holds.

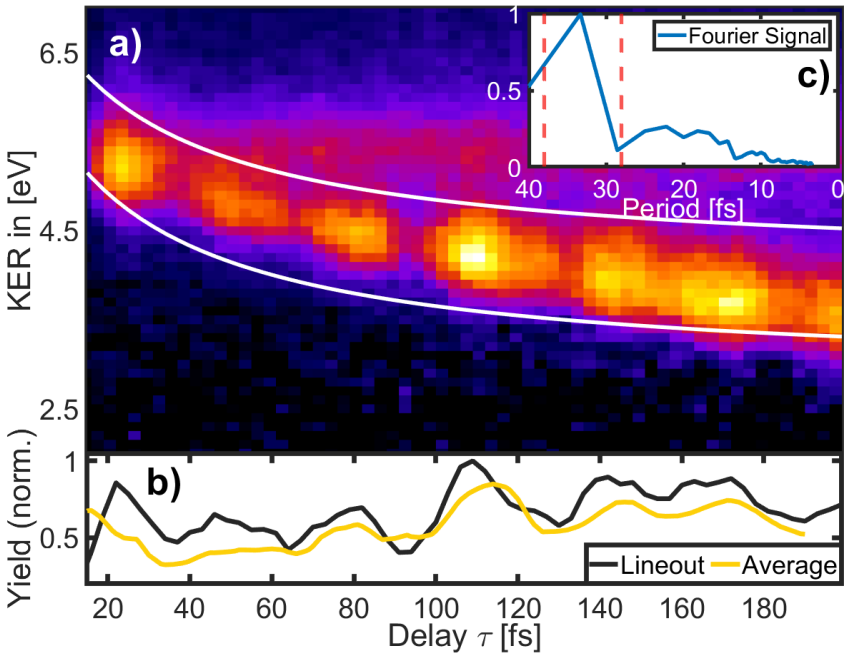

Figure 5.6: In (a) we plot the kinetic energy release from CH_3CO^+ and CH_3CO^+ in covariance as a function of the pump–probe delay at a locking frequency of $\omega_L = 2.51 \times 10^{15}$ rad/s. In (b) we plot the lineout of figure (a) between the white lines, as well as the phase–averaged covariant yield as a function of pump–probe delay. In the inset (c) we plot the Fourier analysis of the phase–averaged signal. Created by the author for publication in [126].

line with the interpretation of disassociation along the CF_3–CH_3CO bond (cf. Figure 5.1). As the distance between CF_3 and CH_3CO increases, the kinetic energy release from double ionization decreases like $1/R$, where R is the distance between these two groups. This is consistent with the interpretation that the KER is dominated by the Coulombic energy between CH_3CO^+ and $CF_3{}^+$ at the time of double ionization (i.e. arrival of probe pulse). In Figure 5.6(a) we indicated this Coulombic trend with white lines[7].

[7]We measure the *difference* between the neutral and the dicationic potentials. Since the neutral potential is relatively flat, the difference is mostly dominated by the Coulombic dication potential.

The second feature is the periodic modulation of the covariance yield with a period of 33 ± 5 fs. We interpret this periodic modulation as coming from nuclear vibrations during disassociation. The period of the modulations matches periods of vibrational modes of the molecule and we expect such nuclear displacements to modulate the kinetic energy release of the dication.

Mode	Assignment [140]	Frequency [cm^{-1}]	Period [fs]
1	C–C–C symmetric stretch	774	43
2	CH_3 symmetric rock	962	35
3	CH_3 antisymmetric rock	1027	32
4	CF_3 symmetric stretch	1131	29
5	**CF_3 antisymmetric stretch**	**1189**	**28**
6	CF_3 antisymmetric stretch	1258	27

Table 5.1: Various vibrational exitations of 3F-Acetone which have a period around 33 ± 5 fs at the Frank-Condon point of the ground state calculated at B3LYP level of theory, as well as one mode above and below the vibrational period of 33 ± 5. Note that the naming convention is ambiguous as the vibrational terminology is insufficient to describe complicated vibrational modes. In Appendix D we display the displacement vectors of each of these modes.

In order to assign a vibrational mode to the modulations we see in Figure 5.6, the author carried out electronic structure calculations for the ground state of the neutral molecule. While the ground state vibrational modes along the disassociation direction are dramatically different than that of the excited state (since the molecule is disassociating), we assume that the calculations provide a reasonable approximation for the directions that are still bound and help us interpret the experimental results[8]. To that end we calculated the vibrational spectrum of 3F–Acetone at the B3LYP/DEF2-SVP level of theory for the ground state of the neural molecule. In Table 5.1 we list the calculated periods of vibrational modes, which have periods within the experimentally

[8]Full computational treatment of the excited state vibrational modes of 3F–Acetone can be carried out by computational chemists, whose expertise is better suited for such calculations.

obtained period of $33 \pm 5\,\mathrm{fs}$. We also listed one mode above and below the experimental range of uncertainty for completeness.

While the experimental measurements are compatible with any one of the vibrational modes within the experimental uncertainty, we can have an educated guess on which one is the likeliest excited mode. The vibrational mode that we seek modulates the disassociative covariant yield in Figure 5.6. Therefore, we don't expect vibrations of the CH_3 group to play a role in the disassociation along the CF_3–CH_3CO bond. Similarly, CF_3 symmetric stretch doesn't affect the bond length between CF_3 and CH_3CO appreciably. Hence, we suspect that the antisymmetric CF_3 stretch (Mode 5) is the likeliest candidate. Here we note that the naming of vibrational modes comes from the most prominent movement for that particular mode and is somewhat ambiguous. This is because the terminology for vibrational modes was developed for a few atoms and therefore, the terminology fails to accurately describe complicated vibrations in molecules with many atoms. In particular, the vibrational mode that we identify involves more than just the antisymmetric vibration of CF_3 group. Furthermore, an adjacent mode is also termed anti–symmetric CF_3 stretch, even though both of the modes are different modes as evidenced by disparate vibrational periods. In Figure 5.7 we depict the displacement vectors for the candidate CF_3 anti–symmetric stretch (Mode 5) and in Appendix D we depict the displacement vector for the all of the modes listen in Table 5.1.

In order to ground this interpretation further, we performed pump–probe measurements at different locking frequencies. In all but one of them, we observe a peak in the Fourier spectrum at $33 \pm 5\,\mathrm{fs}$. Furthermore, we averaged the covariant yield over different locking frequencies. This phase–averaged covariant yield is plotted in Figure 5.6(b), as well as its Fourier spectrum in (c). Since we observe this Fourier peak both in the phase–averaged yield and almost all of the locking frequency scans, we can assign this modulation to molecular vibration.

Finally, we see a constant background in Figure 5.6(a) around 5.5 eV, which is a typical energy scale for double ionization. We believe this constant background to be probe only double ionization. If the probe pulse itself doubly

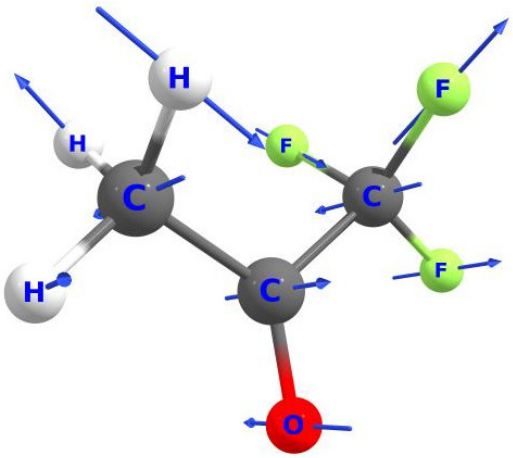

Figure 5.7: Displacement vectors for antisymmetric stretch of CF_3. Note that all of the atoms take part in the vibration and not just the CF_3 group. Created by the author for publication in [126].

ionizes a molecule that wasn't excited by the pump pulse, we expect to see a constant feature in the KER plot. Note also the position of the constant background is at the same KER as the dynamics signal at low pump probe delays. This furthers the interpretation that it is a probe only double ionization. We will disregard this constant background as there's no useful information in this band from the point of view of molecular dynamics.

Since we observe as a disassociation along the CF_3–CH_3CO bond, the initial electronic state of the molecule after the pump–excitation could be a pair of high–lying Rydberg states of the neutral molecule or low–lying states of the cation (cf. Figure 5.1 or Figure 5.8(a)). The phase dependent measurement that we discuss below indicate that it is unlikely to be the low–lying states of the cation, as these electronic states are unlikely to be parallel and exhibit coherences.

5.4.2 Electronic Dynamics

Studying phase–averaged pump–probe measurements shine a light on the vibrational dynamics. In order to gain a holistic understanding of both nuclear and electronic dynamics, we can make use of phase dependent measurements at a fixed delay. To that end we measured the kinetic energy of the CF_3^+ fragment as a function of the relative phase between the pump and the probe pulses. We confirmed using the covariance technique that this channel is indeed the same channel we talked about in the pump–probe measurements. We chose to display the energy resolved yield of the CF_3^+ fragment instead of the covariant kinetic energy release from CF_3^+ and CH_3CO^+ ions, as the statistics for the former was better[9]. This can be understood from the calculations we carried out for the uncertainty of the covariance estimator, as the noise to signal ratio increases going from the raw counts to the covariance (cf. Figure 4.1).

In Figure 5.8 we present the results of phase measurements at a pump–probe delay of 95 fs. Note that we scanned the phase from 0 to 4π in order to benchmark the apparatus since a shift by 2π should yield the same results. As we discussed in section 5.3, we chose such high delays in order to conclusively rule out optical interference of the pump and probe pulses. In Figure 5.8(b) we can see that the kinetic energy of the resulting CF_3^+ ion depends on the phase between the pump and the probe pulses. In order to make this connection explicit, we plotted the center of mass of the distribution at a given phase in black in Figure 5.8(b). This figure therefore, directly shows the coupling between the electronic and nuclear degrees of freedom.

Note also that we see a single modulation of the phase graph within 2π, as opposed to multiple modulations within 2π (see Equation 5.7 and preceding equations). This indicates that the states that contribute to the electronic coherence are separated by one photon energy. Electronic structure calculations at the Frank–Condon point of the ionic molecule indicates that there are no two low–lying states that are separated by one photon energy. This makes us conclude that the initial states that we excite must be the high–lying states of the neutral molecule, as opposed to low–lying states of the molecular ion. As

[9]If the reader is interested in the energy resolved yield of the CF_3^+ ion in covariance with CH_3CO^+ ion, they can see Figure 5.5.

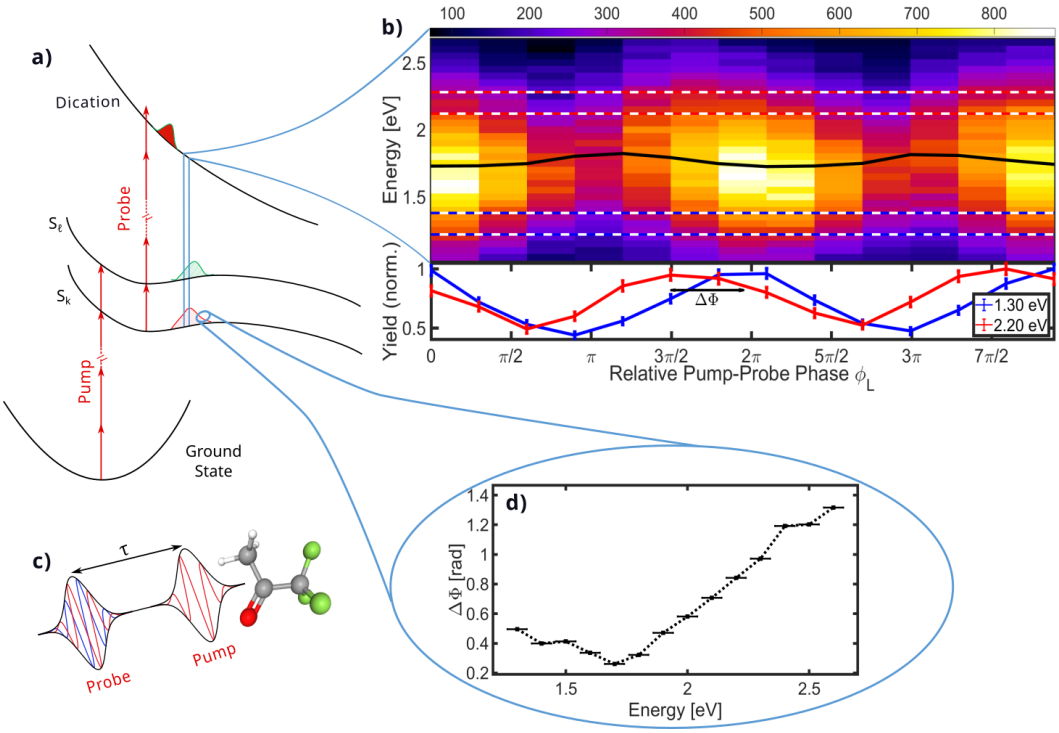

Figure 5.8: (a) Excitation scheme to create and detect coupled electron-nuclear wave packet. (b) CF_3^+ double ionization yield as a function of CF_3^+ energy and pump-probe delay. The lineouts of the red and blue dashed ranges are displayed below with corresponding colors. The center of mass distribution of energies is plotted in black on top of the energy resolved yield. (c) Schematic of shaped, phaselocked pump and probe pulses with different relative phases (d) Phase extracted from fitting lineouts of energy. See Equation 5.10 and text for more information. Created by the author for publication in [126].

we discussed previously, high–lying electronic states of the neutral molecule are likely to be parallel, which allows for coherence to be maintained for longer times.

Lastly, in Figure 5.8(b) we extract lineouts of given energy bands at 1.3 eV and 2.2 eV at the bottom of the plot in order to quantitatively demonstrate the dependence of kinetic energy on the phase. Furthermore, one can fit a

periodic function to the extracted lineouts and extract the phase. Concretely, we fit the following function to each lineout band

$$\text{Lineout} = a \cdot \sin(b\,\phi_L + \Delta\Phi) + c \tag{5.10}$$

where $a, b, c, \Delta\Phi$ are fit coefficients, ϕ_L is the optical phase difference between the two laser pulses. None of the fit coefficients except for $\Delta\Phi$ varied appreciably as a function of the kinetic energy. In Figure 5.8(d) we plot this phase difference $\Delta\Phi$ as a function of the kinetic energy of CF_3^+ ion. We see that there is a non–trivial correlation between the extracted phase and the kinetic energy of the CF_3^+ ion. This non–trivial correlation implies that the intial wavefunction cannot be written as a product of purely electronic and nuclear wavefunctions. In this sense we interpret the modulations in Figure 5.8(b) as direct evidence of entanglement between nuclear and electronic degrees of freedom.

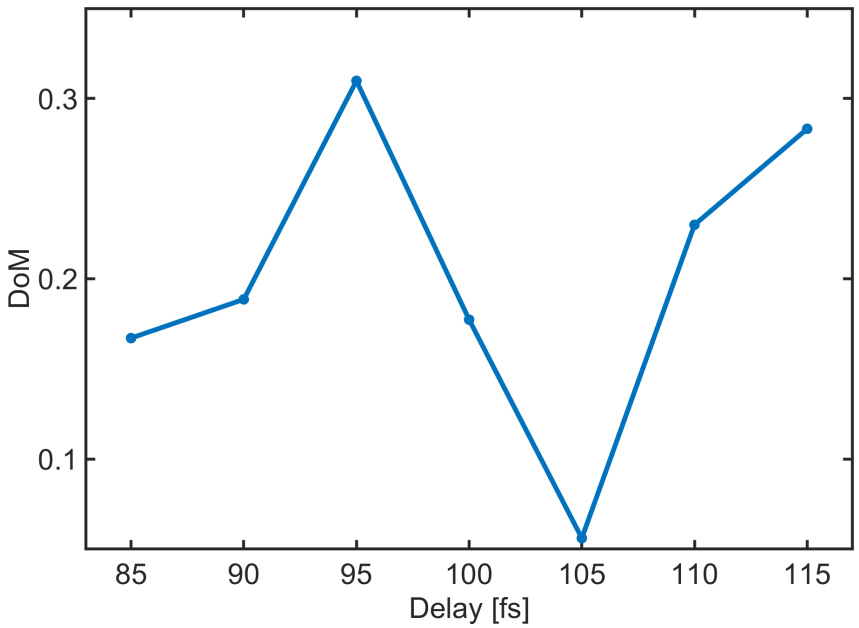

Figure 5.9: Depth of Modulation of phase scans of CF_3^+ yield plotted as a function of pump–probe delay

We carried out such phase measurements at fixed delays for a range of delays from 85 fs to 115 fs. Looking back at Equation 5.7, we can see that the measured dication yield depends on the strength of electronic coherence between the two states. If there is no coherence (i.e. $\rho_{12} = 0$), then we expect to see a constant background, and for non–zero coherence, the yield is modulated by the coherence term. We can thus use the depth of modulation of the phase scans as a proxy for the strength of electronic coherences and study them as a function of the pump–probe delay. We integrate the energy dependent yield to obtain a one–dimensional yield as a function of the relative pump–probe phase.

We define the depth of modulation of a one–dimensional signal S as

$$\text{DoM} = \frac{\max(S) - \min(S)}{\max(S) + \min(S)} \tag{5.11}$$

Note that for non–negative signals such as an integrated yield, the depth of modulation ranges between 0 and 1. In Figure 5.9 we plot the depth of modulation of phase scans as a function of pump–probe delay. We can see that the depth of modulation of the phase scans changes with the pump–probe delay. This indicates that during the dynamics that we described previously, there's a decay and revival of electronic coherences. We think that the main contributor to the change in electronic coherences is the vibrational wave–function overlap term in Equation 5.2. Such revival of electronic coherences due to a change in the nuclear wave–function overlap has been reported previously [14, 125, 135].

5.4.3 TDSE Calculations

We test our interpretation that the phase dependent measurements are a consequence of the interference of wavefunctions on two electronic states by solving time dependent Schrödinger equation for model 1D potentials. To that end, we propagate two wavefunctions on approximately parallel potential energy surfaces using the split operator formalism. Subsequently we calculate the phase difference between these two wavefunctions as a function of the nuclear coordinate $\boldsymbol{R}$.

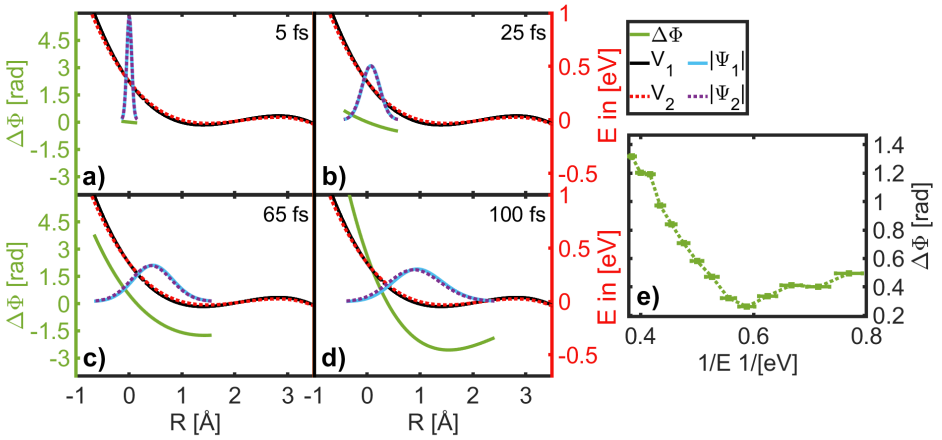

Figure 5.10: (a)–(d): Time evolution of two wave packets on two different, approximately parallel dissociative potentials. In green we plot the R-dependent phase difference between the two wavefunctions at different times. We scaled the wavefunctions for easier viewing. (e) Replot of the experimental phase scan from panel (d) of Figure 5.8. We converted the x-axis into $1/E$ to represent R because of the Coloumb potential relation $E \sim 1/R$. Created by the author for publication in [126].

We chose the two potentials to be dissociative with a small barrier as we expect high–lying Rydberg states to converge towards the ionic state, which is dissociative. We model such a potential by a cubic spline between four points, which roughly correspond to the initial roll down, the minimum, the barrier height and the roll down after the barrier. By varying these points randomly, we made sure that the results we obtain are qualitatively independent of the exact location of these four points. In Figure 5.11 below we plot one of tthe potentials as well as the four points we chose to define the cubic spline.

In Figure 5.10 we present the results of this calculation. We see qualitative agreement between the calculated phase difference in Figure 5.10(d) and the measured phase difference in Figure 5.10(e), which we replotted from Figure 5.8(d). In Figure 5.10(e) we roughly calibrated the kinetic energy of the CF_3^+ fragment into nuclear separation by $R \sim 1/E$ for easier comparison of the measurements with the model.

Our calculations show that the qualitative features in Figure 5.10 are independent of the exact shape of the potential. The wave–packets start with relatively low phase difference displayed in Figure 5.10(a) because they are yet to propagate for sufficient times on their respective potentials. As the wavepackets pick up momentum, they develop a linear phase difference between them (b). Further propagation in different potentials yield a hockey stick shaped feature displayed in (c) and (d). The qualitative comparison between figures (d) and (e) strengthen our interpretation that modulations in Figure 5.8 are indeed a result of coherent interference of two wave–packets propagating on approximately parallel dissociative potential energy sufaces.

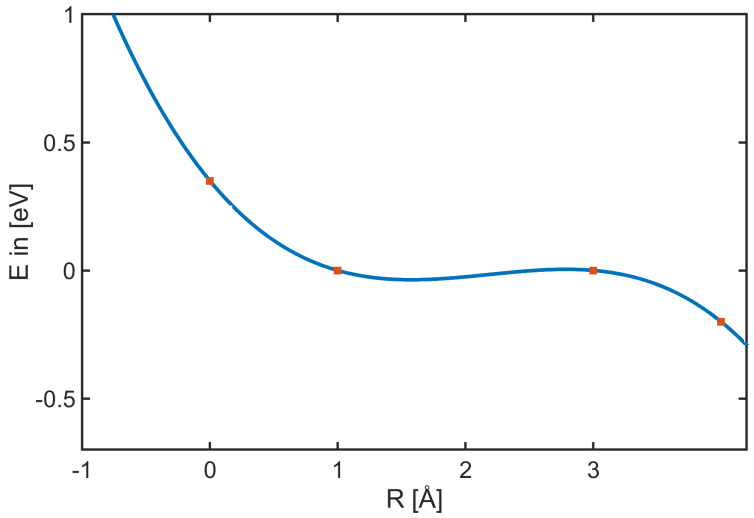

Figure 5.11: Description of four points that were chosen to define the potential energy curves by a cubic spline. The four points approximately correspond to the initial roll down, the minimum, the barrier height and the roll down after the barrier.

Chapter 6

Conclusion and Outlook

6.1 On the Measurement Problem

I remember the first time I watched a lecture on quantum mechanics, in which the instructor made it very clear that all of the ideas and consequences of quantum mechanics are *very weird*. This is in part because we humans do not experience quantum physics and our intuition is attuned to the emergent classical world. It is also because our current understanding of quantum mechanics is, to put it mildly, outrageous. We are taught early on that there is a beautiful equation that describes the quantum world but this equation is accompanied by a twist, namely the collapse of the wavefunction upon measurement of the quantum mechanical system. Hence, there are radically different parts of quantum mechanics, one that describes the time evolution and the other the measurement, whose outcome is described probabilistically by the time evolution. I often found myself thinking about these concepts in the context of the measurements presented in this thesis.

The wavefunction collapse is often described in terms of a superposition of eigenstates collapsing into one eigenstate due to the interaction of the measurement apparatus [141–145]. In a sense the wavefunction collapse is the process through which a quantum mechanical entity "emerges" in the classical world. In the context of the famous double slit experiment, the collapse

happens when the electron hits[1] a position sensitive detector and a "hit" is recorded.

What *is* a measurement? Let's think about this in the context of a photo–ionization measurement. The laser pulse starts a unitary evolution given by the Schrödinger Equation. The molecule is ionized and an electron is created. Has the "collapse" happened? I would argue that the wavefunction of the photo–electron has not yet collapsed as there is nothing other than the laser pulse that can induce this collapse and we readily describe the evolution of the molecule in the laser field as a unitary evolution. If this is the case, then the photo–electron finds itself between two velocity map imaging plates. Do the VMI plates do the "measurement" or does the "measurement" happen when the photo–electron hits the micro–channel plates and causes a shower of electrons? Maybe the "collapse" happens when the shower of electrons cause a "hit" on the phosphor screen. Because of the measurement problem, we are left with the "sorting" of measurement devices (like the laser pulse, VMI plates, MCPs, phosphor screen etc.) into the buckets of "driving unitary evolution" or "projection onto a definite outcome" i.e. "collapse–inducing".

From the perspective of gathering information about a molecular system, it could be totally irrelevant when the collapse exactly happens or whether it happens at all. All that matters is that we can faithfully record the probability distribution of photo–electrons and that we have a systematic way (e.g. Schrödinger Equation) to predict these probabilities. This line of thinking highlights the modeling nature of physics. The Schrödinger Equation is the framework through which we *model* quantum mechanical systems. Especially for complicated quantum mechanical systems like molecules this modeling nature becomes even more apparent. The Basis Set Exchange website[2], which collects various basis sets used in quantum chemistry calculations, has over 700 possible basis sets. There are likely at least as many numerical methods that one can choose to run the actual calculation. The reason for such a

[1] When we use phrases like "an electron hits the detector" we are invariably invoking classical intuition to describe what happens. Perhaps a more accurate but verbose phrasing could be "when the wavefunction of the electron has sufficient overlap with the wavefunction of the of the detector to induce an initial shower of electrons".

[2] `https://www.basissetexchange.org`

large number of number of numerical methods is that some of them are better equipped at modeling certain chemically relevant properties and others are better at other chemically relevant properties.

By taking the modeling perspective, physicists and chemists can successfully sidestep the measurement problem and leave the discussion of the measurement problem to the philosophical community. Yet the real connection between the theoretical calculations and experimental results goes straight through the measurement problem. In my experience, the measurement problem is often swept under the rug, even though it *is*, in some sense, the basis of any experimental measurement. This avoidance is perhaps because the measurement problem is an uncomfortable reality that we learned to forget.

6.2 Conclusion

In this thesis we proposed an experimental scheme to measure the 3D momentum of electrons and combined AOM pulse shaping with the covariance technique in order to study photo–induced dynamics of 3F–Acetone. In chapter 2 we discussed the entire experimental apparatus from the first light generation to spectral broadening in hollow–core fiber to shaping and compression of laser pulses with the AOM pulse shaper. We further discussed the vacuum apparatus, as well as the modifications we made to the vacuum system in order to streamline the sample preparation and to have easier control over the partial pressure of the sample in the vacuum chamber. Lastly, we discussed the velocity map imaging detector and the timepix camera. The timepix camera combined with the AOM pulse shaper is one of the two main pillars of this thesis.

In chapter 3 we proposed a new technique to measure the 3D momentum of photo–electrons. We gave a detailed description of the experimental set–up, where we combined the timepix camera with a constant fraction discriminator in order to timestamp time of flight spread of electrons with 260 ps time resolution. We discussed the strengths and shortcomings of this method and compared it to previously existing methods.

We laid the probabilistic foundations of experimental measurements in chapter 4. Subsequently, we introduced the covariance technique, which is the second pillar of this thesis. We simulated the noise to signal ratio of the covariance estimator in two scenarios; the ideal case and the worst case scenario. In the former case, we compared the simulations to theoretical results. In the worst case scenario, we discussed the uncertainty of the covariance estimator and identified optimal experimental regimes to perform covariance experiments. We then compared the covariance technique to a previously existing background subtraction scheme used in coincidence measurements. Finally, we demonstrated the covariance technique in the example of multi–photon ionization of 1,4–Cyclohexadiene and discussed its various fragmentation channels.

In chapter 5 we combined pulse shape spectroscopy with covariance technique in order to study electronic and nuclear dynamics in 1,1,1-Trifluoroacetone. We gave a brief overview of electronic coherences and discussed how we can identify nuclear and electronic degrees of freedom using the pulse shaper. We then discussed the results of the pump–probe measurements. These measurements indicated a dissociation along the CF_3–CH_3CO bond, as well as a vibrational excitation of the molecule. We used the covariance velocity map imaging technique to analyze fragment ions CF_3^+ and CH_3CO^+ in covariance. We subsequently uncovered the entanglement of electronic and nuclear degrees of freedom and reported on the persistence of electronic coherences even though the molecule underwent large amplitude nuclear motion.

6.3 Scientific Outlook

I want to discuss my scientific outlook on three different time scales: short–, mid– and long–term. In the short–term, the measurement that were presented in the last chapter can be extended to an analogous family of molecules. On the mid–term scientific outlook, I see the arrival of "big data" in ultrafast physics as the exciting new direction that can transform the way we analyze and understand ultrafast experiments. On the long–term, I speculate about how some of the techniques presented in this thesis could be put to practical use in various industries.

In chapter 5 we studied the dissociation of 3F–Acetone along the CF_3–CH_3CO bond and interrogated the relationship between the nuclear and electronic degrees of freedom. This study can be extended by analogous molecular systems with different halogenations. For example, instead of fluorine atoms, one can use chlorine atoms and compare and contrast the two cases. While the ionic state of 3F–Acetone dissociates within ∼100 fs, 3Cl–Acetone has a much longer dissociation horizon [146, 147] and could be an interesting test case for longer electronic coherences during possible dissociative dynamics.

In preliminary pulse shape experiments on 3Cl–Acetone, we noticed that the CCl_3^+does not stay intact, unlike CF_3^+. This is evident in the time of flight mass spectrum of 3Cl–Acetone in Figure 6.1: The CCl_2^+ signal is much more prominent compared to CCl_3^+signal, which is vanishingly small. This could make it more difficult to study and interpret the same dissociation channel as this channel likely leads to three–body dissociation at comparable laser intensities.

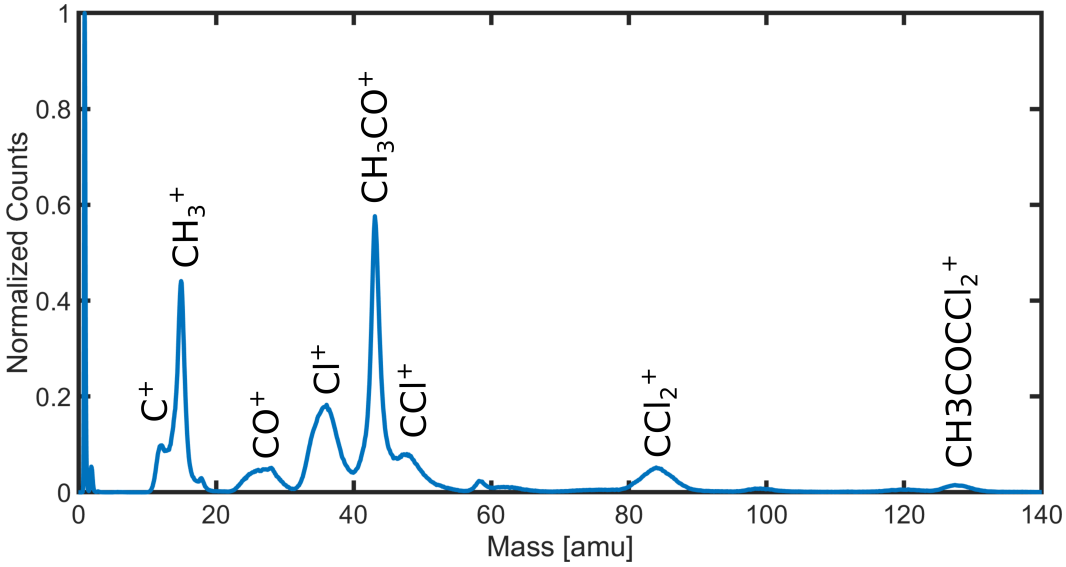

Figure 6.1: Mass Spectrum of 3Cl–Acetone due to strong field ionization. Prominent fragments are identified and labeled

We also carried out preliminary pump probe scans at different locking fre-

quencies as well as phase scans at fixed pump–probe delays for this molecule. Unlike the case in 3F–Acetone, modulations in the yields of fragments for 3Cl–Acetone depend on the locking frequency, indicating that the cause of the modulations are likely from electronic degrees of freedom and not vibrational. While a covariant treatment is needed to fully interpret and understand these measurements, the author is excited for the results of a future study of 3Cl–Acetone molecule and its comparison to the 3F–Acetone case. Already in the preliminary stages of these measurements, there seems to be clear differences in dynamics.

*
* *

As the granularity of the information we gather increases, so does the amount of data collected in ultrafast experiments. The increase in amount of data collected poses both a technical challenge and unparalleled scientific oppurtunities. The storage, access and development of algorithms for large datasets is a scientific discipline of its own and requires specialized training in these areas. Recently, in part in recognition of this reality, ideas about a third type of physicist that goes beyond the experimentalist and theorist paradigm has emerged, namely the idea of "data physicist" [148]. With the increasing use of higher repetition rate lasers ($\sim$100 kHz) [108] the author believes that ultrafast community is at the precipice of having the need for such specialized expertise in data science that necessitates tight collaborations across different scientific disciplines.

The arrival of "big data" in ultrafast science also provides many scientific opportunities, especially in light of pulse shape spectroscopy. In this thesis we presented results of pulse shape spectroscopy, where we *chose* to shape the pulses according to pump–probe paradigm, even though we have arbitrary control on the shape of pulses. Of course, the choice of the pump–probe paradigm helps the interpretation of the data immensely, whereas it is not at all obvious how to interpret a strong field ionization experiment as a function of the *entire* pulse shape and not just as a function of one or two parameters, like pump–probe delay or relative phase between the two pulses.

For example, the author can imagine an extensive pulse shape experiment,

where the spectrum of the laser is recorded simultaneously during the measurement. On the theory side, one could take these various spectra and simulate the ensuing dynamics *as is* i.e. outside of the pump–probe paradigm. Such a measurement would test both the theory and the experiment at a fine level. In interpreting these measurements or coming up with appropriate computational methods machine learning methods might play a big role. The author is excited about what such pulse shape experiments can uncover.

*
* *

On the longest term, one can imagine that pulse shape spectroscopy is used to identify molecules by their quantum dynamics. In the literature, there are already theoretical and experimental ideas that point towards feasibility of this proposition [149–151] . In pharmaceutical and chemical industries, identifying the products created through a chemical process plays a vital role. In these fields, electron impact mass spectroscopy is one of the techniques to identify substances by their cracking patterns, which is often used alongside chromatography techniques like gas chromatography. The author can imagine that pulse shape spectroscopy can be a competitor to electron impact mass spectroscopy as a scan of pulse shapes is likely to capture details of molecular structure, that is otherwise difficult to determine with electron impact mass spectroscopy. Already the extension of one–dimensional mass spectrum to two– and higher–dimensional analogues using covariance measurements outlined in chapter 4 could prove useful in these applications.

Appendix A

Hollow Core Fiber Degrees of Freedom

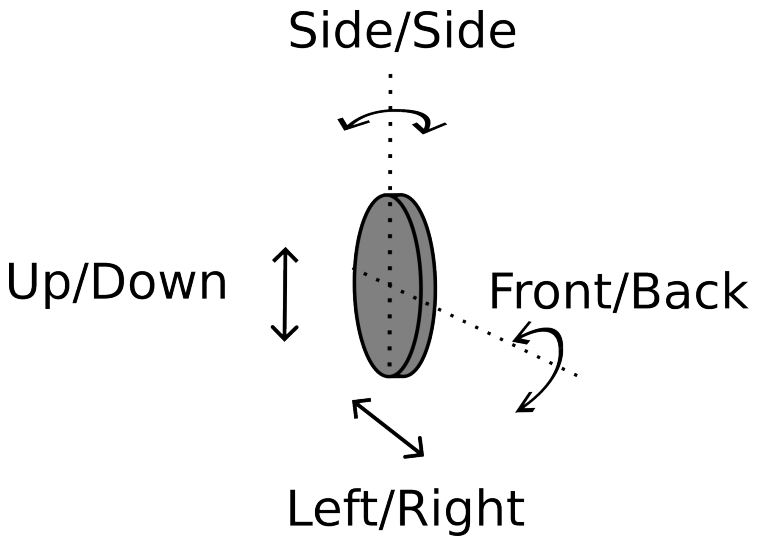

Figure A.1: Definitions of different degrees of freedom of the mount that holds the hollow–core fiber. The degree of freedom along the fiber that controls the tension of the fiber is not depicted.

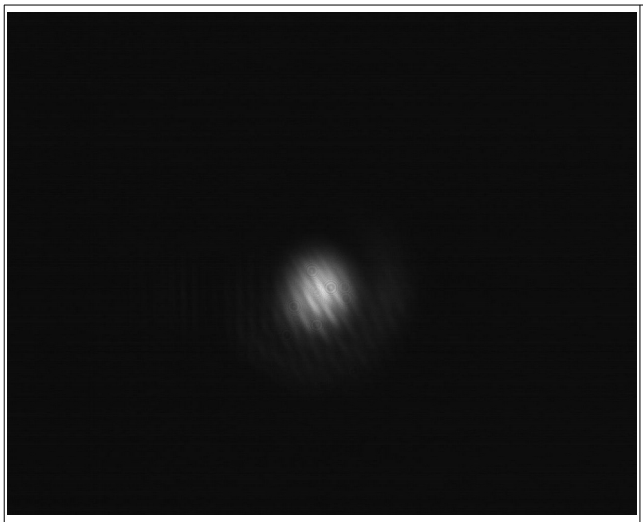	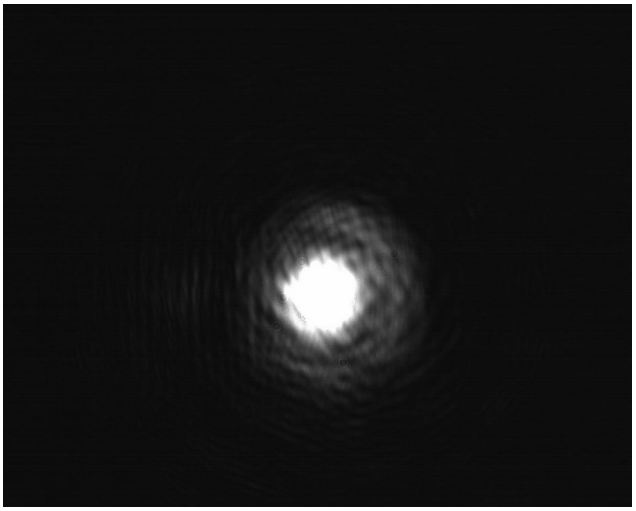
Exit perfect	Exit perfect saturated
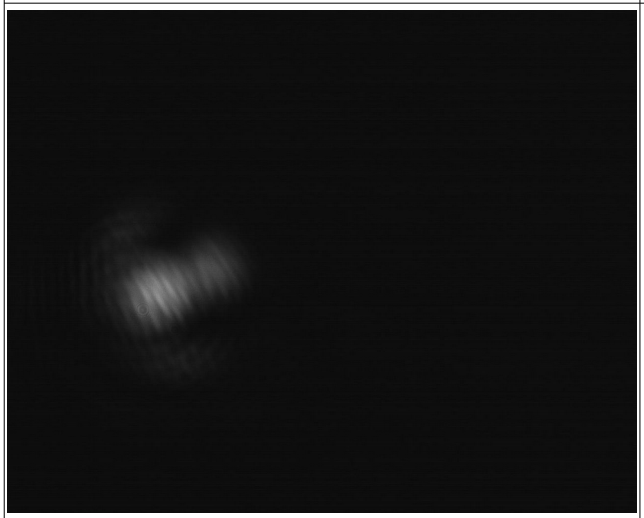	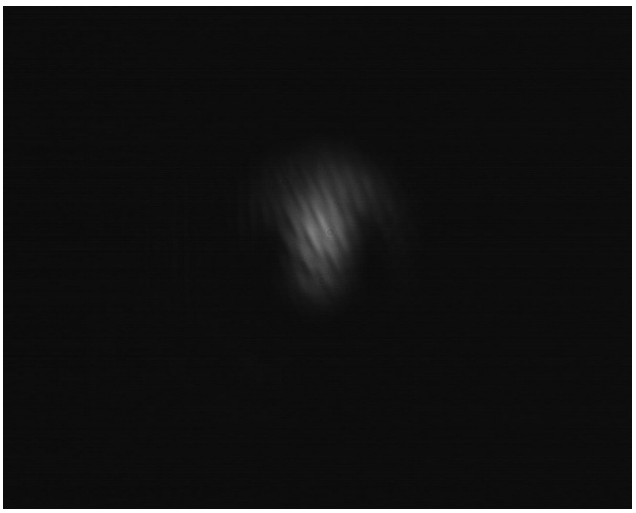
Exit Left-Right Knob	Exit Up-Down Knob
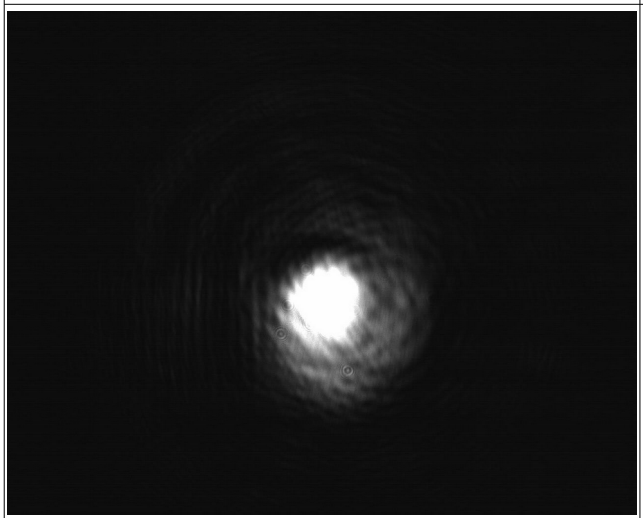	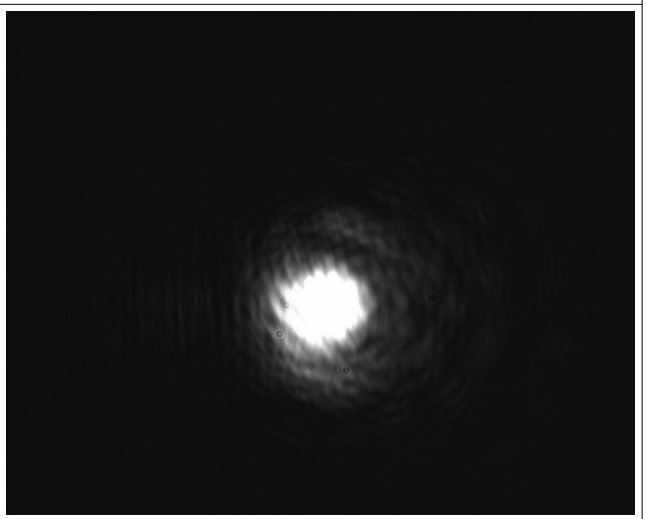
Exit Side-Side Knob (image saturated)	Exit Front-Back Knob (image saturated)

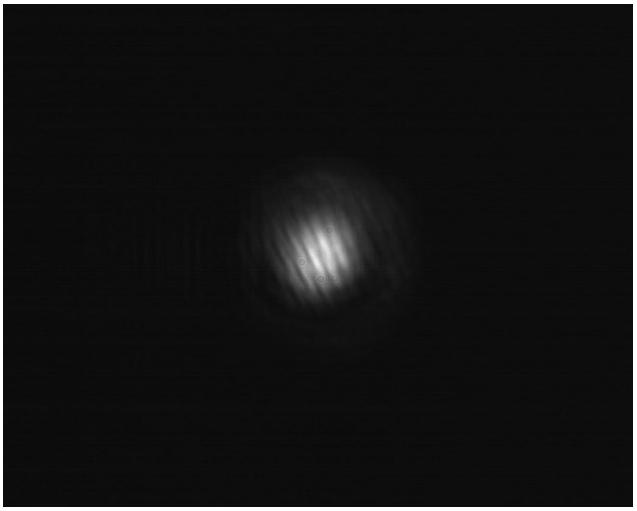	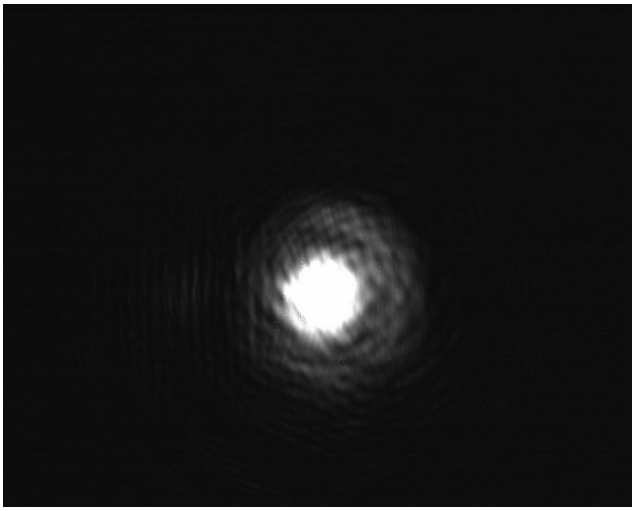
Front Perfect	Exit Perfect saturated
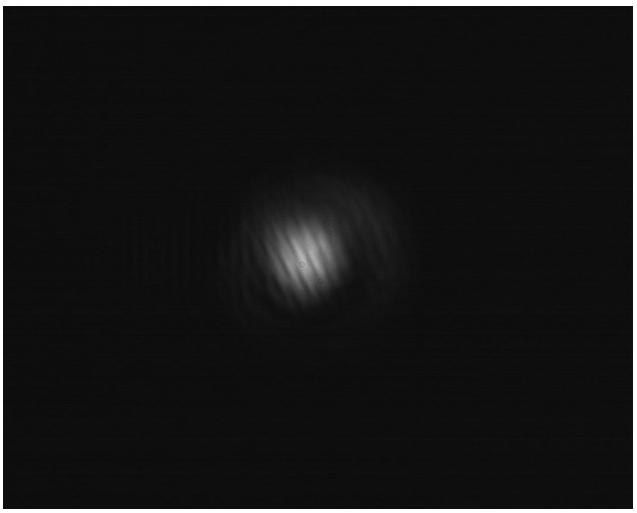	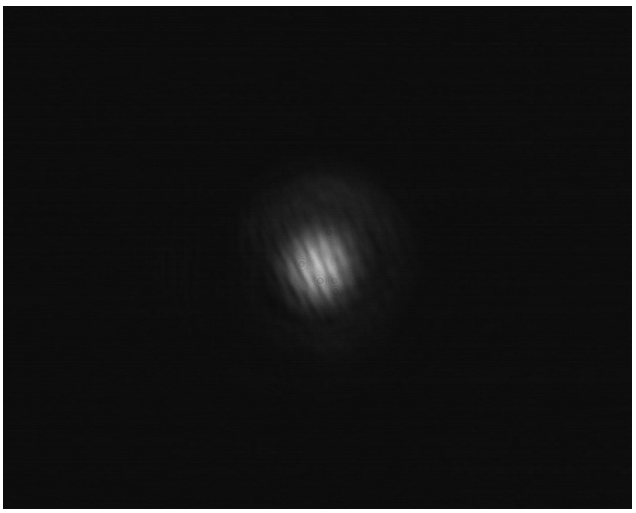
Front Left-Right Knob	Front Up-Down Knob
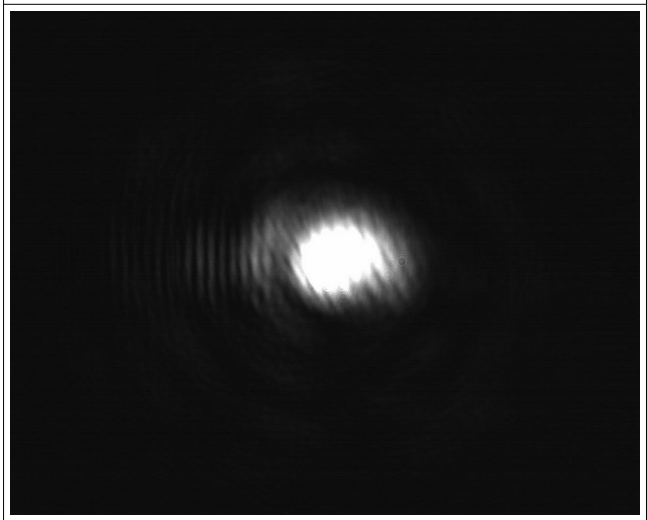	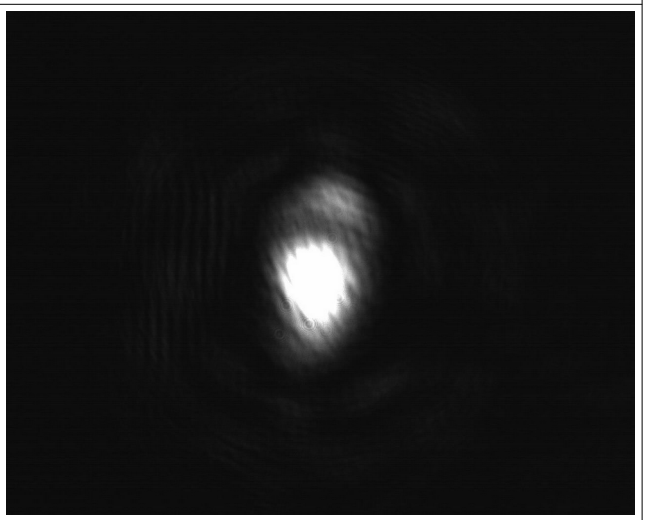
Front Side-Side Knob (image saturated)	Front Front-Back Knob (image saturated)

Appendix B

Recovery from Diffusion Pump Oil Contamination

In this appendix we detail the recovery from the diffusion pump failure as well as the lessons we learned that could be of interest to any experimentalist who uses diffusion pumps. After the initial clean–up of the diffusion pump in the sample chamber, we checked the performance of the VMI apparatus and concluded that it was operational, albeit with compromised sensitivity (see Figure B.1), which we have determined with the sensitivity map technique [152]. In this technique we make use of the fact that each electron hit should lead to the same signal on the phosphor screen. Of course in reality this is not the case due to spatially varying sensitivity of the detector. By diving the total brightness (ToT) of each pixel by the total number of hits recorded by each pixel we can estimate the sensitivity of that region of the detector. The sensitivity map is independent of the distribution of the particles incident on the detector [152].

We installed the RGA back onto the science chamber and pumped out both chambers. The initial RGA readings (see Figure B.2) showed the usual gasses like hydrogen, water vapor and air as well as regularly spaced hydrocarbons up to 200 atomic mass units with partial pressures less than 2×10^{-9} Torr. These hydrocarbons were clear indication of diffusion pump oil contamination but their low vapor pressure reinforced our (false in hindsight) belief that the contamination in the science chamber was minimal. We baked the chamber

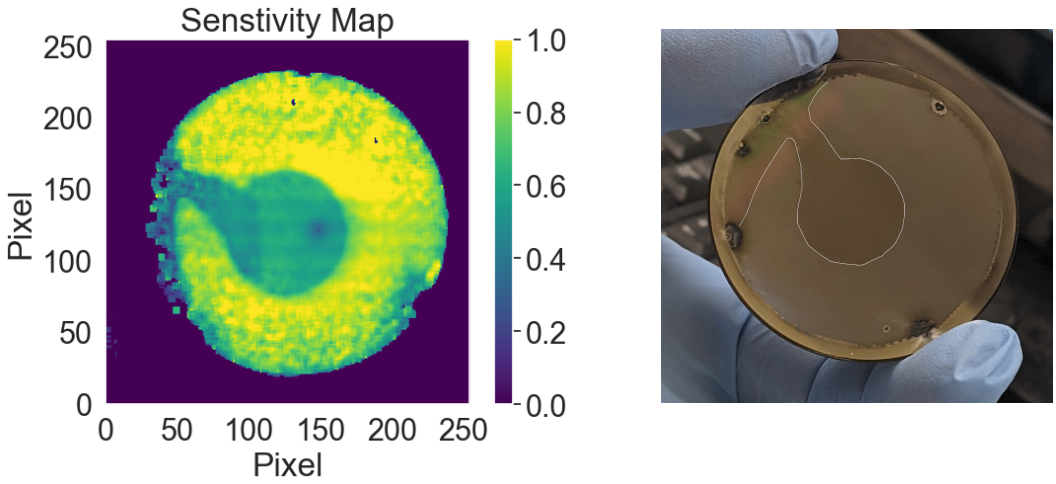

Figure B.1: Recovered sensitivity map (left) and actual damage on the MCP (right). The damage on the right image is marked with a white line for clarity.

again and saw the rise of water vapor as well as hydrocarbons during the bake and the subsequent fall after pumping on these outgassing substances.

However, during the bake we noticed that the sensitivity of RGA was being lost and there was a growing mismatch between the total pressure read by the Bayard–Alpert gauge and the mass spectrum. The mystery of incorrect RGA readings were partially explained by the type of diffusion pump oil used, which was silicone based. Upon being hit by high energy electrons created by Bayard–Alpert gauges silicone based pump oils react and create silica on the filament and more importantly on the collector, thereby reducing the amount of current measured [153]. Since these gauges infer the pressure in the chamber by measuring the amount of current [42], the coating of the collector with silica makes it look like the pressure is lower than it actually is. This is very important to keep in mind when working with diffusion pumps as small amounts of contamination might go undetected and make the vacuum in the chamber look better than it actually is.

In order perform a deep cleaning the chamber, we have disassembled every

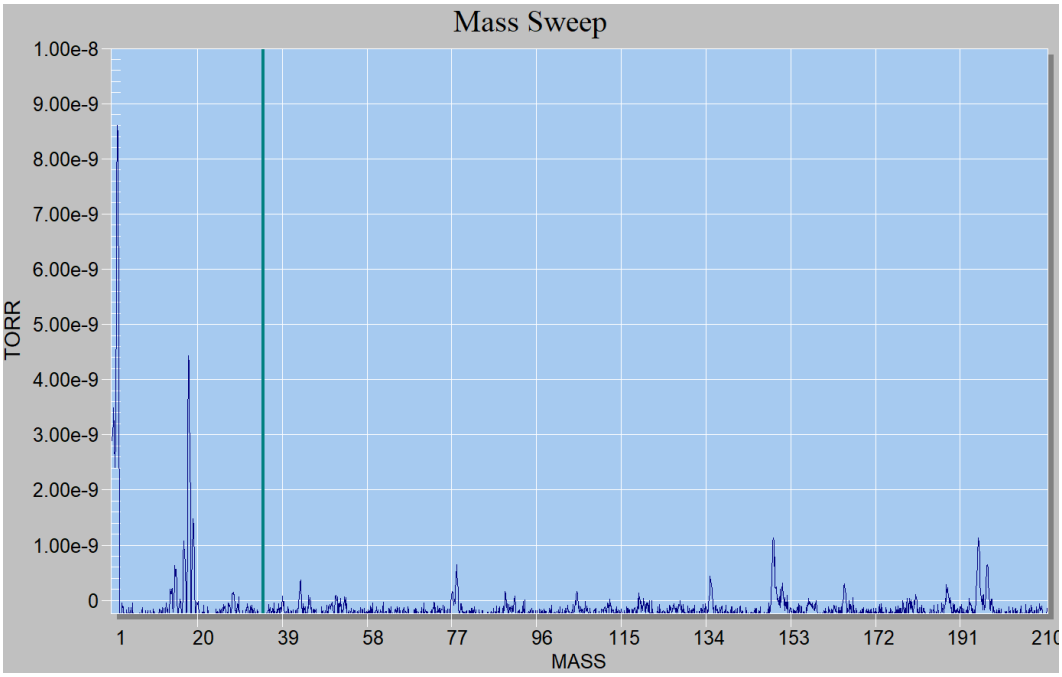

Figure B.2: Initial RGA reading

part of the chamber. Each piece was cleaned twice with a special soap[1] designed for (among other applications) vacuum equipment. Importantly for us, it is advertised to leave no residue upon rinsing with water unlike for example common dish soap. This kind of residue would be detrimental to creating an ultra high vacuum system that we aim for. After cleaning with soap and water, each piece was rinsed with acetone to get rid of any further residue. Subsequently, each piece was dried with a heat gun so that we can be certain that no water or acetone is left on the vacuum equipment. Delicate parts were cleaned in an ultrasonic cleaner and rinsed with acetone. Lastly, the turbo pump on the science chamber was sent to the manufacturer for disassembly and thorough cleaning.

In Figure B.3 we plot the total pressure in the vacuum chamber during the

[1]I thank Eric Jones for pointing out the existence of such cleaning materials and James Ekşi for pointing me to the right brand.

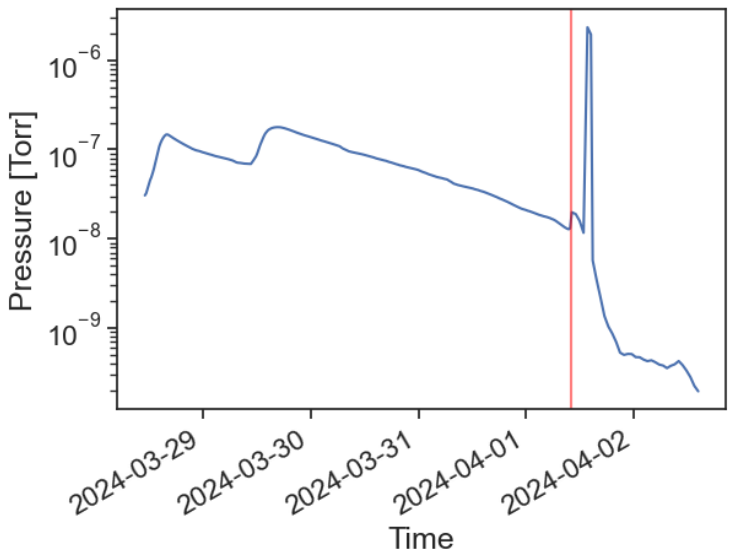

Figure B.3: Total pressure in the chamber over time. The red line indicates degassing of the RGA and subsequent cooling of the chamber.

final bake. We can see that the pressure rises when we actively increase the temperature and that the pressure decreases while the temperature is kept constant, consistent with the degassing of the vacuum walls. We took care in not increasing the total pressure too high, as there was still remnants of diffusion pump oil in the chamber. After degassing and subsequent cooling, the chamber reached a final pressure of 1×10^{-9} Torr. We note that the pressure can further be decreased by a subsequent bake, as water vapor is the dominating background gas in the chamber.

Appendix C

Derivation of the Covariance Formula

In what follows, we want to show that the tree–fold covariance formula, which is defined as

$$\mathrm{cov}(N_A, N_B, N_C) := \left\langle (N_A - \overline{N}_A)(N_B - \overline{N}_B)(N_C - \overline{N}_C) \right\rangle \tag{C.1}$$

reproduces the triple ionization rate λ_{ABC} i.e. we want to show that

$$\mathrm{cov}(N_A, N_B, N_C) = \lambda_{ABC} \tag{C.2}$$

We define $\Delta X := X - \overline{X}$ to be the de–meaned random variable for notational convenience. Expanding the first term on the right hand side of Equation C.1 we get:

$$\mathrm{cov}(N_A, N_B, N_C) = \langle N_A \, \Delta N_B \, \Delta N_C \rangle - \overline{N}_A \, \mathrm{cov}(N_B, N_C) \tag{C.3}$$

For the 2–body covariances $\mathrm{cov}(N_B, N_C)$ we have:

$$\mathrm{cov}(N_B, N_c) = \mathrm{cov}(N_{BC}, N_{BC}) + \mathrm{cov}(N_{ABC}, N_{ABC}) = \overline{N}_{BC} + \overline{N}_{ABC} \tag{C.4}$$

The first term in Equation C.3 requires some care. We cannot manipulate the expectation value further because N_A, ΔN_B and ΔN_C terms are not statistically independent as they both depend on the triple ionization channel. In

what follows, we remove the statistically dependent pieces systematically. To that end, we remove the N_{ABC} term, which we have to treat separately. For all of the random variables we write $\breve{N}_A := N_A - N_{ABC}$ in order to separate the triple–ionization channel.

$$\langle N_A\,\Delta N_B\,\Delta N_C\rangle = \left\langle \breve{N}_A\,\Delta N_B\,\Delta N_C \right\rangle + \langle N_{ABC}\,\Delta N_B\,\Delta N_C\rangle \tag{C.5}$$

We claim that the first term in Equation C.5 is given by:

$$\left\langle \breve{N}_A\,\Delta N_B\,\Delta N_C \right\rangle = (\overline{N}_A - \overline{N}_{ABC})\,\mathrm{cov}(N_B, N_C) \tag{C.6}$$

Writing $\breve{N}_A = N_{A0} + N_{AB} + N_{AC}$, we see that there are two non–trivial terms, namely the double ionization channels. Since the single ionization channel N_{A0} is independent of both ΔN_B and ΔN_C, we can take it out of the expectation value. We calculate one of the non–trivial terms, as the other one is analogous. We again use the separating trick we employed above and write $\Delta\widetilde{N}_B := \Delta N_B - \Delta N_{AB}$.

$$\langle N_{AB}\,\Delta N_B\,\Delta N_C\rangle = \left\langle N_{AB}\big(\Delta N_{AB} + \Delta\widetilde{N}_B\big)\Delta N_C \right\rangle \tag{C.7}$$

Note that both ΔN_{AB} and N_{AB} are independent of ΔN_C, so we can split the expectation value for the first term. Similarly for the second term, N_{AB} is independent of $\Delta\widetilde{N}_B$ and ΔN_C. Using the fact that $\langle \Delta N_C\rangle = 0$, we get:

$$\langle N_{AB}\,\Delta N_B\,\Delta N_C\rangle = \langle N_{AB}\,\Delta N_{AB}\rangle\ \langle \Delta N_C\rangle + \langle NAB\rangle\ \left\langle \Delta\widetilde{N}_B \Delta N_C \right\rangle \tag{C.8}$$

$$= \overline{N}_{AB}\,\mathrm{cov}(\widetilde{N}_B, N_C) = \overline{N}_{AB}\,\mathrm{cov}(N_B, N_C) \tag{C.9}$$

where the last equation holds because N_{AB} is independent of N_C and thus:

$$\mathrm{cov}(N_B, N_C) = \mathrm{cov}(\widetilde{N}_B + N_{AB}, N_C) = \mathrm{cov}(\widetilde{N}_B, N_C) \tag{C.10}$$

We therefore see that Equation C.7 holds. Let's collect the results so far and summarize them:

$$\begin{aligned}\operatorname{cov}(N_A, N_B, N_C) &= (\overline{N}_A - \overline{N}_{ABC})\operatorname{cov}(N_B, N_C) \\ &\quad + \langle N_{ABC}\,\Delta N_B\,\Delta N_C\rangle - \overline{N}_A \operatorname{cov}(N_B, N_C) \\ &= \langle N_{ABC}\,\Delta N_B\,\Delta N_C\rangle - \overline{N}_{ABC}\operatorname{cov}(N_B, N_C) \qquad \text{(C.11)}\end{aligned}$$

Let's calculate the last expectation. By employing similar algebraic manipulations we get:

$$\langle N_{ABC}\,\Delta N_B\,\Delta N_C\rangle = \overline{N}_{ABC}\big(\operatorname{cov}(N_B, N_C) - \overline{N}_{ABC}\big) + \langle N_{ABC}\,\Delta N_{ABC}\,\Delta N_{ABC}\rangle \qquad \text{(C.12)}$$

The last remaining expectation value can be evaluated directly by using the following identities for a Poisson random variable X:

$$\left\langle X^3\right\rangle = \lambda(1 + 3\lambda + \lambda^2) \quad \left\langle X^2\right\rangle = \lambda^2 + \lambda \qquad \text{(C.13)}$$

We thus obtain:

$$\langle N_{ABC}\Delta N_{ABC}\Delta N_{ABC}\rangle = \lambda_{ABC} + \lambda_{ABC}^2 \qquad \text{(C.14)}$$

Plugging back into Equation C.12 and using $\overline{N}_{ABC} = \lambda_{ABC}$, we obtain:

$$\langle N_{ABC}\,\Delta N_B\,\Delta N_C\rangle = \overline{N}_{ABC}\operatorname{cov}(N_B, N_C) + \lambda_{ABC} \qquad \text{(C.15)}$$

Finally plugging back into Equation C.11, we obtain the simple result:

$$\operatorname{cov}(N_A, N_B, N_C) = \lambda_{ABC} \qquad \text{(C.16)}$$

Appendix D

Select Vibrational Modes of 1,1,1-Trifluoroacetone

Mode	Assignment [140]	Frequency [cm^{-1}]	Period [fs]
1	C–C–C symmetric stretch	774	43
2	CH_3 symmetric rock	962	35
3	CH_3 antisymmetric rock	1027	32
4	CF_3 symmetric stretch	1131	29
5	**CF_3 antisymmetric stretch**	**1189**	**28**
6	CF_3 antisymmetric stretch	1258	27

Table D.1: Various vibrational exitations of 3F-Acetone which have a period around 33 ± 5 fs at the Frank-Condon point of the ground state calculated at B3LYP level of theory, as well as one mode above and below the vibrational period of 33 ± 5. Note that the naming convention is ambiguous as the vibrational terminology is insufficient to describe complicated vibrational modes. Below we display the displacement vectors of each of these modes.

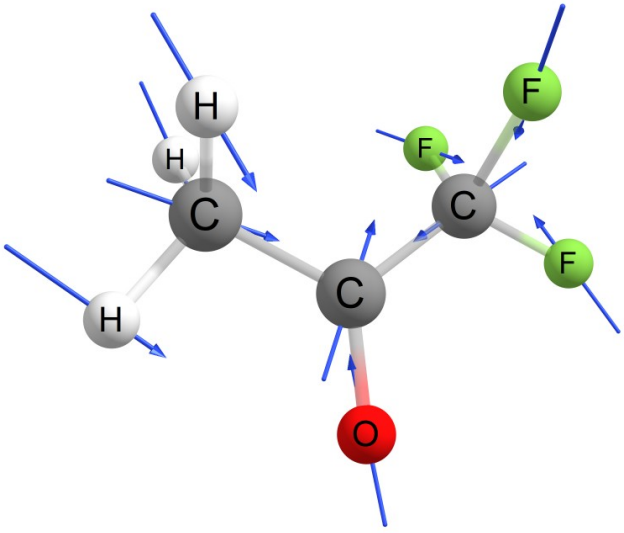

Figure D.1: C–C–C symmetric stretch (Mode 1)

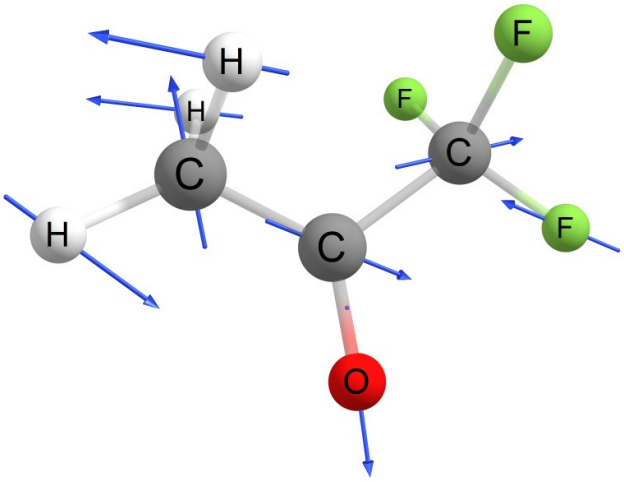

Figure D.2: CH_3 symmetric rock (Mode 2)

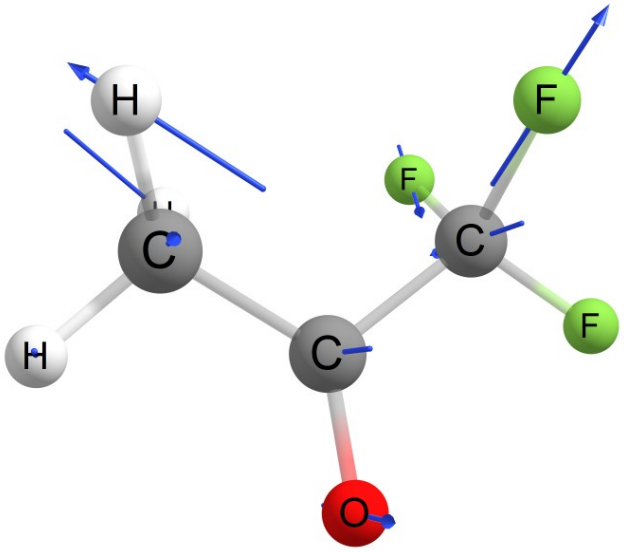

Figure D.3: CH_3 antisymmetric rock (Mode 3)

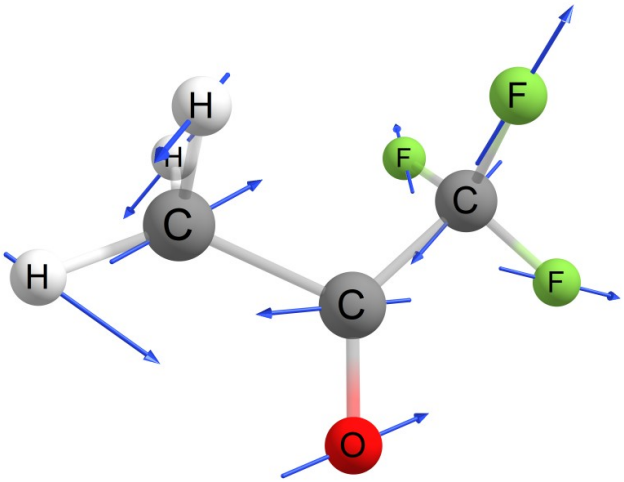

Figure D.4: CF_3 symmetric stretch (Mode 4)

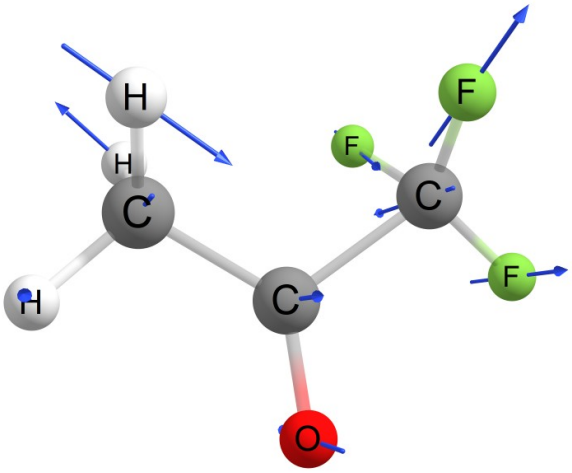

Figure D.5: CF_3 antisymmetric stretch (Mode 5)

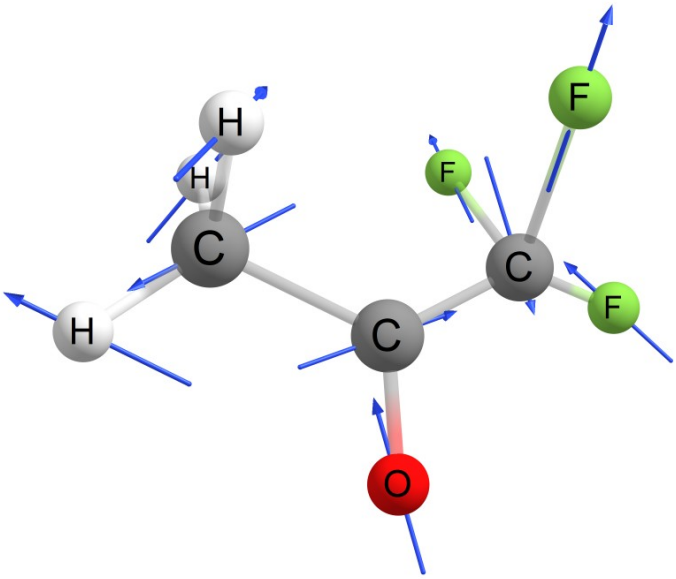

Figure D.6: CF_3 antisymmetric stretch (Mode 6)

Bibliography

[1] Ilyse Resnick, Nora S Newcombe, and Thomas F Shipley. Dealing with big numbers: Representation and understanding of magnitudes outside of human experience. *Cognitive science*, 41(4):1020–1041, 2017.

[2] Noam Chomsky. The responsibility of intellectuals. *The New York review of books*, 23, 1967.

[3] UN ICJ. Allegations of Genocide under the Convention on the Prevention and Punishment of the Crime of Genocide (Ukraine v. Russian Federation) No. 2022/8. 7 March 2022. 2022. URL `https://icj-cij.org/case/182`.

[4] UN ICJ. Application of the Convention on the Prevention and Punishment of the Crime of Genocide in the Gaza Strip (South Africa v. Israel). 2022. URL `https://www.icj-cij.org/case/192`.

[5] Hoesung Lee, Katherine Calvin, Dipak Dasgupta, Gerhard Krinner, Aditi Mukherji, Peter Thorne, Christopher Trisos, José Romero, Paulina Aldunce, and Alexander C Ruane. CLIMATE CHANGE 2023 synthesis report summary for policymakers. *Intergovernmental Panel on Climate Change*, 2024. URL `https://www.ipcc.ch/report/ar6/syr/`.

[6] Dario Polli, Ivan Rivalta, Artur Nenov, O Weingart, Marco Garavelli, and G Cerullo. Tracking the primary photoconversion events in rhodopsins by ultrafast optical spectroscopy. *Photochemical & Photobiological Sciences*, 14(2):213–228, 2015.

[7] H Kandori, Y Shichida, and T Yoshizawa. Photoisomerization in rhodopsin. *Biochemistry (Moscow)*, 66:1197–1209, 2001.

[8] Ming Yan, D Manor, G Weng, H Chao, L Rothberg, TM Jedju, RR Alfano, and RH Callender. Ultrafast spectroscopy of the visual pigment rhodopsin. *Proceedings of the National Academy of Sciences*, 88(21): 9809–9812, 1991.

[9] Abed Mohamadzade and Susanne Ullrich. Internal conversion and intersystem crossing dynamics of uracil upon double thionation: a time-resolved photoelectron spectroscopy study in the gas phase. *Phys. Chem. Chem. Phys.*, 22:15608–15615, 2020. doi: 10.1039/D0CP02145H. URL `http://dx.doi.org/10.1039/D0CP02145H`.

[10] Mariana Assmann, Horst Köppel, and Spiridoula Matsika. Photoelectron Spectrum and Dynamics of the Uracil Cation. *The Journal of Physical Chemistry A*, 119(5):866–875, 2015. doi: 10.1021/jp512221x. URL `https://doi.org/10.1021/jp512221x`. PMID: 25564985.

[11] Spiridoula Matsika, Michael Spanner, Marija Kotur, and Thomas C Weinacht. Ultrafast Relaxation Dynamics of Uracil Probed via Strong Field Dissociative Ionization. *J. Phys. Chem. A*, 117:12796, 2013.

[12] Hanneli R. Hudock, Benjamin G. Levine, Alexis L. Thompson, Helmut Satzger, D. Townsend, N. Gador, S. Ullrich, Albert Stolow, and Todd J. Martínez. Ab Initio Molecular Dynamics and Time-Resolved Photoelectron Spectroscopy of Electronically Excited Uracil and Thymine. *The Journal of Physical Chemistry A*, 111(34):8500–8508, 2007. doi: 10.1021/jp0723665. URL `https://doi.org/10.1021/jp0723665`. PMID: 17685594.

[13] Caroline Arnold, Oriol Vendrell, and Robin Santra. Electronic decoherence following photoionization: Full quantum-dynamical treatment of the influence of nuclear motion. *Physical Review A*, 95(3):033425, 2017.

[14] Gábor Halász, Aurelie Perveaux, Benjamin Lasorne, Michael Robb, Fabien Gatti, and Ágnes Vibók. Coherence revival during the attosecond electronic and nuclear quantum photodynamics of the ozone molecule. *Physical Review A*, 88, 05 2013.

[15] Ignacio Franco, Moshe Shapiro, and Paul Brumer. Femtosecond dynamics and laser control of charge transport in trans-polyacetylene. *The Journal of Chemical Physics*, 128(24):244905, 2008.

[16] Alan Scheidegger, Jiří Vaníček, and Nikolay V Golubev. Search for long-lasting electronic coherence using on-the-fly ab initio semiclassical dynamics. *The Journal of Chemical Physics*, 156(3):034104, 2022.

[17] Hyonseok Hwang and Peter J Rossky. Electronic decoherence induced by intramolecular vibrational motions in a betaine dye molecule. *The Journal of Physical Chemistry B*, 108(21):6723–6732, 2004.

[18] Hideyuki Kamisaka, Svetlana V Kilina, Koichi Yamashita, and Oleg V Prezhdo. Ultrafast vibrationally-induced dephasing of electronic excitations in pbse quantum dots. *Nano Letters*, 6(10):2295–2300, 2006.

[19] Morgane Vacher, Michael J. Bearpark, Michael A. Robb, and João Pedro Malhado. Electron Dynamics upon Ionization of Polyatomic Molecules: Coupling to Quantum Nuclear Motion and Decoherence. *Physical Review Letters*, 118:083001, Feb 2017. doi: 10.1103/PhysRevLett.118.083001. URL `https://link.aps.org/doi/10.1103/PhysRevLett.118.083001`.

[20] Morgane Vacher, Lee Steinberg, Andrew J. Jenkins, Michael J. Bearpark, and Michael A. Robb. Electron dynamics following photoionization: Decoherence due to the nuclear-wave-packet width. *Physical Review A*, 92:040502, Oct 2015. doi: 10.1103/PhysRevA.92.040502. URL `https://link.aps.org/doi/10.1103/PhysRevA.92.040502`.

[21] V. Despré, N. V. Golubev, and A. I. Kuleff. Charge migration in propiolic acid: A full quantum dynamical study. *Physical Review Letters*, 121:203002, 2018.

[22] Robert W Boyd. *Nonlinear Optics*. Academic press, 2019.

[23] Tamas Nagy, Michael Forster, and Peter Simon. Flexible Hollow Fiber for Pulse Compressors. *Applied Optics*, 47(18):3264–3268, 2008.

[24] Tamas Nagy, Martin Kretschmar, Marc J. J. Vrakking, and Arnaud Rouzée. Generation of Above-Terawatt 1.5-Cycle Visible Pulses at 1 kHz by Post-Compression in a Hollow Fiber. *Optics Letters*, 45(12): 3313–3316, 2020.

[25] Anthony Catanese, Brian Kaufman, Chuan Cheng, Eric Jones, Martin G Cohen, and Thomas Weinacht. Acousto-optic modulator pulse-shaper compression of octave-spanning pulses from a stretched hollow-core fiber. *OSA Continuum*, 4(12):3176–3183, 2021.

[26] Richard Abrams. Coupling Losses in Hollow Waveguide Laser Resonators. *IEEE Journal of Quantum Electronics*, 8(11):838–843, 1972.

[27] Ronald Joseph Butler. Analytical Philosophy. *Les Etudes Philosophiques*, 20(4), 1965.

[28] Andrew M Weiner. Ultrafast Optical Pulse Shaping: A Tutorial Review. *Opt. Commun.*, 284(15):3669–3692, 2011.

[29] CW Hillegas, JX Tull, D Goswami, D Strickland, and WS Warren. Femtosecond Laser Pulse Shaping by Use of Microsecond Radio-Frequency Pulses. *Optics Letters*, 19(10):737–739, 1994.

[30] MA Dugan, JX Tull, and WS Warren. High-Resolution Acousto-Optic Shaping of Unamplified and Amplified Femtosecond Laser Pulses. *J. Opt. Soc. Am. B*, 14(9):2348–2358, 1997.

[31] Andrew C. Jones, Miriam Bohlmann Kunz, Isabelle Tigges-Green, and Martin T. Zanni. Dual Spectral Phase and Diffraction Angle Compensation of a Broadband AOM 4-f Pulse-Shaper for Ultrafast Spectroscopy. *Opt. Express*, 27(26):37236, December 2019. ISSN 1094-4087. doi: 10.1364/OE.27.037236.

[32] Andrew M Weiner. Femtosecond Pulse Shaping Using Spatial Light Modulators. *Rev. Sci. Instrum.*, 71(5):1929–1960, 2000.

[33] Miguel Miranda, Cord L. Arnold, Thomas Fordell, Francisco Silva, Benjamín Alonso, Rosa Weigand, Anne L'Huillier, and Helder Crespo. Characterization of broadband few-cycle laser pulses with the

d-scan technique. *Opt. Express*, 20(17):18732–18743, Aug 2012. doi: 10.1364/OE.20.018732. URL https://opg.optica.org/oe/abstract.cfm?URI=oe-20-17-18732.

[34] Miguel Miranda, Thomas Fordell, Cord Arnold, Anne L'Huillier, and Helder Crespo. Simultaneous compression and characterization of ultrashort laser pulses using chirped mirrors and glass wedges. *Opt. Express*, 20(1):688–697, Jan 2012. doi: 10.1364/OE.20.000688. URL https://opg.optica.org/oe/abstract.cfm?URI=oe-20-1-688.

[35] Ian A. Walmsley and Christophe Dorrer. Characterization of ultrashort electromagnetic pulses. *Adv. Opt. Photon.*, 1(2):308–437, Apr 2009. doi: 10.1364/AOP.1.000308. URL https://opg.optica.org/aop/abstract.cfm?URI=aop-1-2-308.

[36] Esmerando Escoto, Ayhan Tajalli, Tamas Nagy, and Günter Steinmeyer. Advanced Phase Retrieval for Dispersion Scan: A Comparative Study. *J. Opt. Soc. Am. B*, 35(1):8–19, January 2018. doi: 10.1364/JOSAB.35.000008.

[37] Miguel Miranda, João Penedones, Chen Guo, Anne Harth, Maïté Louisy, Lana Neoričić, Anne L'Huillier, and Cord L Arnold. Fast Iterative Retrieval Algorithm for Ultrashort Pulse Characterization Using Dispersion Scans. *JOSA B*, 34(1):190–197, 2017.

[38] Daniel E Wilcox, Franklin D Fuller, and Jennifer P Ogilvie. Fast second-harmonic generation frequency-resolved optical gating using only a pulse shaper. *Optics Letters*, 38(16):2980–2983, 2013.

[39] Nicolas Forget, Vincent Crozatier, and Thomas Oksenhendler. Pulse-measurement techniques using a single amplitude and phase spectral shaper. *J. Opt. Soc. Am. B*, 27(4):742–756, Apr 2010. doi: 10.1364/JOSAB.27.000742. URL https://opg.optica.org/josab/abstract.cfm?URI=josab-27-4-742.

[40] Ivan Amat-Roldán, Iain G. Cormack, Pablo Loza-Alvarez, Emilio J. Gualda, and David Artigas. Ultrashort Pulse Characterisation with

SHG Collinear-FROG. *Opt. Express*, 12(6):1169–1178, March 2004. doi: 10.1364/OPEX.12.001169.

[41] Brian Kaufman. *Coherent Control Spectroscopy of Electronic and Nuclear Dynamics*. PhD thesis, Stony Brook University, 2023. Copyright - Database copyright ProQuest LLC; ProQuest does not claim copyright in the individual underlying works; Last updated - 2023-09-12.

[42] John H. Moore, Christopher C. Davis, Michael A. Coplan, and Sandra C. Greer. *Building Scientific Apparatus*. Cambridge University Press, 4 edition, 2009.

[43] André T. J. B. Eppink and David H. Parker. Velocity map imaging of ions and electrons using electrostatic lenses: Application in photoelectron and photofragment ion imaging of molecular oxygen. *Review of Scientific Instruments*, 68(9):3477–3484, 09 1997. ISSN 0034-6748. doi: 10.1063/1.1148310. URL `https://doi.org/10.1063/1.1148310`.

[44] Vladimir Dribinski, Alexei Ossadtchi, Vladimir A. Mandelshtam, and Hanna Reisler. Reconstruction of Abel-transformable Images: The Gaussian Basis-Set Expansion Abel Transform Method. *Rev. Sci. Inst.*, 73 (7):2634–2642, 2002. doi: 10.1063/1.1482156.

[45] Gustavo A. Garcia, Laurent Nahon, and Ivan Powis. Two-dimensional charged particle image inversion using a polar basis function expansion. *Review of Scientific Instruments*, 75(11):4989–4996, 11 2004. ISSN 0034-6748. doi: 10.1063/1.1807578. URL `https://doi.org/10.1063/1.1807578`.

[46] Michael Davino, Edward McManus, Nora G. Helming, Chuan Cheng, Gönenç Moğol, Zhanna Rodnova, Geoffrey Harrison, Kevin Watson, Thomas Weinacht, George N. Gibson, Tobias Saule, and Carlos A. Trallero-Herrero. A plano–convex thick-lens velocity map imaging apparatus for direct, high resolution 3D momentum measurements of photoelectrons with ion time-of-flight coincidence. *Review of Scientific Instruments*, 94(1):013303, 01 2023. ISSN 0034-6748. doi: 10.1063/5.0129900. URL `https://doi.org/10.1063/5.0129900`.

[47] T Poikela, J Plosila, T Westerlund, M Campbell, M De Gaspari, X Llopart, V Gromov, R Kluit, M van Beuzekom, F Zappon, V Zivkovic, C Brezina, K Desch, Y Fu, and A Kruth. Timepix3: a 65K channel hybrid pixel readout chip with simultaneous ToA/ToT and sparse readout. *Journal of Instrumentation*, 9(05):C05013, 2014. doi: 10.1088/1748-0221/9/05/c05013. URL https://doi.org/10.1088/1748-0221/9/05/c05013.

[48] Andrei Nomerotski. Imaging and time stamping of photons with nanosecond resolution in Timepix based optical cameras. *Nuclear Instruments and Methods in Physics Research Section A: Accelerators, Spectrometers, Detectors and Associated Equipment*, 937:26–30, September 2019. doi: 10.1016/j.nima.2019.05.034. URL https://doi.org/10.1016/j.nima.2019.05.034.

[49] Timepix3, Knowledge Transfer Group at Cern. https://kt.cern/technologies/timepix3. Accessed: 2024-05-21.

[50] Arthur Zhao, Martin van Beuzekom, Bram Bouwens, Dmitry Byelov, Irakli Chakaberia, Chuan Cheng, Erik Maddox, Andrei Nomerotski, Peter Svihra, Jan Visser, Vaclav Vrba, and Thomas Weinacht. Coincidence velocity map imaging using Tpx3Cam, a time stamping optical camera with 1.5 ns timing resolution. *Review of Scientific Instruments*, 88(11):113104, 2017. doi: 10.1063/1.4996888. URL https://doi.org/10.1063/1.4996888.

[51] Paul B. Corkum. Plasma perspective on strong field multiphoton ionization. *Phys. Rev. Lett.*, 71:1994–1997, Sep 1993. doi: 10.1103/PhysRevLett.71.1994. URL https://link.aps.org/doi/10.1103/PhysRevLett.71.1994.

[52] K. J. Schafer, Baorui Yang, L. F. DiMauro, and K. C. Kulander. Above threshold ionization beyond the high harmonic cutoff. *Phys. Rev. Lett.*, 70:1599–1602, Mar 1993. doi: 10.1103/PhysRevLett.70.1599. URL https://link.aps.org/doi/10.1103/PhysRevLett.70.1599.

[53] Chuan Cheng, Ruaridh Forbes, Andrew J. Howard, Michael Spanner, Philip H. Bucksbaum, and Thomas Weinacht. Momentum-resolved

above-threshold ionization of deuterated water. *Phys. Rev. A*, 102: 052813, Nov 2020. doi: 10.1103/PhysRevA.102.052813. URL https://link.aps.org/doi/10.1103/PhysRevA.102.052813.

[54] David W. Chandler and Paul L. Houston. Two-dimensional imaging of state-selected photodissociation products detected by multiphoton ionization. *The Journal of Chemical Physics*, 87(2):1445–1447, 1987. doi: 10.1063/1.453276. URL https://doi.org/10.1063/1.453276.

[55] Arno Vredenborg, Wim G. Roeterdink, and Maurice H. M. Janssen. A photoelectron-photoion coincidence imaging apparatus for femtosecond time-resolved molecular dynamics with electron time-of-flight resolution of σ=18ps and energy resolution ΔE/E=3.5%. *Review of Scientific Instruments*, 79(6):063108, 2008. doi: 10.1063/1.2949142. URL https://doi.org/10.1063/1.2949142.

[56] Thomas Weinacht and Brett J. Pearson. *Time-Resolved Spectroscopy: An Experimental Perspective*. CRC Press, 2019. ISBN 9780367780401.

[57] Katharine L. Reid. Photoelectron Angular Distributions. *Annual Review of Physical Chemistry*, 54(Volume 54, 2003):397–424, 2003. ISSN 1545-1593. doi: 10.1146/annurev.physchem.54.011002.103814. URL https://www.annualreviews.org/content/journals/10.1146/annurev.physchem.54.011002.103814.

[58] J. A. Davies, R. E. Continetti, D. W. Chandler, and C. C. Hayden. Femtosecond Time-Resolved Photoelectron Angular Distributions Probed during Photodissociation of NO_2. *Phys. Rev. Lett.*, 84:5983–5986, Jun 2000. doi: 10.1103/PhysRevLett.84.5983. URL https://link.aps.org/doi/10.1103/PhysRevLett.84.5983.

[59] Stephan Thürmer, Robert Seidel, Manfred Faubel, Wolfgang Eberhardt, John C. Hemminger, Stephen E. Bradforth, and Bernd Winter. Photoelectron Angular Distributions from Liquid Water: Effects of Electron Scattering. *Phys. Rev. Lett.*, 111:173005, Oct 2013. doi: 10.1103/PhysRevLett.111.173005. URL https://link.aps.org/doi/10.1103/PhysRevLett.111.173005.

[60] Yusong Liu, Pratip Chakraborty, Spiridoula Matsika, and Thomas Weinacht. Excited state dynamics of cis,cis-1,3-cyclooctadiene: UV pump VUV probe time-resolved photoelectron spectroscopy. *The Journal of Chemical Physics*, 153(7):074301, 08 2020. ISSN 0021-9606. doi: 10.1063/5.0006920. URL https://doi.org/10.1063/5.0006920.

[61] Pratip Chakraborty, Yusong Yusong Liu, Thomas Weinacht, and Spiridoula Matsika. Excited state dynamics of cis,cis-1,3-cyclooctadiene: Non-adiabatic trajectory surface hopping. *The Journal of Chemical Physics*, 152:174302, 05 2020. doi: 10.1063/5.0005558.

[62] Christoph R. Gebhardt, T. Peter Rakitzis, Peter C. Samartzis, Vlassis Ladopoulos, and Theofanis N. Kitsopoulos. Slice imaging: A new approach to ion imaging and velocity mapping. *Review of Scientific Instruments*, 72(10):3848–3853, 10 2001. ISSN 0034-6748. doi: 10.1063/1.1403010. URL https://doi.org/10.1063/1.1403010.

[63] Dave Townsend, Michael P. Minitti, and Arthur G. Suits. Direct current slice imaging. *Review of Scientific Instruments*, 74(4):2530–2539, 04 2003. ISSN 0034-6748. doi: 10.1063/1.1544053. URL https://doi.org/10.1063/1.1544053.

[64] Suk Kyoung Lee, Yun Fei Lin, Steven Lingenfelter, Lin Fan, Alexander H. Winney, and Wen Li. Communication: Time- and space-sliced velocity map electron imaging. *The Journal of Chemical Physics*, 141 (22):221101, 12 2014. ISSN 0021-9606. doi: 10.1063/1.4903744. URL https://doi.org/10.1063/1.4903744.

[65] Gönenç Moğol, Chuan Cheng, Thomas Weinacht, Andrei Nomerotski, and Carlos Trallero-Herrero. 3D velocity map imaging of electrons with TPX3CAM. *Review of Scientific Instruments*, 93(1):013003, 01 2022. ISSN 0034-6748. doi: 10.1063/5.0071804. URL https://doi.org/10.1063/5.0071804.

[66] Simion Software. https://simion.com/. Accessed: 2024-05-23.

[67] Gönenç Moğol. GitHub Repository for Timepix Camera. https://github.com/gmogol/Timepix. Accessed: 2024-05-23.

[68] NG Kling, D Paul, A Gura, G Laurent, S De, H Li, Z Wang, B Ahn, CH Kim, TK Kim, et al. Thick-lens velocity-map imaging spectrometer with high resolution for high-energy charged particles. *Journal of Instrumentation*, 9(05):P05005, 2014.

[69] Joseph Ladislas Wiza et al. Microchannel plate detectors. *Nucl. Instrum. Methods*, 162(1-3):587–601, 1979.

[70] X. Llopart, J. Alozy, Rafael Ballabriga, Michael Campbell, R. Casanova, V. Gromov, Erik Heijne, T. Poikela, Edinei Santin, Viros Sriskaran, L. Tlustos, and A. Vitkovskiy. Timepix4, a large area pixel detector readout chip which can be tiled on 4 sides providing sub-200 ps timestamp binning. *Journal of Instrumentation*, 17:C01044, 01 2022. doi: 10.1088/1748-0221/17/01/C01044.

[71] R. Ballabriga, J.A. Alozy, F.N. Bandi, G. Blaj, M. Campbell, P. Christodoulou, V. Coco, A. Dorda, S. Emiliani, K. Heijhoff, E. Heijne, T. Hofmann, J. Kaplon, A. Koukab, I. Kremastiotis, X. Llopart, M. Noy, A. Paterno, M. Piller, J.M. Sallesse, Sriskaran V., L. Tlustos, and M. van Beuzekom. The Timepix4 analog front-end design: Lessons learnt on fundamental limits to noise and time resolution in highly segmented hybrid pixel detectors. *Nuclear Instruments and Methods in Physics Research Section A: Accelerators, Spectrometers, Detectors and Associated Equipment*, 1045:167489, 2023. ISSN 0168-9002. doi: 10.1016/j.nima.2022.167489. URL `https://www.sciencedirect.com/science/article/pii/S0168900222007811`.

[72] X. Llopart. The Timepix4 chip and its design approach. In *The 28th International Workshop on Vertex Detectors, 13-18 October*, page 18, 2019.

[73] H. Kollmus, W. Schmitt, R. Moshammer, M. Unverzagt, and J. Ullrich. A high resolution 4pi multi-electron spectrometer for soft electrons. *Nuclear Instruments and Methods in Physics Research Section B: Beam Interactions with Materials and Atoms*, 124(2): 377–380, 1997. ISSN 0168-583X. doi: 10.1016/S0168-583X(96)00819-1. URL `https://www.sciencedirect.com/science/article/pii/S0168583X96008191`. Fast Ion-Atom Collisions.

[74] J Ullrich, R Moshammer, R Dörner, O Jagutzki, V Mergel, H Schmidt-Böcking, and L Spielberger. Recoil-ion momentum spectroscopy. *J. Phys. B: At. Mol. Opt. Phys.*, 30(13):2917, 1997.

[75] R. Dörner, V. Mergel, O. Jagutzki, L. Spielberger, J. Ullrich, R. Moshammer, and H. Schmidt-Böcking. Cold Target Recoil Ion Momentum Spectroscopy: a 'momentum microscope' to view atomic collision dynamics. *Phys. Rep.*, 330:95, 2000.

[76] J Ullrich, R Moshammer, A Dorn, R Dörner, L Ph H Schmidt, and H Schmidt-Böcking. Recoil-ion and electron momentum spectroscopy: reaction-microscopes. *Reports on Progress in Physics*, 66(9):1463–1545, aug 2003. doi: 10.1088/0034-4885/66/9/203. URL `https://doi.org/10.1088/0034-4885/66/9/203`.

[77] Timur Osipov. *Experimental study of photo-electron diffraction from two-center molecules by means of the Coltrims technique*. Kansas State University, 2003.

[78] Ottmar Jagutzki, Alfred Cerezo, Achim Czasch, R Dorner, M Hattas, Min Huang, Volker Mergel, Uwe Spillmann, Klaus Ullmann-Pfleger, Thorsten Weber, et al. Multiple hit readout of a microchannel plate detector with a three-layer delay-line anode. *IEEE Transactions on Nuclear Science*, 49(5):2477–2483, 2002.

[79] W. Iskandar, T. N. Rescigno, A. E. Orel, T. Severt, K. A. Larsen, Z. L. Streeter, B. Jochim, B. Griffin, D. Call, V. Davis, C. W. McCurdy, R. R. Lucchese, J. B. Williams, I. Ben-Itzhak, D. S. Slaughter, and Th. Weber. Efficiency of charge transfer in changing the dissociation dynamics of OD+ transients formed after the photo-fragmentation of D2O. *The Journal of Chemical Physics*, 159(9):094301, 09 2023. ISSN 0021-9606. doi: 10.1063/5.0159300. URL `https://doi.org/10.1063/5.0159300`.

[80] Chuan Cheng. *Momentum Resolved Coincidence and Covariance Measurements of Strong Field Molecular Ionization*. PhD thesis, Stony Brook University, 2023 2023. Copyright - Database copyright ProQuest LLC;

ProQuest does not claim copyright in the individual underlying works; Last updated - 2023-10-24.

[81] JHD Eland. Dynamics of fragmentation reactions from peak shapes in multiparticle coincidence experiments. *Laser Chemistry*, 11(3-4):259–263, 1991.

[82] T Jahnke, Th Weber, T Osipov, AL Landers, O Jagutzki, L Ph H Schmidt, CL Cocke, MH Prior, H Schmidt-Böcking, and R Dörner. Multicoincidence studies of photo and Auger electrons from fixed-in-space molecules using the COLTRIMS technique. *Journal of Electron Spectroscopy and Related Phenomena*, 141(2-3):229–238, 2004.

[83] M Lavollée and H Bergeron. Data treatment in multiparticle coincidence experiments: two-step dissociation processes. *Journal of Physics B: Atomic, Molecular and Optical Physics*, 25(14):3101, 1992.

[84] F Légaré, Kevin F Lee, IV Litvinyuk, PW Dooley, SS Wesolowski, PR Bunker, Peter Dombi, Ferenc Krausz, AD Bandrauk, DM Villeneuve, et al. Laser Coulomb-explosion imaging of small molecules. *Phys. Rev. A*, 71(1):013415, 2005.

[85] Surjendu Bhattacharyya, Kurtis Borne, Farzaneh Ziaee, Shashank Pathak, Enliang Wang, Anbu Selvam Venkatachalam, Nathan Marshall, Kevin D. Carnes, Charles W. Fehrenbach, Travis Severt, Itzik Ben-Itzhak, Artem Rudenko, and Daniel Rolles. Two- and three-body fragmentation of multiply charged tribromomethane by ultrafast laser pulses. *Phys. Chem. Chem. Phys.*, 24:27631–27644, 2022. doi: 10.1039/D2CP03089F. URL `http://dx.doi.org/10.1039/D2CP03089F`.

[86] I. Ben-Itzhak, A. Max Sayler, M. Leonard, J.W. Maseberg, D. Hathiramani, E. Wells, M.A. Smith, Jiangfan Xia, Pengqian Wang, K.D. Carnes, and B.D. Esry. Bond rearrangement caused by sudden single and multiple ionization of water molecules. *Nuclear Instruments and Methods in Physics Research Section B: Beam Interactions with Materials and Atoms*, 233(1):284–292, 2005. ISSN 0168-583X. doi: 10.1016/j.nimb.2005.03.123. URL `https://www.sciencedirect.com/science/article/pii/S0168583X05003472`. Fast Ion-Atom Collisions.

[87] Tomoyuki Endo, Simon P. Neville, Vincent Wanie, Samuel Beaulieu, Chen Qu, Jude Deschamps, Philippe Lassonde, Bruno E. Schmidt, Hikaru Fujise, Mizuho Fushitani, Akiyoshi Hishikawa, Paul L. Houston, Joel M. Bowman, Michael S. Schuurman, François Légaré, and Heide Ibrahim. Capturing roaming molecular fragments in real time. *Science (80-.).*, 370(6520):1072–1077, nov 2020. ISSN 10959203. doi: 10.1126/science.abc2960.

[88] Martin Pitzer, Maksim Kunitski, Allan S. Johnson, Till Jahnke, Hendrik Sann, Felix Sturm, Lothar Ph. H. Schmidt, Horst Schmidt-Böcking, Reinhard Dörner, Jürgen Stohner, Julia Kiedrowski, Michael Reggelin, Sebastian Marquardt, Alexander Schießer, Robert Berger, and Markus S. Schöffler. Direct Determination of Absolute Molecular Stereochemistry in Gas Phase by Coulomb Explosion Imaging. *Science*, 341(6150):1096–1100, 2013. doi: 10.1126/science.1240362. URL `https://www.science.org/doi/abs/10.1126/science.1240362`.

[89] K. Codling, L. J. Frasinski, P. A. Hatherly, and M. Stankiewicz. New triple coincidence techniques applied to multiple ionisation of molecules. *Phys. Scr.*, 41(4):433–439, apr 1990. ISSN 14024896. doi: 10.1088/0031-8949/41/4/012.

[90] LJ Frasinski, K Codling, and PA Hatherly. Covariance mapping: A correlation method applied to multiphoton multiple ionization. *Science*, 246(4933):1029–1031, 1989.

[91] L. J. Frasinski, P. A. Hatherly, and K. Codling. Multiphoton multiple ionisation of N2O probed by three-dimensional covariance mapping. *Phys. Lett. A*, 156(5):227–232, jun 1991. ISSN 03759601. doi: 10.1016/0375-9601(91)90145-X.

[92] L J Frasinski, M Stankiewicz, P A Hatherly, G M Cross, K Codling, A J Langley, and W Shaikh. Molecular H2 in intense laser fields probed by electron-electron, electron-ion, and ion-ion covariance techniques. *Phys. Rev. A*, 46(11), 1992. ISSN 10502947. doi: 10.1103/PhysRevA.46.R6789.

[93] V Zhaunerchyk, M Mucke, P Salén, P vd Meulen, M Kaminska, R J Squibb, L J Frasinski, M Siano, J. H.D. Eland, P Linusson, R D Thomas,

M Larsson, L Foucar, J Ullrich, K Motomura, S Mondal, K Ueda, T Osipov, L Fang, B F Murphy, N Berrah, C Bostedt, J D Bozek, S Schorb, M Messerschmidt, J M Glownia, J P Cryan, R N Coffee, O Takahashi, S Wada, M N Piancastelli, R Richter, K C Prince, and R Feifel. Using covariance mapping to investigate the dynamics of multi-photon ionization processes of Ne atoms exposed to X-FEL pulses. *J. Phys. B At. Mol. Opt. Phys.*, 46(16):164034, aug 2013. ISSN 09534075. doi: 10.1088/0953-4075/46/16/164034.

[94] Vitali Zhaunerchyk, LJ Frasinski, John HD Eland, and Raimund Feifel. Theory and simulations of covariance mapping in multiple dimensions for data analysis in high-event-rate experiments. *Physical Review A*, 89 (5):053418, 2014.

[95] M. Mucke, V. Zhaunerchyk, L. J. Frasinski, R. J. Squibb, M. Siano, J. H.D. Eland, P. Linusson, P. Salén, P. V.D. Meulen, R. D. Thomas, M. Larsson, L. Foucar, J. Ullrich, K. Motomura, S. Mondal, K. Ueda, T. Osipov, L. Fang, B. F. Murphy, N. Berrah, C. Bostedt, J. D. Bozek, S. Schorb, M. Messerschmidt, J. M. Glownia, J. P. Cryan, R. N. Coffee, O. Takahashi, S. Wada, M. N. Piancastelli, R. Richter, K. C. Prince, and R. Feifel. Covariance mapping of two-photon double core hole states in C2H2 and C2H6 produced by an X-ray free electron laser. *New J. Phys.*, 17(7), 2015. ISSN 13672630. doi: 10.1088/1367-2630/17/7/073002.

[96] Leszek J Frasinski. Covariance mapping techniques. *J. Phys. B*, 49(15): 152004, 2016. ISSN 0953-4075. doi: 10.1088/0953-4075/49/15/152004.

[97] L. J. Frasinski, V. Zhaunerchyk, M. Mucke, R. J. Squibb, M. Siano, J. H.D. Eland, P. Linusson, P. V.d. Meulen, P. Salén, R. D. Thomas, M. Larsson, L. Foucar, J. Ullrich, K. Motomura, S. Mondal, K. Ueda, T. Osipov, L. Fang, B. F. Murphy, N. Berrah, C. Bostedt, J. D. Bozek, S. Schorb, M. Messerschmidt, J. M. Glownia, J. P. Cryan, R. N. Coffee, O. Takahashi, S. Wada, M. N. Piancastelli, R. Richter, K. C. Prince, and R. Feifel. Dynamics of hollow atom formation in intense X-ray pulses probed by partial covariance mapping. *Phys. Rev. Lett.*, 111(7):073002, aug 2013. ISSN 00319007. doi: 10.1103/PhysRevLett.111.073002.

[98] O Kornilov, M Eckstein, M Rosenblatt, C P Schulz, K Motomura, A Rouzée, J Klei, L Foucar, M Siano, A Lübcke, F Schapper, P Johnsson, D. M.P. Holland, T Schlathölter, T Marchenko, S Düsterer, K Ueda, M. J.J. Vrakking, and L J Frasinski. Coulomb explosion of diatomic molecules in intense XUV fields mapped by partial covariance. *J. Phys. B At. Mol. Opt. Phys.*, 46(16):164028, 2013. ISSN 09534075. doi: 10.1088/0953-4075/46/16/164028.

[99] Jochen Mikosch, Andrey E. Boguslavskiy, Iain Wilkinson, Michael Spanner, Serguei Patchkovskii, and Albert Stolow. Channel- and Angle-Resolved Above Threshold Ionization in the Molecular Frame. *Phys. Rev. Lett.*, 110:023004, 2013.

[100] Andrey E Boguslavskiy, Jochen Mikosch, Arjan Gijsbertsen, Michael Spanner, Serguei Patchkovskii, Niklas Gador, Marc J. J. Vrakking, and Albert Stolow. The multielectron ionization dynamics underlying attosecond strong-field spectroscopies. *Science*, 335(6074):1336–40, mar 2012. ISSN 1095-9203. doi: 10.1126/science.1212896.

[101] Chuan Cheng, Vaibhav Singh, Spiridoula Matsika, and Thomas Weinacht. Strong Field Double Ionization of Formaldehyde Investigated Using Momentum Resolved Covariance Imaging and Trajectory Surface Hopping. *The Journal of Physical Chemistry A*, 126(40):7399–7406, 2022.

[102] Chuan Cheng, Patricia Vindel-Zandbergen, Spiridoula Matsika, and Thomas Weinacht. Electron correlation in channel-resolved strong-field molecular double ionization. *Phys. Rev. A*, 100(5):053405, nov 2019. ISSN 24699934. doi: 10.1103/PhysRevA.100.053405.

[103] Felix Allum, Chuan Cheng, Andrew J Howard, Philip H Bucksbaum, Mark Brouard, Thomas Weinacht, and Ruaridh Forbes. Multi-Particle Three-Dimensional Covariance Imaging:"Coincidence" Insights into the Many-Body Fragmentation of Strong-Field Ionized D2O. *J. Phys. Chem. Lett.*, 12(34):8302–8308, 2021.

[104] L J Frasinski. Cumulant mapping as the basis of multi-dimensional spectrometry. *Physical Chemistry Chemical Physics*, 24:20776, 2022.

[105] Chuan Cheng, Leszek J. Frasinski, Gönenç Moğol, Felix Allum, Andrew J. Howard, Daniel Rolles, Philip H. Bucksbaum, Mark Brouard, Ruaridh Forbes, and Thomas Weinacht. Multiparticle Cumulant Mapping for Coulomb Explosion Imaging. *Phys. Rev. Lett.*, 130(9):093203, 2023.

[106] Chuan Cheng, Leszek J. Frasinski, Gönenç Moğol, Felix Allum, Andrew J. Howard, Philip H. Bucksbaum, Ruaridh Forbes, and Thomas Weinacht. Multiparticle cumulant mapping for Coulomb explosion imaging: Calculations and algorithm. *Phys. Rev. A*, 109:042802, Apr 2024. doi: 10.1103/PhysRevA.109.042802. URL `https://link.aps.org/doi/10.1103/PhysRevA.109.042802`.

[107] George Casella and Roger Berger *Statistical Inference*. CRC Press, 2001. ISBN 9780534243128

[108] Julia Codere, Michael Belmonte, Brian Kaufman, Michael Wahl, Eric Jones, Martin G Cohen, Thomas Weinacht, and Ruaridh Forbes. High repetition-rate pulse shaping of a spectrally broadened Yb femtosecond laser. *Opt. Continuum*, 3(5):785–794, May 2024. doi: 10.1364/OPTCON.522036. URL `https://opg.optica.org/optcon/abstract.cfm?URI=optcon-3-5-785`.

[109] Felix Allum, Nils Anders, Mark Brouard, Phil H. Bucksbaum, Michael Burt, Briony Downes-ward, Sven Grundmann, James Harries, Yudai Ishimura, Hiroshi Iwayama, Leon Kaiser, Edwin Kukk, Jason W.L. Lee, Xiaojing Liu, Russell S Minns, Kiyonobu Nagaya, Akinobu Niozu, Johannes Niskanen, Jordan T. O'Neal, Shigeki Owada, James Pickering, Daniel Rolles, Artem Rudenko, Shu Saito, Kiyoshi Ueda, Claire Vallance, Nicholas Werby, Joanne Woodhouse, Daehyun You, Farzaneh Ziaee, Taran Driver, and Ruaridh Forbes. Multi-channel photodissociation and XUV-induced charge transfer dynamics in strong-field-ionized methyl iodide studied with time-resolved recoil-frame covariance imaging. *Faraday Discuss.*, 2020. ISSN 1359-6640. doi: 10.1039/d0fd00115e.

[110] Nagitha Ekanayake, Travis Severt, Muath Nairat, Nicholas P Weingartz, Benjamin M Farris, Balram Kaderiya, Peyman Feizollah, Bethany

Jochim, Farzaneh Ziaee, Kurtis Borne, et al. H2 roaming chemistry and the formation of H3+ from organic molecules in strong laser fields. *Nature communications*, 9(1):5186, 2018.

[111] S. Zhao, Bethany Jochim, Peyman Feizollah, Jyoti Rajput, F. Ziaee, Kanaka Raju P., B. Kaderiya, K. Borne, Y. Malakar, Ben Berry, J. Harrington, D. Rolles, A. Rudenko, K. D. Carnes, E. Wells, I. Ben-Itzhak, and T. Severt. Strong-field-induced bond rearrangement in triatomic molecules. *Phys. Rev. A*, 99:053412, May 2019. doi: 10.1103/PhysRevA.99.053412. URL https://link.aps.org/doi/10.1103/PhysRevA.99.053412.

[112] Jiaqi Zhou, Yutian Li, Yingying Wang, Shaokui Jia, Xiaorui Xue, Tao Yang, Zhen Zhang, Alexander Dorn, and Xueguang Ren. Ultrafast ring-opening fragmentation dynamics of $C_6H_6{}^{3+}$ induced by electron-impact ionization. *Phys. Rev. A*, 104:032807, Sep 2021. doi: 10.1103/PhysRevA.104.032807. URL https://link.aps.org/doi/10.1103/PhysRevA.104.032807.

[113] Y. Li, M. Li, T. Yang, Y. Wang, S. Jia, X. Liu, and Z. Xu. Theoretical study on the formation mechanisms of CH3+ from doubly charged benzene. *Chemical Physics*, 553:111358, 2022. ISSN 0301-0104. doi: 10.1016/j.chemphys.2021.111358. URL https://www.sciencedirect.com/science/article/pii/S030101042100269X.

[114] Paul B. Corkum and Ferenc Krausz. Attosecond science. *Nature Physics*, 3(6):381–387, 2007.

[115] Alicia Palacios and Fernando Martín. The quantum chemistry of attosecond molecular science. *Wiley Interdisciplinary Reviews: Computational Molecular Science*, 10(1):e1430, 2020.

[116] Lisa-Marie Koll, Laura Maikowski, Lorenz Drescher, Tobias Witting, and Marc J. J. Vrakking. Experimental Control of Quantum-Mechanical Entanglement in an Attosecond Pump-Probe Experiment. *Physical Review Letters*, 128:043201, Jan 2022. doi: 10.1103/PhysRevLett.128.043201. URL https://link.aps.org/doi/10.1103/PhysRevLett.128.043201.

[117] Marc J. J. Vrakking. Ion-photoelectron entanglement in photoionization with chirped laser pulses. *Journal of Physics B*, 55(13):134001, jun 2022. doi: 10.1088/1361-6455/ac6e17. URL https://dx.doi.org/10.1088/1361-6455/ac6e17.

[118] Marc J. J. Vrakking. Control of Attosecond Entanglement and Coherence. *Physical Review Letters*, 126:113203, Mar 2021. doi: 10.1103/PhysRevLett.126.113203. URL https://link.aps.org/doi/10.1103/PhysRevLett.126.113203.

[119] Hong-Guang Duan, Valentyn I Prokhorenko, Richard J Cogdell, Khuram Ashraf, Amy L Stevens, Michael Thorwart, and RJ Dwayne Miller. Nature does not rely on long-lived electronic quantum coherence for photosynthetic energy transfer. *Proceedings of the National Academy of Sciences*, 114(32):8493–8498, 2017.

[120] Margherita Maiuri, Evgeny E Ostroumov, Rafael G Saer, Robert E Blankenship, and Gregory D Scholes. Coherent wavepackets in the Fenna–Matthews–Olson complex are robust to excitonic-structure perturbations caused by mutagenesis. *Nature Chemistry*, 10(2):177–183, 2018.

[121] Mario Barbatti, Antonio Carlos Borin, and Susanne Ullrich. *Photoinduced Processes in Nucleic Acids*, pages 1–32. Springer International Publishing, Cham, 2015. ISBN 978-3-319-13371-3. URL https://doi.org/10.1007/128_2014_569.

[122] Helmut Satzger, Dave Townsend, Marek Z Zgierski, Serguei Patchkovskii, Susanne Ullrich, and Albert Stolow. Primary processes underlying the photostability of isolated DNA bases: Adenine. *Proceedings of the National Academy of Sciences*, 103(27):10196–10201, 2006.

[123] H. Maeda and T. F. Gallagher. Nondispersing Wave Packets. *Physical Review Letters*, 92:133004, Apr 2004. doi: 10.1103/PhysRevLett.92.133004. URL https://link.aps.org/doi/10.1103/PhysRevLett.92.133004.

[124] T. C. Weinacht, J. Ahn, and P. H. Bucksbaum. Measurement of the Amplitude and Phase of a Sculpted Rydberg Wave Packet. *Physical Review Letters*, 80:5508–5511, Jun 1998. doi: 10.1103/PhysRevLett.80.5508. URL https://link.aps.org/doi/10.1103/PhysRevLett.80.5508.

[125] John A. Yeazell, Mark Mallalieu, and C. R. Stroud. Observation of the collapse and revival of a Rydberg electronic wave packet. *Physical Review Letters*, 64:2007–2010, Apr 1990. doi: 10.1103/PhysRevLett.64.2007. URL https://link.aps.org/doi/10.1103/PhysRevLett.64.2007.

[126] Gönenç Moğol, Brian Kaufman, Thomas Weinacht, Chuan Cheng, and Itzik Ben-Itzhak. Direct observation of entangled electronic-nuclear wave packets. *Phys. Rev. Res.*, 6:L022047, May 2024. doi: 10.1103/PhysRevResearch.6.L022047. URL https://link.aps.org/doi/10.1103/PhysRevResearch.6.L022047.

[127] Brian Kaufman, Philipp Marquetand, Tamás Rozgonyi, and Thomas Weinacht. Long-Lived Electronic Coherences in Molecules. *Physical Review Letters*, 131:263202, Dec 2023. doi: 10.1103/PhysRevLett.131.263202. URL https://link.aps.org/doi/10.1103/PhysRevLett.131.263202.

[128] Brian Kaufman, Philipp Marquetand, Tamás Rozgonyi, and Thomas Weinacht. Long Lived Electronic Coherences in Molecular Wave Packets Probed with Pulse Shape Spectroscopy. *Arxiv Preprint*. URL https://arxiv.org/abs/2311.10598.

[129] Tamas Nagy, Peter Simon, and Laszlo Veisz. High-energy few-cycle pulses: post-compression techniques. *Advances in Physics: X* , 6(1): 2020. URL https://doi.org/10.1080/23746149.2020.1845795.

[130] Tamas Nagy, Vladimir Pervak, and Peter Simon. Optimal pulse compression in long hollow fibers. *Optics Letters*, 36, pages 4422–4424, 2011. URL https://doi.org/10.1364/OL.36.004422.

[131] Brian Kaufman, Philipp Marquetand, Thomas Weinacht, and Tamás Rozgonyi. Numerical calculations of multiphoton molecular absorption. *Physical Review A*, 106(1):013111, 2022.

[132] William DM Lunden, Péter Sándor, Thomas C Weinacht, and Tamás Rozgonyi. Model for describing resonance-enhanced strong-field ionization with shaped ultrafast laser pulses. *Physical Review A*, 89(5):053403, 2014.

[133] B. J. Cocksey, J. H. D. Eland, and C. J. Danby. The effect of alkyl substitution on ionisation potential. *J. Chem. Soc. B*, pages 790–792, 1971. doi: 10.1039/J29710000790. URL http://dx.doi.org/10.1039/J29710000790.

[134] V. Y. Young and K. L. Cheng. The photoelectron spectra of halogen substituted acetones. *The Journal of Chemical Physics*, 65(8):3187–3195, 10 1976. ISSN 0021-9606. doi: 10.1063/1.433490. URL https://doi.org/10.1063/1.433490.

[135] D. T. Matselyukh, V. Despré, N. V. Golubev, A. I. Kuleff, and H. J. Wörner. Decoherence and revival in attosecond charge migration driven by non-adiabatic dynamics. *Nature Physics*, 18:1206–1213, 2022.

[136] J. Vester, V. Despré, and A. I. Kuleff. The role of symmetric vibrational modes in the decoherence of correlation-driven charge migration. *The Journal of Chemical Physics*, 158:104305, 2023.

[137] Diptesh Dey, Alexander I. Kuleff, and Graham A. Worth. Quantum Interference Paves the Way for Long-Lived Electronic Coherences. *Physical Review Letters*, 129:173203, Oct 2022. doi: 10.1103/PhysRevLett.129.173203. URL https://link.aps.org/doi/10.1103/PhysRevLett.129.173203.

[138] Morgane Vacher, Fabio E. A. Albertani, Andrew J. Jenkins, Iakov Polyak, Michael J. Bearpark, and Michael A. Robb. Electron and nuclear dynamics following ionisation of modified bismethylene-adamantane. *Faraday Discussions*, 194:95–115, 2016. doi: 10.1039/C6FD00067C. URL http://dx.doi.org/10.1039/C6FD00067C.

[139] András Csehi, Péter Badankó, Gabor J Halasz, Ágnes Vibók, and Benjamin Lasorne. On the preservation of coherence in the electronic

wavepacket of a neutral and rigid polyatomic molecule. *Journal of Physics B*, 53(18):184005, 2020.

[140] James R. Durig and Jeffrey S. Church. Vibrational spectra and the assignment of the normal modes of 1,1,1-trifluoro-2-propanone. *Spectrochimica Acta Part A*, 36:957–964, 1980. URL https://doi.org/10.1016/0584-8539(80)80174-7.

[141] Časlav Brukner. On the quantum measurement problem. *Quantum [un]speakables II: half a century of Bell's theorem*, pages 95–117, 2017.

[142] Maximilian Schlosshauer. Quantum decoherence. *Physics Reports*, 831:1–57, 2019. ISSN 0370-1573. doi: 10.1016/j.physrep.2019.10.001. URL https://www.sciencedirect.com/science/article/pii/S0370157319303084.

[143] Jeffrey Bub and Itamar Pitowsky. Two dogmas about quantum mechanics. *Many worlds*, pages 433–459, 2010.

[144] Tim Maudlin. Three measurement problems. *Topoi*, 14(1):7–15, 1995.

[145] Itamar Pitowsky. Quantum mechanics as a theory of probability. In *Physical theory and its interpretation: Essays in honor of Jeffrey Bub*, pages 213–240. Springer, 2006.

[146] David M. Cardoza. *Understanding learning control of molecular fragmentation.* PhD thesis, Stony Brook University, 2006. Copyright - Database copyright ProQuest LLC; ProQuest does not claim copyright in the individual underlying works; Last updated - 2023-03-22.

[147] David Cardoza, Mark Baertschy, and Thomas Weinacht. Understanding learning control of molecular fragmentation. *Chemical physics letters*, 411(4-6):311–315, 2005.

[148] Benjamin Nachman. Opinion: The Rise of the Data Physicist. *APS News*, 32, 2023. URL https://www.aps.org/publications/apsnews/202311/backpage.cfm.

[149] Constantin Brif, Raj Chakrabarti, and Herschel Rabitz. Control of quantum phenomena: past, present and future. *New Journal of Physics*, 12 (7):075008, 2010.

[150] Baiqing Li, Gabriel Turinici, Viswanath Ramakrishna, and Herschel Rabitz. Optimal dynamic discrimination of similar molecules through quantum learning control. *The Journal of Physical Chemistry B*, 106(33): 8125–8131, 2002.

[151] Baiqing Li, Herschel Rabitz, and Jean-Pierre Wolf. Optimal dynamic discrimination of similar quantum systems with time series data. *The Journal of chemical physics*, 122(15), 2005.

[152] Denis Aglagul, Brian Kaufman, Chuan Cheng, Thomas Weinacht, Tobias Saule, Carlos A. Trallero-Herrero, and Andrei Nomerotski. A simple approach for characterizing the spatially varying sensitivity of microchannel plate detectors. *Review of Scientific Instruments*, 93(7): 075108, 07 2022. ISSN 0034-6748. doi: 10.1063/5.0092346. URL `https://doi.org/10.1063/5.0092346`.

[153] Private Communication with John Hackwelder, the Manufacturer of Extorr Residual Gas Analyzers.

[154] *Translation of the Turkish Text in Acknowledgments.* I am always grateful to my mom who has supported me and put me on this career path. It is because of the courage that she gave me that I dared to go to a boarding school in Istanbul, then to Germany and finally to America. Ever since my childhood my mom has taught me to stand on my own two feet, to defend my rights and to fulfill my responsibilities. Consequently, she has an influence in every success I have ever had. Similarly, my dad has supported me throughout my life. I could always reach out to him whenever I felt lost or need his help and advice. During my PhD I have lost my grandmother, my grandfather and my aunt Fatma. May their souls rest in peace. I am so eternally grateful for my grandparents part in raising me. Finally, I want to thank my aunt Şükran my cousins Sümer, Esra, Petek, Ayşegül, Nisan and all my family members for their love and support.